Spatial Considerations in Membrane Electrode Assembly CO2 Electrolyzers

Subramanian, S.S.

DOI
10.4233/uuid:33ff19c7-313e-4342-8833-bcddae8e7116

Publication date
2024

Document Version
Final published version

Citation (APA)
Subramanian, S. S. (2024). *Spatial Considerations in Membrane Electrode Assembly CO2 Electrolyzers*. [Dissertation (TU Delft), Delft University of Technology]. https://doi.org/10.4233/uuid:33ff19c7-313e-4342-8833-bcddae8e7116

SPATIAL CONSIDERATIONS IN MEMBRANE ELECTRODE ASSEMBLY CO_2 ELECTROLYZERS

SPATIAL CONSIDERATIONS IN MEMBRANE ELECTRODE ASSEMBLY CO_2 ELECTROLYZERS

Dissertation

for the purpose of obtaining the degree of doctor
at Delft University of Technology
by the authority of the Rector Magnificus, prof. dr. ir. T.H.J.J. van der Hagen,
chair of the Board for Doctorates
to be defended publicly on
Thursday 23 May 2024 at 10:00 o' clock

by

Siddhartha SUBRAMANIAN

Master of Science in Chemical Engineering,
Loughborough University, United Kingdom,
born in Tarapur, India

This dissertation has been approved by the promotors.

Composition of the doctoral committee:

Rector Magnificus,	chairperson
Dr. T.E. Burdyny,	Delft University of Technology, *promotor*
Em. Prof. dr. B. Dam,	Delft University of Technology, *promotor*
Independent members:	
Prof. dr. A. Urakawa	Delft University of Technology
Prof. dr. B. Seger	Technical University of Denmark, Denmark
Dr. A.F. Cuenca	Eindhoven University of Technology
Dr. M.C. Figueiredo	Eindhoven University of Technology
Prof. dr. F. Mulder,	Delft University of Technology, reserve member

The work described in this thesis has been carried out in the Materials for Energy Conversion and Storage (MECS) group, Department of Chemical Engineering, Faculty of Applied Sciences, Delft University of Technology. It was supported by co-financing from Shell and a PPP-allowance from Top Consortia for Knowledge and Innovation (TKI's) of the Ministry of Economic Affairs and Climate in the context of the TU Delft e-Refinery Institute and Netherlands Organisation for Scientific Research (NWO) through the Veni grant (Dr. T.E. Burdyny).

Printed by: Proefschriftspecialist

Cover by: Katrina Goretskaya

ISBN 000-00-0000-000-0

An electronic copy of this dissertation is available at
https://repository.tudelft.nl/.

To my

Mom and Dad

CONTENTS

PREFACE

In presenting this doctoral thesis, I am grateful for the journey that has led me to this point. Undertaking this research has been a profound endeavor, marked by dedication, intellectual exploration, and collaborative learning.

I wish to express my sincere appreciation to my supervisors, committee members, colleagues, friends and family whose unwavering support, guidance, and encouragement have been instrumental throughout this journey. Their collective influence has enhanced the depth and breadth of this work, and it is my hope that this thesis makes a meaningful contribution to the CO_2 electrolysis community.

Siddhartha Subramanian
Delft, January 2024

1

GENERAL INTRODUCTION

1.1. GETTING TO NET ZERO

52 billion tonnes per year. That's the average amount of greenhouse gases the world typically adds to the atmosphere. Net Zero by 2050. This is the target we should strive for to stop the earth from warming and avoid worst effects of climate change. Achieving this is truly one of the most ambitious goals of this century with a huge impact on our lives and organizations [1–3].

Out of the 52 billion tonnes, carbon dioxide emissions (CO_2) account for the greatest portion of warming associated with human activities (37 billion tonnes). Global temperatures since pre-industrial times, have increased by 1 degree Celsius (^oC) and without getting to net zero CO_2 emissions by 2050, the world is projected to have between 1.5 and 3^oC of warming by mid-century and it is important to remember here that a 'little' is a lot. A small increase in global temperatures - just 1 or 2^oC could actually cause a lot of trouble. For example, the average temperature of the earth during the ice age was just 6 degrees lower than its today [4–6]. This implies that the projected increases in global temperatures could have disastrous consequences such as storms getting worse in some places and more severe droughts in other places, leading to a strange feast-or-famine situations in various parts of the world.

Another noticeable effect of climate change is the consistent retreat of the global surface ice coverage since 1950, something scientists do not believe to have happened during the last 2000 years [7, 8]. And a planet with less surface ice does not reflect as much heat from the sun, further accelerating global warming. The worrying part is then not the change in temperature itself, but the pace at which it's happening, which makes it challenging for civilizations and surrounding ecosystem to rapidly adapt to the changing weather, rising sea levels and seasonal changes.

Getting to net zero will however be quite challenging. The major reason for this is the fact that fossil fuels are so pervasive in our day to day lives, right from the materials we use to the buildings we live in. A honest accounting of greenhouse gas emissions is then essential to understand the obstacles and design new infrastructure for the much-required energy transition. A breakdown of the greenhouse gases emitted by human activities is shown in Table 1.1. Getting to zero means zeroing out every one of these categories:

Table 1.1: A breakdown of greenhouse gas emissions from human activities (Source: [9]).

Source	**Contribution**
Making things (cement, steel and plastic)	29 %
Plugging in (electricity)	26 %
Growing things (plants, animals)	22 %
Getting around (planes, trucks, cargo ships)	16 %
Keeping warm and cool (heating, cooling, refrigeration)	7 %

As shown in Table 1.1, it might be surprising to see that electricity accounts for just over a quarter of all emissions. The good news is that although electricity generation accounts for only 26% of the problem, it could represent much more than 26% of the solution such as in electrifying heating and cooling systems instead of burning hydrocarbons. Electrification then plays a key role but is not solely sufficient to reach net zero.

Importantly, renewable energy sources like solar and wind have become cheaper over the years [10, 11] and challenges associated with intermittency and transmission capacity currently limit its wide scale adoption and replacement over fossil fuels. Before understanding these challenges, it is first important to understand how current energy services operate and the flow of energy from source to sink.

Energy flow Sankey diagrams are great for understanding this flow of energy from various sources. Figure 1.1 shows the Sankey diagram in the United States (US) for the year 2022. The US is taken as an example here as it is one of world's largest emitters of greenhouse gases (per capita) and the main idea behind sankey flow diagrams can be translated to other countries as well. Here, the primary energy sources come on the left side. The amount of electricity generated from these primary sources is shown in the middle, which is further split into various areas of use such as transportation, industrial and electricity generation. The different sectors where electricity is being used provides a quantification of energy consumption from all sources. Notably, we see that for the year 2022, electricity generation still heavily relied on fossil fuels such as coal and natural gas in the United States. We also see that about two-thirds of energy generated from these fossil fuels gets thrown out as ‘Rejected energy’ (red box on the right) in the form of waste heat energy generated from the burning of oil, natural gas and coal. Importantly, this shows that we *do not have to replace all the energy produced from current fossil fuel route*, but only replace the unwasted energy services, that accounts for one-third of the current fossil fuel route. The usage of electricity from renewable or low carbon energy sources will generate substantially less waste heat than these fossil fuel route, which means that these alternate energy sources can compete with fossil fuel based power plants. We must therefore focus on building the right infrastructure to get to net zero.

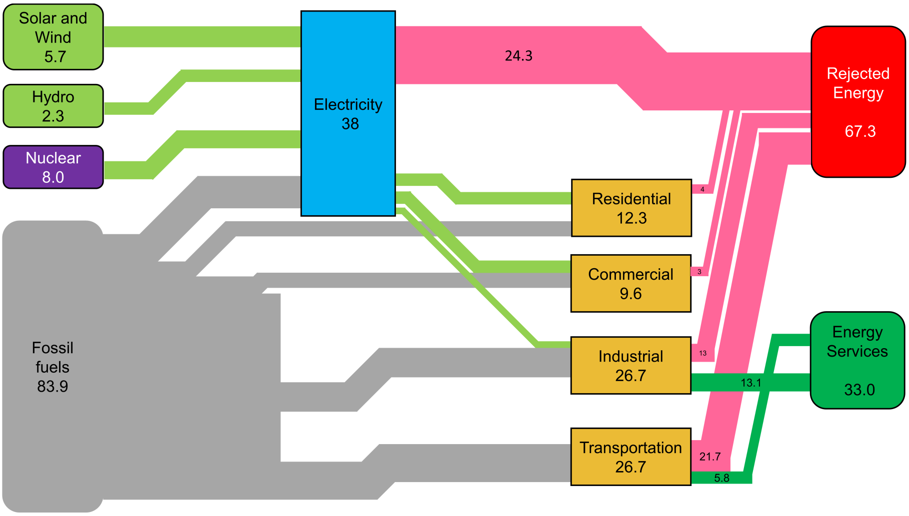

Figure 1.1: Sankey diagram showing the estimated energy consumption in the United States for the year 2022 (101 quads) released by the Lawrence Livermore National Laboratory. 1 quad corresponds to 1015 British thermal units (BTU) or 1 x 108 J.

1.2. Renewably Powered CO_2 Electrolysis

If done properly, most of the sectors emitting greenhouse gas emissions can be de-carbonized. Importantly, these everyday items which are essential for our society, themselves contain carbon. However, going back to Table 1.1, a few sectors where decarbonization might be challenging are the manufacturing of plastics, cement and steel which accounts for a combined 29% of carbon dioxide emissions. While, electrification of the manufacturing steps in these processes might reduce carbon emissions, a by-product of processes such as cement still emits CO_2 and has to be either captured or converted to a commodity chemical. It is then essential to establish an industrial carbon cycle where captured CO_2 from point sources or directly from air[12–14] or oceans [15–17] is coupled to renewably powered electricity for sustainable hydrocarbon production. CO_2 electrolysis becomes an attractive technology for sustainbly producing these carbon based chemicals. This technology involves electrochemical CO_2 reduction reaction (CO_2RR), most commonly performed in aqueous electrolytes. A reactor having a constant CO_2 source, aqueous electrolyte, and electrons from renewable source are then required to produce value added chemicals and close the carbon cycle as shown in Figure 1.2.

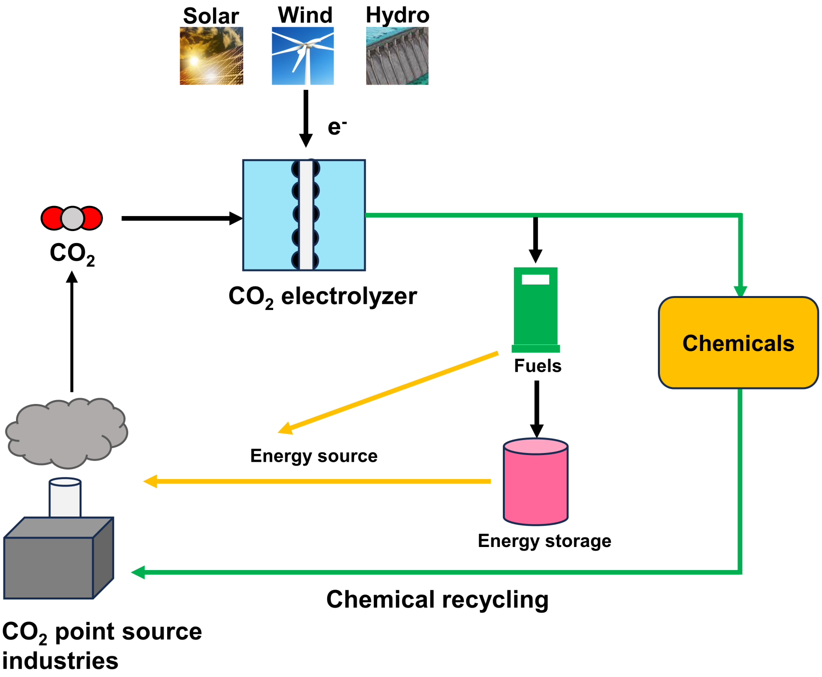

Figure 1.2: Simplified view of how utilizing renewable energy for CO_2 electrolysis to make base chemicals or fuels can close the carbon cycle.

Additionally, an important commodity chemical that is consumed the most and widely used in the production of textile fibres, plastics and furniture is ethylene, which has a 200 billion USD (US dollars) market [18–20]. Currently, ethylene is primarily produced by steam cracking process which involves the breakdown of hydrocarbons through natural gas or petroleum refining. Substantial amount of carbon dioxide are emitted in this process and it is also energy intensive due to the high temperatures (800-900 deg C) that are required. Electrochemical CO_2RR might play a critical role here for replacing the current fossil fuel based route to synthesize ethylene. A few startups like Dioxycle (Paris) and Twelve (US) are already building these CO_2 electrolyzers to manufacture various commodity chemicals. Formic acid (0.5 billion USD) and CO (5 billion USD) are other products where CO_2 electrolysis could be attractive, however these products have a much lower market value. This thesis explores the challenges of scaling up electrochemical CO_2 conversion to CO and ethylene, which are the two major products where the technology could become attractive.

1.2.1. ELECTROCHEMICAL CO_2 REDUCTION (CO_2RR) - A BRIEF OVERVIEW

CO_2 is a thermodynamically stable molecule with a standard heat of formation of -393.4 KJ/mol [21]. Due to its high stability, a significant amount of energy is required to convert CO_2 into various chemicals such as CO or hydrocarbons. With decreasing electricity prices from renewable sources, the use of electrons to convert CO_2 into base chemicals such as CO and ethylene has seen significant progress in the past decade with the field moving from numerous physical scales (nm to m) for commercialization of this technology [22–24].

Fundamentally, CO_2RR is performed in an electrolytic cell comprising of two half reactions at the positively charged (anode) and negatively charged (cathode) electrodes. The electrocatalyst is then a material used at the two electrodes (anode and cathode) and CO_2 is converted to a specific product at the surface of this electrocatalyst. The reaction kinetics and rates are affected by the choice of the material, the electrolyte solution and the applied potential at the electrodes. In aqueous solutions, CO_2RR has been found to occur either through a concerted proton coupled or proton decoupled (cation coupled) electron transfer mechanisms [25–29].

In short, CO_2RR in aqueous media requires an appropriate catalyst, a proton source and an ion exchange membrane to separate the two compartments with respective half-cell reactions. The half-cell reaction at the anode side provides electrons to the cathode and one of the commonly used reaction at the anode is the oxygen evolution reaction. Depending on the local reaction environment around the catalyst, various products can be obtained from CO_2RR. Two of those commonly investigated products are CO (2 e^-) and ethylene (12 e^-) and the thermodynamic potentials required for each of these products are shown in equations 1.1 and 1.2.

$$CO_2 + H_2O + 2e^- \rightarrow CO + 2OH^- \quad (-0.11V\ vs. RHE) \tag{1.1}$$

$$2CO_2 + 8H_2O + 12e^- \rightarrow C_2H_4 + 12OH^- \quad (-0.08V\ vs. RHE) \tag{1.2}$$

$$2H_2O + 2e^- \rightarrow H_2 + 2OH^- \quad (0V\ vs. RHE) \tag{1.3}$$

1.2.2. REACTION RATE IS PRIMARILY INFLUENCED BY THE DIFFUSION LENGTH OF CO_2 REACHING THE CATALYST

As industrial operation requires higher reaction rates (>100 mA/cm^2), mass transport of reactants reaching the catalyst surface affects the maximum attainable reaction rate (limiting current density) [30]. This is because CO_2 that is fed into the reactor reaches the catalyst primarily by diffusion and the thermodynamically favourable hydrogen evolution reaction (Equation 1.3) competes with CO_2RR, from the ample water present in the aqueous electrolyte. The limiting current density is then primarily influenced by the Nernstian diffusion layer (From Fick's first law) with an inverse relationship as shown in the following equation:

$$j_{lim,CO_2RR} = \frac{n^e\, F\, D_{CO_2}\, C_0}{\delta} \tag{1.4}$$

Here j is the limiting current density for CO_2RR, n^e is the number of electrons involved in the reaction, F is Faraday's constant, D_{CO_2} is Diffusivity of CO_2 in liquid phase and C_0 is concentration of CO_2 in the electrolyte solution and δ is the Nernstian diffusion length.

All these parameters defining the limiting current density are affected by the reactor configuration employed and the operating conditions. In a typical H-cell used in laboratories, CO_2 is bubbled into the liquid electrolyte and the limiting current density is limited to 20-30 mA/cm^2 due to the lower CO_2 solubility (30 mM) in water [31] and the longer diffusion length for CO_2 to travel from the bulk electrolyte to the catalyst surface (50 μm). The use of gas diffusion electrodes (GDE) as porous transport layers helps overcome this mass transport limitation by decreasing the diffusion length of CO_2 by three orders of magnitude (50-100 nm), resulting in higher limiting current densities (100-1000 mA/cm^2).

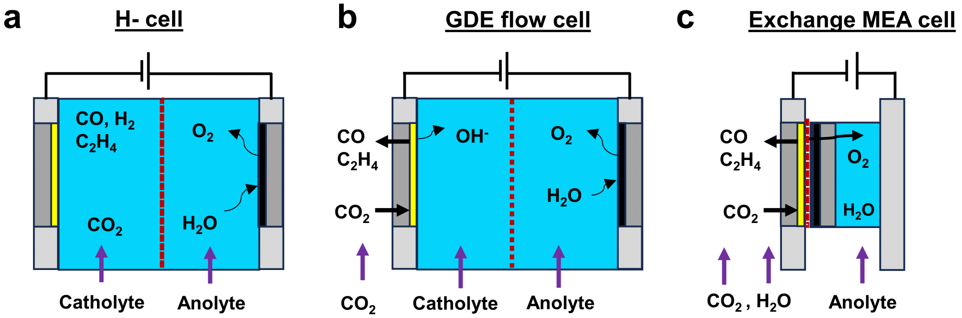

Figure 1.3: The most commonly used lab scale CO_2 electrolyzers. (a) H-cell, (b) Gas diffusion electrode cell with a flowing anolyte and catholyte, (c) A zero gap membrane electrode assembly with humidified CO_2 at the cathode and an exchange solution at the anode side.

Among electrochemical reactors employing GDE, two widely adopted designs are the GDE flow cells (Figure 1.3b), where a flowing catholyte separates the catalyst from the ion exchange membrane [32–34] and a membrane electrode assembly [35], where the catalyst is directly pressed against the membrane either as CCS (catalyst coated substrate) or CCM (catalyst coated membrane), resulting in a zero gap configuration at the cathode. The zero gap membrane electrode assembly is then promising for scale up due to the lower ohmic losses encountered in the reactor. As the total cell voltage for an electrolyzer becomes one of the important metrics for scale up, a zero gap design often becomes more attractive for commercialization although, challenges related to operational stability exists. The three commonly adopted reactor configurations are shown in Figure 1.3.

Going to back to equation 1.4, we see that there a few parameters that are constant and are unaltered by the reactor used. The number of electrons for the given electrochemical reaction (n^e), the Faraday's constant (F) and the diffusivity of CO_2 in the liquid phase (D_{CO_2}) remain constant at a given temperature and pressure. However, the terms C_0, which corresponds to the local CO_2 concentration at the catalyst surface can vary depending on the operating conditions. Since water reduction becomes the primary proton source for CO_2, there is a significant amount of hydroxide (OH^-) ions generated at the catalyst surface. These (OH^-) ions can react with CO_2 fed into the reactor forming bicarbonates (HCO_3^-) and carbonates (CO_3^{2-}). This not only creates CO_2 concentration gradients from the bulk of the electrolyte to the interface of the catalyst surface, but also generates pH gradients due to differences in concentrations of (OH^-), (CO_3^{2-} and (HCO_3^-) ions. Overall, this means that the local CO_2 concentration at the catalyst will always be less than its solubility limit in water ($\approx$ 34 mM) due to its reaction with hydroxide ions.

Further, the Nernstian diffusion length can also change based on the design of the electrolyzer. Using catalyst coated GDE, diffusion lengths of 10-20 microns have been reported which has enabled these electrolyzers reach an order of magnitude higher current densities than H-cells. A recent study by Wen et.al [36] used forced convection of saturated CO_2 solution in electrolyte through a porous transport layer and achieved a current density of 3A/cm^2, significantly higher than works reported in commonly used GDE flow cells. The authors attributed this massive increase in current density to the lower diffusion layer thickness of about 1 micron, 20 times lower than in commonly used GDE flow cells. This work clearly shows that CO_2 electrolysis reaching higher reaction rates is primarily affected by the diffusion layer thickness and decreasing the diffusion lengths by efficient design of porous transport layers can enable reach current densities on the order of A/cm^2.

1.2.3. (BI)CARBONATE FORMATION DURING CO_2RR

The use of alkaline media for CO_2RR is primarily due the favourable kinetics of CO_2RR over competing HER, which has sluggish kinetics [37–39]. In membrane electrode assembly reactors, the use of anion exchange membranes are then preferable since it conducts only anions such as hydroxide (OH^-) ions, thus maintaining a favourable alkaline environment at the cathode. However, this leads to the unwanted consumption of CO_2 to OH^- ions producing carbonate and bicarbonate ions near the electrode surface (See Equations 1.5 and 1.6).

Due to the five order of magnitude higher reaction rate of carbonate formation (Equation 1.6) than bicarbonate formation reaction (Equation 1.5), carbonate concentration becomes dominant at higher local alkaline (pH >12) conditions[40]. In anion exchange membrane electrode assembly reactors (AEMEA), this leads to the primary anion charge carrier to become CO_3^{2-} instead of OH^- leading to significant CO_2 losses. A consequence of this is the maximum single pass CO_2 utilization of 50% for 2e$^-$ products like CO and 25% for 12e$^-$ products like ethylene. To alleviate this issue, cation exchange or bipolar membranes can be used to create acidic/near neutral pH around the cathode, however this leads to other challenges such as faster carbonate precipitation blocking active sites and competing HER taking over thus, limiting the performance of CO_2RR.

$$CO_2 + OH^- \leftrightarrow HCO_3^- \quad (pK_a = 7.8) \tag{1.5}$$

$$HCO_3^- + OH^- \leftrightarrow CO_3^{2-} \quad (pK_a = 10.3) \tag{1.6}$$

It is important to understand that these trade-offs in performance and energy efficiencies of AEMEA reactors for designing industrially relevant CO_2 electrolyzers. In addition, insights into the variations in reactant and product concentrations, pressure drop and optimal operating conditions deserves scrutiny. This PhD work aims to answer a few of these questions and are divided into different chapters as shown below.

1.3. CHAPTER OUTLINE

The chapter-wise outline of the dissertation is given below:

- Chapter 2 provides the context for spatial considerations in CO_2 electrolyzers and how such strategies help formulate design rules for maximizing performance. This chapter discusses briefly, the recent works where spatial effects have been studied and some future directions for this line of research.

- Chapter 3 provides detailed insights into the trade-offs associated with product selectivity and single pass CO_2 utilization in a silver (Ag) based zero gap CO_2 electrolyzers and how variations in reactant concentrations leads to a spatial faradaic efficiency inside a reactor at higher current densities. Here, an introduction to the mass transport and fluid model for predicting local CO_2 concentrations is provided which then serves as tools for chapters 4 and 5.

- Chapter 4 discusses the influence of gas flow field pattern on the performance of a Ag based zero gap CO_2 electrolyzer. Varying the gas flow pattern not only alters reactant distribution but also alters the pressure drop, electrolyte flooding the gas diffusion layers and stability of operation. We use serpentine, parallel and interdigitated flow fields to understand these effects.

- Chapter 5 delves into the influence of CO residence on multi-carbon product formation rates in a Cu based zero gap CO_2 electrolyzer. Using a combination of residence time distribution curves, operating flow rates, flow fields and CO electrolysis we show insights into the strategies for maximizing residence time of CO to maximize multi-carbon product formation in a zero gap CO_2 electrolyzer.

- Chapter 6 briefly talks about the role of cation crossover in AEM based CO_2 electrolyzer and trade-offs associated with cell voltage, salt precipitation and operating conditions in a membrane electrode assembly configuration.

- In Chapter 7, I discuss future perspectives on scaling up CO_2 electrolyzers based on the chapters presented in this dissertation.

REFERENCES

[1] R. S. Dimitrov. “The Paris agreement on climate change: Behind closed doors”. In: *Global environmental politics* 16.3 (2016), pp. 1–11.

[2] J. Rogelj, M. Den Elzen, N. Höhne, T. Fransen, H. Fekete, H. Winkler, R. Schaeffer, F. Sha, K. Riahi, and M. Meinshausen. “Paris Agreement climate proposals need a boost to keep warming well below 2 C”. In: *Nature* 534.7609 (2016), pp. 631–639.

[3] S. Bouckaert, A. F. Pales, C. McGlade, U. Remme, B. Wanner, L. Varro, D. D’Ambrosio, and T. Spencer. “Net zero by 2050: A roadmap for the global energy sector”. In: (2021).

[4] S. Dobricic, E. Vignati, and S. Russo. “Large-scale atmospheric warming in winter and the Arctic sea ice retreat”. In: *Journal of Climate* 29.8 (2016), pp. 2869–2888.

[5] Z. Jinping, S. Jiuxin, W. Zhaomin, L. Zhijun, and H. Fei. “Arctic amplification produced by sea ice retreat and its global climate effects”. In: *Advances in Earth Science* 30.9 (2015), p. 985.

[6] A. Kumar, J. Yadav, and R. Mohan. “Global warming leading to alarming recession of the Arctic sea-ice cover: Insights from remote sensing observations and model reanalysis”. In: *Heliyon* 6.7 (2020).

[7] J. Yadav, A. Kumar, and R. Mohan. “Dramatic decline of Arctic sea ice linked to global warming”. In: *Natural Hazards* 103 (2020), pp. 2617–2621.

[8] D. G. Vaughan and C. S. Doake. “Recent atmospheric warming and retreat of ice shelves on the Antarctic Peninsula”. In: *Nature* 379.6563 (1996), pp. 328–331.

[9] B. Gates. *How to avoid a climate disaster: the solutions we have and the breakthroughs we need*. Vintage, 2021.

[10] V. Sivaram, J. O. Dabiri, and D. M. Hart. “The need for continued innovation in solar, wind, and energy storage”. In: *Joule* 2.9 (2018), pp. 1639–1642.

[11] L. R. Brown. *The great transition: Shifting from fossil fuels to solar and wind energy*. WW Norton & Company, 2015.

[12] C. Breyer, M. Fasihi, C. Bajamundi, and F. Creutzig. “Direct air capture of CO2: a key technology for ambitious climate change mitigation”. In: *Joule* 3.9 (2019), pp. 2053–2057.

[13] A. Kumar, D. G. Madden, M. Lusi, K.-J. Chen, E. A. Daniels, T. Curtin, J. J. Perry IV, and M. J. Zaworotko. “Direct air capture of CO2 by physisorbent materials”. In: *Angewandte Chemie International Edition* 54.48 (2015), pp. 14372–14377.

[14] N. McQueen, K. V. Gomes, C. McCormick, K. Blumanthal, M. Pisciotta, and J. Wilcox. “A review of direct air capture (DAC): scaling up commercial technologies and innovating for the future”. In: *Progress in Energy* 3.3 (2021), p. 032001.

[15] C.-F. de Lannoy, M. D. Eisaman, A. Jose, S. D. Karnitz, R. W. DeVaul, K. Hannun, and J. L. Rivest. “Indirect ocean capture of atmospheric CO2: Part I. Prototype of a negative emissions technology”. In: *International journal of greenhouse gas control* 70 (2018), pp. 243–253.

[16] R. Sharifian, R. Wagterveld, I. Digdaya, C. Xiang, and D. Vermaas. “Electrochemical carbon dioxide capture to close the carbon cycle”. In: *Energy & Environmental Science* 14.2 (2021), pp. 781–814.

[17] I. A. Digdaya, I. Sullivan, M. Lin, L. Han, W.-H. Cheng, H. A. Atwater, and C. Xiang. “A direct coupled electrochemical system for capture and conversion of CO2 from oceanwater”. In: *Nature communications* 11.1 (2020), p. 4412.

[18] R. Chauhan, R. Sartape, N. Minocha, I. Goyal, and M. R. Singh. “Advancements in Environmentally Sustainable Technologies for Ethylene Production”. In: *Energy & Fuels* 37.17 (2023), pp. 12589–12622.

[19] Y. Gao, L. Neal, D. Ding, W. Wu, C. Baroi, A. M. Gaffney, and F. Li. “Recent advances in intensified ethylene production—a review”. In: *ACS Catalysis* 9.9 (2019), pp. 8592–8621.

[20] L. Berkelaar, J. van der Linde, J. Peper, A. Rajhans, D. Tiemessen, L. van der Ham, and H. van den Berg. “Electrochemical conversion of carbon dioxide to ethylene: plant design, evaluation and prospects for the future”. In: *Chemical Engineering Research and Design* 182 (2022), pp. 194–206.

[21] R. L. Berg and C. E. Vanderzee. “Thermodynamics of carbon dioxide and carbonic acid:(a) the standard enthalpies of solution of Na2CO3 (s), NaHCO3 (s), and CO2 (g) in water at 298.15 K;(b) the standard enthalpies of formation, standard Gibbs energies of formation, and standard entropies of CO2 (aq), HCO3-(aq), CO32-(aq), NaHCO3 (s), Na2CO3 (s), Na2CO3· H2O (s), and Na2CO3· 10H2O (s)”. In: *The Journal of Chemical Thermodynamics* 10.12 (1978), pp. 1113–1136.

[22] Z. Li, H. Zhang, H. Xu, and J. Xuan. “Advancing the multiscale understanding on solid oxide electrolysis cells via modelling approaches: A review”. In: *Renewable and Sustainable Energy Reviews* 141 (2021), p. 110863.

[23] D. Wakerley, S. Lamaison, J. Wicks, A. Clemens, J. Feaster, D. Corral, S. A. Jaffer, A. Sarkar, M. Fontecave, E. B. Duoss, *et al.* “Gas diffusion electrodes, reactor designs and key metrics of low-temperature CO2 electrolysers”. In: *Nature Energy* 7.2 (2022), pp. 130–143.

[24] T. Burdyny and W. A. Smith. “CO 2 reduction on gas-diffusion electrodes and why catalytic performance must be assessed at commercially-relevant conditions”. In: *Energy & Environmental Science* 12.5 (2019), pp. 1442–1453.

[25] M. R. Singh, Y. Kwon, Y. Lum, J. W. Ager III, and A. T. Bell. “Hydrolysis of electrolyte cations enhances the electrochemical reduction of CO2 over Ag and Cu”. In: *Journal of the American chemical society* 138.39 (2016), pp. 13006–13012.

[26] M. C. Monteiro, F. Dattila, N. López, and M. T. Koper. “The role of cation acidity on the competition between hydrogen evolution and CO2 reduction on gold electrodes”. In: *Journal of the American Chemical Society* 144.4 (2021), pp. 1589–1602.

[27] J. Gu, S. Liu, W. Ni, W. Ren, S. Haussener, and X. Hu. “Modulating electric field distribution by alkali cations for CO2 electroreduction in strongly acidic medium”. In: *Nature Catalysis* 5.4 (2022), pp. 268–276.

[28] S. Ringe, E. L. Clark, J. Resasco, A. Walton, B. Seger, A. T. Bell, and K. Chan. “Understanding cation effects in electrochemical CO 2 reduction”. In: *Energy & Environmental Science* 12.10 (2019), pp. 3001–3014.

[29] J. Resasco, L. D. Chen, E. Clark, C. Tsai, C. Hahn, T. F. Jaramillo, K. Chan, and A. T. Bell. “Promoter effects of alkali metal cations on the electrochemical reduction of carbon dioxide”. In: *Journal of the American Chemical Society* 139.32 (2017), pp. 11277–11287.

[30] L.-C. Weng, A. T. Bell, and A. Z. Weber. “Modeling gas-diffusion electrodes for CO 2 reduction”. In: *Physical Chemistry Chemical Physics* 20.25 (2018), pp. 16973–16984.

[31] L. W. Diamond and N. N. Akinfiev. “Solubility of CO2 in water from- 1.5 to 100 C and from 0.1 to 100 MPa: evaluation of literature data and thermodynamic modelling”. In: *Fluid phase equilibria* 208.1-2 (2003), pp. 265–290.

[32] D. M. Weekes, D. A. Salvatore, A. Reyes, A. Huang, and C. P. Berlinguette. “Electrolytic CO2 reduction in a flow cell”. In: *Accounts of chemical research* 51.4 (2018), pp. 910–918.

[33] J.-B. Vennekoetter, R. Sengpiel, and M. Wessling. “Beyond the catalyst: How electrode and reactor design determine the product spectrum during electrochemical CO2 reduction”. In: *Chemical Engineering Journal* 364 (2019), pp. 89–101.

[34] T. N. Nguyen and C.-T. Dinh. “Gas diffusion electrode design for electrochemical carbon dioxide reduction”. In: *Chemical Society Reviews* 49.21 (2020), pp. 7488–7504.

[35] L. Ge, H. Rabiee, M. Li, S. **Subramanian**, Y. Zheng, J. H. Lee, T. Burdyny, and H. Wang. “Electrochemical CO_2 reduction in membrane-electrode assemblies”. In: *Chem* 8.3 (2022), pp. 663–692.

[36] G. Wen, B. Ren, X. Wang, D. Luo, H. Dou, Y. Zheng, R. Gao, J. Gostick, A. Yu, and Z. Chen. “Continuous CO2 electrolysis using a CO2 exsolution-induced flow cell”. In: *Nature Energy* 7.10 (2022), pp. 978–988.

[37] W. Sheng, M. Myint, J. G. Chen, and Y. Yan. “Correlating the hydrogen evolution reaction activity in alkaline electrolytes with the hydrogen binding energy on monometallic surfaces”. In: *Energy & Environmental Science* 6.5 (2013), pp. 1509–1512.

[38] N. Mahmood, Y. Yao, J.-W. Zhang, L. Pan, X. Zhang, and J.-J. Zou. “Electrocatalysts for hydrogen evolution in alkaline electrolytes: mechanisms, challenges, and prospective solutions”. In: *Advanced science* 5.2 (2018), p. 1700464.

[39] Y. Zheng, Y. Jiao, A. Vasileff, and S.-Z. Qiao. “The hydrogen evolution reaction in alkaline solution: from theory, single crystal models, to practical electrocatalysts”. In: *Angewandte Chemie International Edition* 57.26 (2018), pp. 7568–7579.

[40] T. Moore, X. Xia, S. E. Baker, E. B. Duoss, and V. A. Beck. “Elucidating mass transport regimes in gas diffusion electrodes for CO2 electroreduction”. In: *ACS Energy Letters* 6.10 (2021), pp. 3600–3606.

2

INTRODUCTION TO SPATIAL EFFECTS IN CO_2 ELECTROLYZERS

Logic will you get you from A to Z. Imagination will get you everywhere.

- Albert Einstein

CO_2 electrolyzers show great promise as clean energy conversion technology for the production of value-added chemicals. In recent years, research has moved from understanding the activity and selectivity of products from CO_2 electroreduction on a single catalyst site (OD) to interactions with gas, liquid and electrolyte (1D). For scaling up these electrolyzers however, 2D and 3D spatial variations in product selectivity and activity arise due to the design of reactor components, as well as spatial variations in concentration of reactants, intermediates, and products. This means that conventional 'black box' measurement protocols are insufficient to describe a complete picture of the catalyst microenvironment inside an electrolyzer. In this perspective, we provide an argument for why CO_2 electrolysis cannot be approximated through a 1D analysis. We use recent works on spatial effects to support this claim and show how a spatial perspective is essential for proper data interpretation, design of effective catalysts and prolonging the lifetime of CO_2 electrolyzers. Researchers should then view the electrochemical reaction in multi-dimensions (2D and 3D) for accelerating scale up efforts.

This chapter is part of a manuscript under preparation, titled "Going beyond one dimension: how spatial effects define CO_2 electrolysis systems" by S.Subramanian, H.P.I. Van Montfort and Thomas Burdyny. Both SS and HPIVM contributed equally to the writing and editing of this MS.

2.1. INTRODUCTION

Low temperature CO_2 electrolysis using renewable energy sources is an attractive route to generate fossil-free fuels and base chemicals [1–3]. Advancements in developing new catalysts and reactor designs have enabled the scale up of electrochemical CO_2 reduction reaction (CO_2RR) to a diverse range of products. With the adoption of gas diffusion electrodes (GDE) in membrane electrode assembly configuration, CO_2RR has achieved industrially relevant reaction rates (>200 mA/cm^2), posing itself as strong candidate for replacing solid oxide electrolyzers that require extremely high temperatures (>600^{o}C) [4].

While significant advancements in CO_2RR have taken place in the past decade, the performance metrics of these systems are still widely studied using conventional 'black box' measurement protocols [5], which involve characterization using electrochemical techniques and gas/liquid product quantification at the inlet and exit of the reactor. These 'device averaged' metrics are valuable and currently accepted in the field. However, the 'black box' approach leads to an incomplete understanding of CO_2 electrolyzers and will lead to data misinterpretation in cases of high CO_2 conversions, reactive products, larger cell/stack sizes and systems with large thermal variations [6, 7].

Efforts are then required to properly assess these performance metrics of CO_2 electrolyzers by considering a spatial perspective (parameters varying in space (x,y,z), rather than an averaged 0D metric). In this perspective, we seek to shed light on the criticality of spatial variations in CO_2 electrolyzers, highlighting a body of recent studies employing operando techniques and multiphysics modelling tools that have identified these effects and their importance. We then provide instances where spatial effects can be used effectively for enhancing performance (in certain cases) and mitigating instability (current/potential distribution) for increasing the lifetime of an electrolyzer.

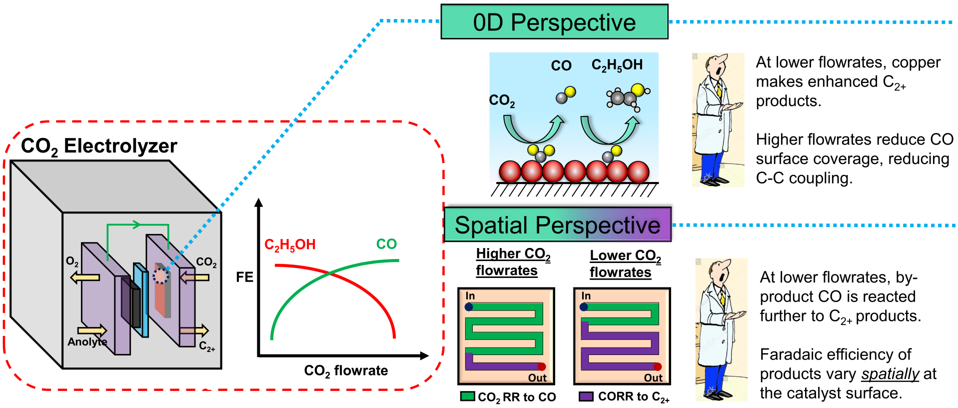

Figure 2.1: Schematic of a CO_2 electrolyzer producing CO and ethanol using a copper catalyst. Shown are the 0D and spatial perspectives and how each case can lead to different interpretation

of the observed data on faradaic efficiencies.

2.2. SPATIAL CONSIDERATIONS AND ITS RELEVANCE

2.2.1. CO_2, WATER AND PRODUCT SPATIAL VARIATIONS IN CO_2 ELECTROLYZERS

An example of a CO_2RR on a copper (Cu) catalyst producing CO and hydrocarbons at various CO_2 flowrates is shown in Figure 1. Many studies have shown that the operating flow rate can alter the product distribution, with the main observation of a higher C2 products (ethanol/ethylene) selectivity at lower flowrates [8–10]. As a first step, proper product quantification using appropriate techniques are essential to calculate the selectivities accurately. However, interpretation of the obtained data at this point without looking inside the 'black box' might lead to misinterpretation of the actual phenomena occurring at the catalyst surface.

A '0D perspective' (as shown in figure 1) might then lead to a possible conclusion that an excessive CO_2 supply reduces C-C coupling due to decreased CO coverage by the excess CO_2 molecules which leads to insufficient sites for dimerization of two CO molecules. The CO coverage then becomes the primary factor influencing C-C coupling rates and this can only be confirmed when looking at the reaction beyond 0D and 1D. In contrast, taking a spatial perspective might reveal an alternate hypothesis of a higher reactant residence time and spatial faradaic efficiency (FE) across the catalyst and gas channel as an alternate explanation for the overall product selectivity and the C_2 product mix. These spatial differences in product selectivity will further be amplified when electrolyzers are scaled to large areas.

Firstly, the existence of selectivity gradients for CO_2RR products along the length of the reactor have been shown in recent studies, suggesting the importance of spatial perspective while performing electrochemical studies and interpreting obtained results. Simonson et.al [11] showed such spatial faradaic efficiencies exist for a copper catalyst performing direct CO electrolysis to C_{2+} products by direct measurement of products within a reactor using a segmented cell. Spatial differences in ethylene and H_2 partial current densities were observed at various inlet flow rates and CO partial pressures, explaining why a 0D 'device averaged FE' may be insufficient to explain these results.

Secondly, such spatial perspective can be beneficial to tune coverage of by-products like CO on a Cu catalyst surface to maximize C_{2+} production. This strategy has been shown widely in a number of studies employing tandem Ag/Cu or Zn/Cu catalyst systems to tune CO coverage and enhance C_{2+} production [12–14]. For instance, Zhang et.al designed a segmented Cu/Ag GDE (s-GDE) and found that a CO selective catalyst near the inlet (Ag) of the reactor and a Cu catalyst at subsequent segments maximizes C_{2+} partial current densities to $> 1A/cm^2$ [15]. The strategy of controlling spatial management of by-products like CO shows how having a spatial perspective of electrochemical systems can be beneficial in designing effective catalyst layers for enhanced product formation rates especially when reactors are scaled up.

In addition to product selectivities, variation in the concentration of reactants across the reactor have been shown to affect the performance of a CO_2 electrolyzer. Wheeler et.al showed that the water concentration at the catalyst-membrane interface remained a constant in a MEA electrolyzer employing a Ag catalyst and humidity at the cathode feed was found to affect the production of CO significantly [16]. Using humidity sensors in the reactor and a numerical transport model, they showed that humidity at the cathode inlet feed modulated the flux of water transport and potassium cations crossover from the anode to cathode.

This has implications for water management in MEA reactors which play a role in two main failure mechanisms: flooding of the carbon GDE and (bi) carbonate precipitation at the cathode. A proper understanding of water management and associated trade-offs in water concentrations at the cathode side are then essential for improving lifetime of these electrolyzers. In addition to concentrations of reactants (CO_2, H_2O), it is important to emphasize here that a variation in concentration of ions (K^+, OH^-, HCO_3^- and CO_3^{2-}) at the catalyst microenvironment also alter reaction rates. For example, higher local cation concentration around the catalyst surface is known to increase C-C coupling and C_{2+} product formation rates in Cu based MEA reactors in both alkaline and acidic conditions.

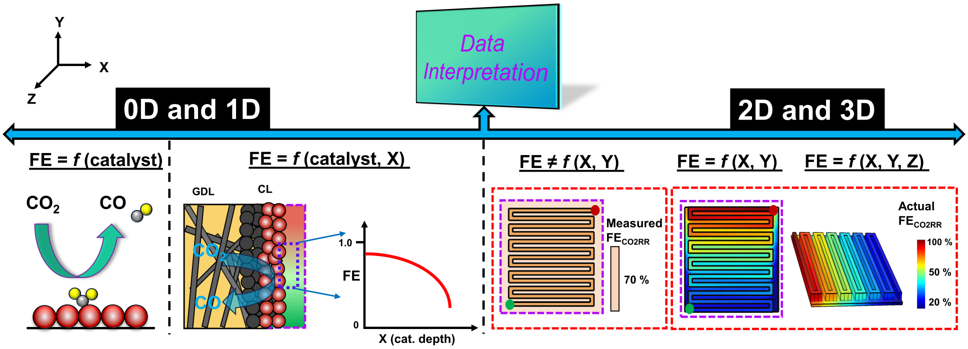

Figure 2.2: Schematic of a CO_2 electrolyzer producing CO and the perspective of faradaic efficiencies(FE) in different dimensions. While device averaged FE remains the same, the actual FE across the catalyst vary at different regions.

2.3. OPERANDO VISUALIZATION OF SPATIAL EFFECTS

While spatial variations can be inferred from 'black box' data and numerical models or probed with in-cell measurement points using humidity sensors or in-channel product quantification, these approaches still approximate or infer spatial effects. Direct measurement of spatial effects both in-plane and through the catalyst layer remains essential. Here operando techniques such as in-situ X-ray diffraction (XRD), Neutron diffraction, Raman spectroscopy and Infrared Thermography have just begun to probe CO_2 electrolyzers despite their usage in adjacent electrochemical fields. Here we will discuss these techniques and encourage their adopted use.

Firstly, Moss et. al used in-situ XRD studies in a Cu based anion exchange membrane (AEM) electrolyzer and observed the evolution of bicarbonate formation within the GDE [17], which leads to salt precipitation and an oscillatory decline in the rates of CO_2RR (Figure 2.3b). These results not only provide insights into flooding of the GDE and subsequent decline in the performance, but also help in understanding ion transport mechanisms in AEMs under CO_2RR conditions, which are beneficial for designing AEMs specifically suited for CO_2 electrolyzers.

Disch et.al [18] used neutron-diffraction technique in a zero gap MEA reactor and found that areas under the rib/land regions showed higher CO_2RR activity than at the gas flow field regions, due to higher water concentrations at the rib regions (Figure 2.3b). Our previous work on the influence of gas flow field pattern on CO production also showed that a higher pressure drop at the cathode side generated by a serpentine flow pattern resists electrolyte flooding the GDE, prolonging the lifetime of the electrolyzer [19]. Design of proper gas flow field designs, rib spacing and humidification are then crucial considerations for the development of stable CO_2 electrolyzers.

In addition to these spatial variation in species concentrations, proper quantification of pH gradients around the catalyst coated GDL are essential as the competing HER and products like CH_4 are known to be pH dependent. This is where 1D reaction diffusion models have greatly enabled researchers to estimate pH gradients at various operating conditions and reactor configurations [20–23]. Experimentally, a few studies have used operando techniques to estimate pH gradients around the catalyst surface in GDE flow cells. A study by Lu et.al using operando Raman spectroscopy in a GDE flow cell showed direct observation of pH gradients and the results were in good agreements with their reaction diffusion models [24].

As electrolyzers are scaled up, this technique may however prove to be challenging since the electrochemical cell in this study was immersed in DI water during measurements. Another similar study by Bohme et.al showed maps of local pOH around the catalyst surface using confocal laser scanning microscopy (CLSM) and observed a higher pH in the micro-trenches of the GDE [25]. While each of these techniques come with its own advantages and disadvantages in terms of cell designs and spatial resolutions in space and time, we posit that the use of one of these techniques might greatly benefit from combining it with a reaction diffusion model for proper estimation of pH gradients around the catalyst surface.

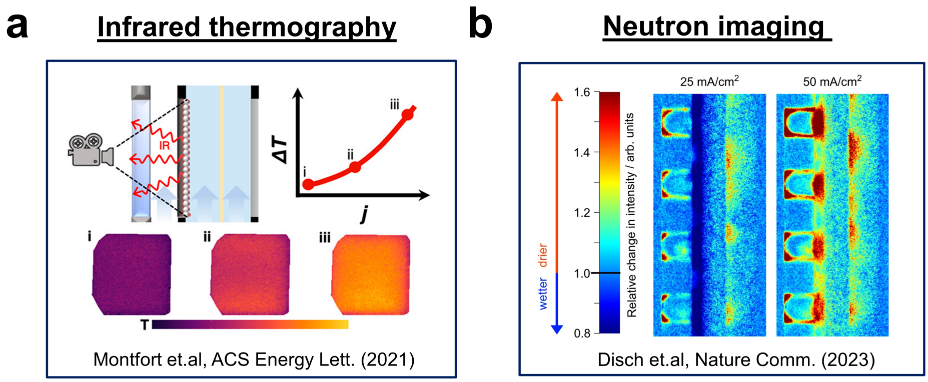

Infrared thermography

Montfort et.al, ACS Energy Lett. (2021)

Neutron imaging

Disch et.al, Nature Comm. (2023)

Figure 2.3: Operando techniques uses to measure spatial variations in CO$_2$ electrolyzers. (a) An infrared thermography technique employed to measure temperature gradients in CO$_2$ electrolyzer. (b) (a) Neutron diffraction study performed in a MEA electrolyzer. Figures adapted with permission from Refs[[18, 26]].

The aforementioned operando techniques showed how each of can be useful for measuring spatial variations in species concentrations and pH gradients around the catalyst surface. Notably, these metrics can be collectively termed as extrinsic properties of a CO$_2$RR catalyst which directly do not depend on the catalyst used. However, an intrinsic property of a catalyst do not change at a given temperature and pressure and it is usually assumed that the catalyst temperature is similar to the operating temperature of an electrolyzer. This is unfortunately not the case during high current density operating conditions, as a significant amount of heat is generated due to joule heating and exothermic reaction of CO$_2$ with hydroxide ions. A technique like infrared thermography can then become beneficial to properly account of these heat losses and temperature distribution inside various parts of an electrolyzer.

Montfort et.al used an infrared thermography to probe the local heat generated in a catalyst coated GDL by using an IR camera from the back of the GDE flow cell [26]. At higher current densities during CO$_2$RR at ambient temperature, a Ag catalyst was found to be >10 K hotter than the operating temperature. This has serious implications for data interpretation since higher temperatures not only alter the extrinsic properties as shown earlier, but also defy the assumed intrinsic properties like exchange current densities and turn over frequencies (TOF) of the catalyst at standard conditions. As industrial CO$_2$ electrolyzers are likely to be operated at much higher current densities, it is important to understand that catalyst during operation might be significantly hotter than the electrolyzer itself. Once again, this study shows why considering electrochemical reactions in multiple dimensions are beneficial for proper data interpretation and understanding of the actual phenomena occurring inside the electrolyzer.

2.4. LOOKING FURTHER: GDE AS A 3D REGION

An important realization, in addition to the variation of the nature of catalyst in the 2D-plane, is the intrinsic complexity of the catalyst layer in the third dimension. The plethora of deposition methods reported in literature result in an equally complex landscape of electrode topologies. In a system that is very sensitive to local concentration of reactants, tortuosity of the fluid phase, and basicity, this leads to a blurred understanding of observed effects at play during CO_2RR. For added complexity, some catalysts, like copper, show an inherent instability that results in shifting product selectivity in time. These issues highlight the importance of understanding the role of our catalyst layer in the reaction system and the influence the deposition technique has on the performance metrics.

In a drive to tackle the instability of some catalysts, it can be enticing to 'overload' the electrode with active particles. This prevents the catalyst activity from being a bottleneck in bench-top tests in a lab environment. Since catalyst loading is often overlooked as a variable in electrode development for CO_2RR, this practice goes mostly unnoticed. If one imagines a catalyst layer as a region with a progressively deactivating regime, a thicker catalyst layer benefits the stability of the system overall. This comes at a cost of a thicker catalyst layer, but the reduced increase in this dimension relative to the overall cathode size seems a valid compromise.

The problem of this blind-spot in literature comes when constant-potential tests are performed. Two electrodes with the same active catalyst but dissimilar loadings will display different current densities when subjected to the same polarization. In addition, the common practice in the CO_2RR field is to condense current densities to a 2D-geometric area, disregarding the electrochemical active surface area (ECSA). This draws unrealistic performance metrics of catalytic materials by ignoring the third depth dimension in electrode development. Factors such as catalyst porosity, catalyst loading and catalyst layer thickness affect the ECSA and values of these parameters must be reported in future works.

CURRENT DISTRIBUTION IN GAS DIFFUSION ELECTRODES

An often overlooked, besides that of catalyst loading, is that of current collection in gas-diffusion electrodes [27]. Assumed is that the carbonous substrate of most gas-diffusion layers is sufficiently conductive. The state of the CO_2RR field has not yet triggered output that could be confronted with poor current collection, since most output is performed on electrodes with a total surface area in the range of 1–5cm^2. These assumptions might however soon be challenged by two separate developments. On the one hand, the move towards high current-density and surface area systems is moving the bottleneck of current-flow from the catalyst to the supporting interface (in this case, the GDE) and its anisotropy of current collection. On the other hand, irruption of alternative GDL-materials like expanded polytetrafluoroethylene (ePTFE) might complicate current collection and form a bottleneck at even smaller scales.

2.5. FUTURE OUTLOOK

We have discussed the benefits of looking at a GDE as a 3D region for proper consideration of the spatial effects arising in the electrolyzer. As technology matures and more focus is placed on understanding spatial effects, there will be further opportunities to effectively design gas diffusion electrodes for CO_2 electrolysis. While PTFE based electrodes have shown great promise for maintaining stability and obtaining increased reaction rates, for industrial applications, carbon based GDEs are essential both due to the ease of manufacturing and the ability to distribute currents uniformly throughout the electrode. Further, the extensive knowledge on spatial effects from PEM water electrolyzers and fuel cells might be beneficial to accelerate the CO_2 electrolysis field forward.

The field must then advance in an approach that is threefold: on the one hand, focus on interfacial design to accommodate the sought process conditions is needed. Secondly, experimental design should take local effects in the electrolyzer into account, like elevated local temperatures and varying humidity. Finally, the field needs standardization in reporting catalyst loadings and designs, to achieve a one-to-one comparison like that present in the Li-battery field.

REFERENCES

[1] D. Wakerley, S. Lamaison, J. Wicks, A. Clemens, J. Feaster, D. Corral, S. A. Jaffer, A. Sarkar, M. Fontecave, E. B. Duoss, *et al.* “Gas diffusion electrodes, reactor designs and key metrics of low-temperature CO2 electrolysers”. In: *Nature Energy* 7.2 (2022), pp. 130–143.

[2] R. I. Masel, Z. Liu, H. Yang, J. J. Kaczur, D. Carrillo, S. Ren, D. Salvatore, and C. P. Berlinguette. “An industrial perspective on catalysts for low-temperature CO2 electrolysis”. In: *Nature nanotechnology* 16.2 (2021), pp. 118–128.

[3] R. Küngas. “electrochemical CO2 reduction for CO production: comparison of low-and high-temperature electrolysis technologies”. In: *Journal of The Electrochemical Society* 167.4 (2020), p. 044508.

[4] A. Raya-Imbernón, A. A. Samu, S. Barwe, G. Cusati, T. Fődi, B. M. Hepp, and C. Janáky. “Renewable Syngas Generation via Low-Temperature Electrolysis: Opportunities and Challenges”. In: *ACS Energy Letters* 9 (2023), pp. 288–297.

[5] H.-P. Iglesias van Montfort, S. **Subramanian**, E. Irtem, M. Sassenburg, M. Li, J. Kok, J. Middelkoop, and T. Burdyny. “An Advanced Guide to Assembly and Operation of CO_2 Electrolyzers”. In: *ACS Energy Letters* 8.10 (2023), pp. 4156–4161.

[6] R. Kas, A. G. Star, K. Yang, T. Van Cleve, K. C. Neyerlin, and W. A. Smith. “Along the channel gradients impact on the spatioactivity of gas diffusion electrodes at high conversions during CO2 electroreduction”. In: *ACS Sustainable Chemistry & Engineering* 9.3 (2021), pp. 1286–1296.

[7] S. **Subramanian**, J. Middelkoop, and T. Burdyny. “Spatial reactant distribution in CO_2 electrolysis: balancing CO 2 utilization and faradaic efficiency”. In: *Sustainable Energy & Fuels* 5.23 (2021), pp. 6040–6048.

[8] H. Song, J. T. Song, B. Kim, Y. C. Tan, and J. Oh. “Activation of C2H4 reaction pathways in electrochemical CO2 reduction under low CO2 partial pressure”. In: *Applied Catalysis B: Environmental* 272 (2020), p. 119049.

[9] C. M. Gabardo, C. P. O’Brien, J. P. Edwards, C. McCallum, Y. Xu, C.-T. Dinh, J. Li, E. H. Sargent, and D. Sinton. “Continuous carbon dioxide electroreduction to concentrated multi-carbon products using a membrane electrode assembly”. In: *Joule* 3.11 (2019), pp. 2777–2791.

[10] Y. C. Tan, K. B. Lee, H. Song, and J. Oh. “Modulating local CO2 concentration as a general strategy for enhancing C- C coupling in CO2 electroreduction”. In: *Joule* 4.5 (2020), pp. 1104–1120.

[11] H. Simonson, W. E. Klein, D. Henckel, S. Verma, K. Neyerlin, and W. A. Smith. “Direct Measurement of Electrochemical Selectivity Gradients over a 25 cm2 Copper Gas Diffusion Electrode”. In: *ACS Energy Letters* 8.9 (2023), pp. 3811–3819.

[12] B. Zhang, L. Wang, D. Li, Z. Li, R. Bu, and Y. Lu. “Tandem strategy for electrochemical CO2 reduction reaction”. In: *Chem Catalysis* 2.12 (2022), pp. 3395–3429.

[13] T. Zhang, Z. Li, J. Zhang, and J. Wu. “Enhance CO2-to-C2+ products yield through spatial management of CO transport in Cu/ZnO tandem electrodes”. In: *Journal of catalysis* 387 (2020), pp. 163–169.

[14] C. G. Morales-Guio, E. R. Cave, S. A. Nitopi, J. T. Feaster, L. Wang, K. P. Kuhl, A. Jackson, N. C. Johnson, D. N. Abram, T. Hatsukade, *et al.* “Improved CO2 reduction activity towards C2+ alcohols on a tandem gold on copper electrocatalyst”. In: *Nature Catalysis* 1.10 (2018), pp. 764–771.

[15] T. Zhang, J. C. Bui, Z. Li, A. T. Bell, A. Z. Weber, and J. Wu. “Highly selective and productive reduction of carbon dioxide to multicarbon products via in situ CO management using segmented tandem electrodes”. In: *Nature Catalysis* 5.3 (2022), pp. 202–211.

[16] D. G. Wheeler, B. A. Mowbray, A. Reyes, F. Habibzadeh, J. He, and C. P. Berlinguette. “Quantification of water transport in a CO 2 electrolyzer”. In: *Energy & Environmental Science* 13.12 (2020), pp. 5126–5134.

[17] A. B. Moss, S. Garg, M. Mirolo, C. A. G. Rodriguez, R. Ilvonen, I. Chorkendorff, J. Drnec, and B. Seger. “In operando investigations of oscillatory water and carbonate effects in MEA-based CO2 electrolysis devices”. In: *Joule* 7.2 (2023), pp. 350–365.

[18] J. Disch, L. Bohn, L. Metzler, and S. Vierrath. “Strategies for the mitigation of salt precipitation in zero-gap CO 2 electrolyzers producing CO”. In: *Journal of Materials Chemistry A* (2023).

[19] S. **Subramanian**, K. Yang, M. Li, M. Sassenburg, M. Abdinejad, E. Irtem, J. Middelkoop, and T. Burdyny. “Geometric Catalyst Utilization in Zero-Gap CO_2 Electrolyzers”. In: *ACS Energy Letters* 8.1 (2022), pp. 222–229.

[20] T. Moore, X. Xia, S. E. Baker, E. B. Duoss, and V. A. Beck. “Elucidating mass transport regimes in gas diffusion electrodes for CO2 electroreduction”. In: *ACS Energy Letters* 6.10 (2021), pp. 3600–3606.

[21] T. Burdyny and W. A. Smith. “CO 2 reduction on gas-diffusion electrodes and why catalytic performance must be assessed at commercially-relevant conditions”. In: *Energy & Environmental Science* 12.5 (2019), pp. 1442–1453.

[22] D. Raciti, M. Mao, and C. Wang. “Mass transport modelling for the electroreduction of CO2 on Cu nanowires”. In: *Nanotechnology* 29.4 (2017), p. 044001.

[23] L.-C. Weng, A. T. Bell, and A. Z. Weber. “Modeling gas-diffusion electrodes for CO 2 reduction”. In: *Physical Chemistry Chemical Physics* 20.25 (2018), pp. 16973–16984.

[24] X. Lu, C. Zhu, Z. Wu, J. Xuan, J. S. Francisco, and H. Wang. “In situ observation of the pH gradient near the gas diffusion electrode of CO2 reduction in alkaline electrolyte”. In: *Journal of the American Chemical Society* 142.36 (2020), pp. 15438–15444.

[25] A. Böhme, J. C. Bui, A. Q. Fenwick, R. Bhide, C. N. Feltenberger, A. J. Welch, A. J. King, A. T. Bell, A. Z. Weber, S. Ardo, *et al.* “Direct observation of the local microenvironment in inhomogeneous CO 2 reduction gas diffusion electrodes via versatile pOH imaging”. In: *Energy & Environmental Science* 16.4 (2023), pp. 1783–1795.

[26] H.-P. Iglesias van Montfort and T. Burdyny. “Mapping Spatial and Temporal Electrochemical Activity of Water and CO2 Electrolysis on Gas-Diffusion Electrodes Using Infrared Thermography”. In: *ACS Energy Letters* 7.8 (2022), pp. 2410–2419.

[27] H.-P. Iglesias van Montfort, M. Li, E. Irtem, M. Abdinejad, Y. Wu, S. K. Pal, M. Sassenburg, D. Ripepi, S. **Subramanian**, J. Biemolt, *et al.* “Non-invasive current collectors for improved current-density distribution during CO2 electrolysis on super-hydrophobic electrodes”. In: *Nature Communications* 14.1 (2023), p. 6579.

3

SPATIAL REACTANT DISTRIBUTION IN CO_2 ELECTROLYSIS

Science progresses best when observations force us to alter our preconceptions.

- Vera Rubin

The production of value added C1 and C2 compounds within CO_2 electrolyzers has reached sufficient catalytic performance that system and process performance such as CO_2 utilization have come more into consideration. Efforts to assess the limitations of CO_2 conversion and crossover within electrochemical systems have been performed, providing valuable information to position CO_2 electrolyzers within a larger process. Currently missing, however, is a clear elucidation of the inevitable trade-offs that exist between CO_2 utilization and electrolyzer performance, specifically how the faradaic efficiency of a system varies with CO_2 availability. In this work, we provide a combined experimental and 3D modelling assessment of the trade-offs between CO_2 utilization and selectivity at 200 mA/cm^2 within a silver based membrane-electrode assembly CO_2 electrolyzer. Using varying inlet flow rates, we demonstrate that the variation in spatial concentration of CO_2 leads to spatial variations in faradaic efficiency that cannot be captured using common 'black box' measurement procedures. Specifically, losses of faradaic efficiency are observed to occur even at incomplete CO_2 consumption (80 %). Modelling of the gas channel and diffusion layers indicated that at least a portion of the H_2 generated is considered as avoidable by proper flow field design and modification. The combined work allows for a spatially resolved interpretation of product selectivity occurring inside the reactor, providing the foundation for design rules in balancing CO_2 utilization and device performance in both lab and scaled applications.

This chapter has been published as "Spatial reactant distribution in CO_2 electrolysis: balancing CO_2 utilization and faradaic efficiency" by Siddhartha Subramanian, Joost Middelkoop, Thomas Burdyny. *Sustainable Energy Fuels*, 2021,5, 6040-6048.

3.1. INTRODUCTION

One of the emerging technologies to mitigate fossil fuel-based carbon emissions is the electrochemical conversion of CO_2 to fuels and value-added products. In electrochemical CO_2 reduction, an electric potential is applied in the presence of an appropriate catalyst to convert CO_2 and H_2O to syngas ($CO+H_2$), ethylene (C_2H_4), ethanol (C_5H_2OH) and formate ($HCOO^-$) among other products.[1–3] To meaningfully mitigate CO2 emissions and be cost-competitive with alternative production routes, CO_2 electrolyzers will need to be proven as scalable to global production rates on the order of 100's Mtons/year.[4–6] While water electrolyzers are developmentally able to reach such scales, CO_2 electrolyzers are at a much earlier stage of development. Thus, while producing an anthropogenic carbon cycle composed of converting atmospheric CO_2 to fuels using solar and other renewable energy sources is appealing, additional research and development is needed to improve the performance metrics and scale of the technology for it to become a viable option.[7–9]

To perform research into CO_2 electrolyzers at increased production rates, a greater fraction of research has taken place under elevated current densities (> 100 mA/cm^2), using either high pressure systems or gas diffusion electrodes to enhance the availability of CO_2 at the catalyst surface. Gas diffusion electrodes (GDE) in particular have been found to be promising due to their ease of operation at atmospheric conditions which lowers the barrier for research to adopt their use.[10–12] When paired with novel catalyst architectures and cell designs, CO_2 electrolysis on GDE's has then achieved current densities on the order of 1A/cm^2 for promising products such as both CO[13] and ethylene [14] with reasonable faradaic efficiencies and cell voltages. Additionally, some researchers have begun discussing the importance of CO_2 utilization (as known as single-pass conversion efficiency) within such systems. Separate works have assessed the maximum conversion for a given configuration,[15] the crossover of the CO_2 to the anode as carbonate, [16] and the observed drop in faradaic efficiency at higher CO_2 utilizations.[17] Such research has made it clear that trade-offs will ultimately exist between the traditional performance metrics of the CO_2 electrolyzer itself (current density, Faradaic efficiency, overpotential), and the efficiency and cost of the entire CO_2 conversion process consisting of upstream and downstream processes.[18]

The balance between CO_2 utilization and faradaic efficiency is particularly interesting as these metrics are directly impacted by the gas flow rate, the applied current density, temperature and the electrolyte alkalinity, all of which affect the CO_2 that is available for conversion. For example, Jeng at al.[15] highlighted the trade-off between partial current density for CO and the fraction of CO_2 converted to products for a 25 cm^2 membrane-electrode assembly (MEA) CO_2 electrolyzer under various operating conditions, noting a consistent maximum CO_2 utilization of 43 % for the given reaction. While such observations provide valuable information around CO_2 utilization in such systems, the trade-off in faradaic efficiency with CO_2 utilization under varying CO_2 concentrations has received less attention and is less well-described. Specifically, while the CO_2RR faradaic efficiency of a system under excess flow conditions can be determined using either a high gas flow rate or a very small geometric surface area (e.g. < 1 cm^2), the selectivity of the system under decreasing CO_2 partial pressures is less clear with only a few studies available[19]. Importantly, as the surface area of standard test cells increases, *the concentration of CO_2 will also vary spatially throughout the reactor,* leading to spatial differences in reactivity and faradaic efficiency that will need to be understood to scale-up and optimize the technology.

While the influence of spatial reactant distribution on performance has not been well-investigated in the CO_2 electrolysis community, there is a wealth of research in the fuel cell community assessing the influence of reactant concentrations, flow patterning and under-rib convection on efficiency, utilization and mass transport on the overall performance of the device.[20–23] Using previous electrochemical fields as a guidepost, it is apparent that understanding the spatial variation of selectivity within a CO_2 electrolyzer device will also be an essential step towards scaling-up such devices as well as choosing configurations which maximize CO_2 utilization without unnecessary penalties in selectivity. For CO_2 electrolysis, these efforts are complicated by competing and homogenous reactions which poses additional challenges as compared to well-studied parallel electrochemical fields. There is also less data presently available evaluating the performance differences between different flow fields for the gaseous CO_2 channel as most research is performed using smaller geometric catalyst areas and a fully open cavity.

Here we sought to provide a framework for how reactant flowrate and spatial CO_2 distribution impacts product selectivity at higher CO_2 utilizations using a well-utilized electrochemical testing platform. Firstly, we performed CO_2 electrolysis using a silver (Ag) gas diffusion electrode in a 5 cm^2 MEA at various reactant flowrates to determine the macroscopic influence on product selectivity. From these experiments a ‘black box’ evaluation of faradaic efficiencies (FE) at various CO_2 utilizations is defined. We then built a 3D mass transport model of the cathode side of the MEA to estimate the spatial CO_2 distribution inside the reactor and catalyst layer under each of the varying flow conditions to convert the ‘black box’ results of the CO_2 distribution throughout the 5 cm^2 cell into a more spatially resolved interpretation of reactant concentration at the catalyst’s surface (Fig.1). Finally, we show that by using a combined experimental and modelling approach, the influence of reactant flowrate and spatial CO_2 distribution can in turn be used to predict a spatial product selectivity across the device. Once defined, such a combined experimental and modelling system can then be used to predict the impacts of varying flow fields, cell areas and current densities, providing the groundwork for designing and prototyping CO_2 electrolyzers which balance CO_2 utilization with product selectivity.

3.2. RESULTS AND DISCUSSION

Product quantification within gaseous-fed CO_2 electrolyzers is presently performed by measuring the composition of the outlet gas phase using a gas chromatography (GC), and measuring the composition of the liquid electrolyte phases using nuclear magnetic resonance spectroscopy (NMR) or high performance liquid chromatography (HPLC). Such measurements provide a point-in-time 'black box' interpretation of the FE at a given flow rate, current density and configuration that can be monitored through periodic measurements (Figure 1a). At elevated inlet flow rates where CO_2 utilizations are low, the outlet gas stream remains > 90% CO_2 and it is subsequently assumed that ample CO_2 can reach the entire catalytic surface area. In other words, no specific area of the catalyst surface exhibits mass transport limitations and the Faradaic Efficiency is assumed to be equal across the entire catalyst area (e.g. FE $\neq$ f(x,y)). Such an assumption is particularly valid for smaller catalyst areas, high CO_2 flow rates and open cavity gas channels which are assumed as well-mixed and maintained at similar temperature and pressures.

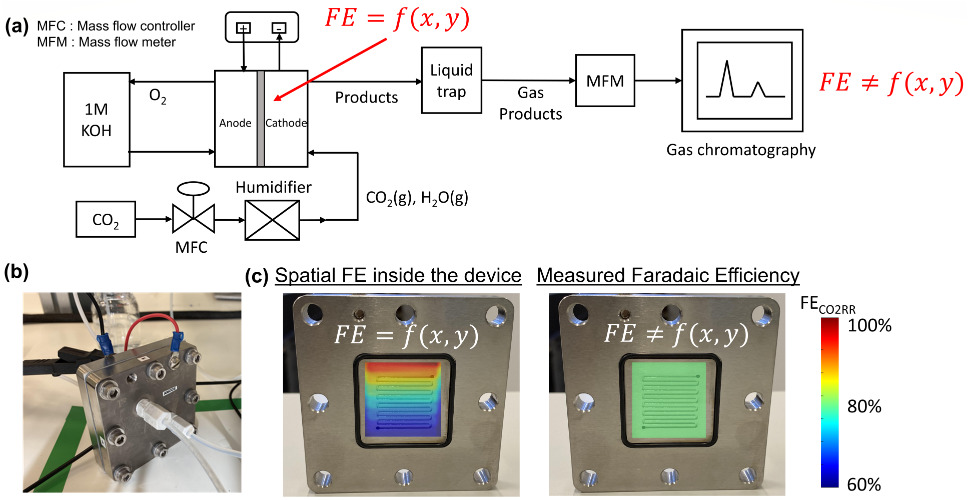

Figure 3.1 : (a) Simplified schematic of the experimental setup used for CO_2 electroreduction to CO in a membrane electrode assembly (MEA). (b) Figure of the experimental MEA utilized in the work. (c) Overlaid schematic of the actual vs measured Faradaic Efficiency of a CO_2 electrolysis system under CO_2-limited operating flow rates for the serpentine flow fields used for CO_2 flow behind a gas-diffusion layer.

As industrial and lab geometric cell areas increase, CO_2 must be distributed to the GDL and catalyst area through flow fields, which are also critically acting as a current collector to ensure homogenous electrode potentials. Within these CO_2 flow channels, the reactant and product compositions will then change along the length of each flow channel [24] as the catalyst consumes CO_2 and produces products such as CO and H_2. In cases where CO_2 utilizations are increased, spatial variations in performance and selectivity will occur when areas of the catalyst no longer have access to sufficient CO_2, and produce unwanted H_2 instead (see Fig. 1b for representation) [25–27]. To begin assessing this trade-off we first collected a data set under varying flow rate conditions for CO_2 conversion to carbon-monoxide (CO) on a silver (Ag) catalyst in a membrane-electrode assembly with a serpentine flow field of 5 cm^2 geometric area (Figure3.6).

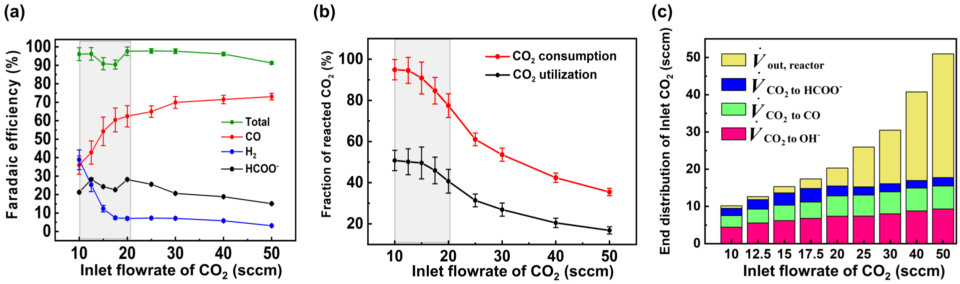

Figure 3.2 : (a) Faradaic efficiency of products for various inlet flow rates performed at a current density of 200 mA/cm2. CO_2 utilization and CO_2 consumption for different inlet flowrates at 200 mA/cm^2. Greyed regions represent trade-offs between utilization and selectivity. (c) Carbon balance on cathode showing the volumetric flowrate of CO_2 consumed to different reactions.

3.2.1. TRADE OFFS IN CO_2RR AND SINGLE PASS CO_2UTILIZATION

For the data set we performed electrolysis at a constant current density of 200 mA/cm^2 for 3600 seconds at inlet CO_2 flowrates between 10 and 50 sccm. The gas products and unreacted CO_2 were quantified using a mass-flow metre (MFM) and GC installed at the exit of the reactor (Figure 3.1a). As shown in Figure 3.2(a), we found that at excess flow rates between 20 and 50 sccm the Faradaic efficiency of CO_2 reduction products (CO and formate) was maintained between 93-97%, indicating that sufficient reactant is available throughout the system. At lower flow rates (< 20 sccm), however the FE of hydrogen begins increasing steadily with increasing CO_2 utilization, reaching an H_2 selectivity of 38.9 % at 10 sccm and a measured CO_2 utilization of 50 % (Figure 3.2b).

Over the entire examined region, CO_2 utilization decreases with an increase in the inlet flowrate from 50.8 % at 10 sccm to 16.8 % at 50 sccm as shown in Figure 3.2(b). The highlighted grey region in Figure 3.2a and 3.2b represents the likely operating region of a commercial CO_2 electrolyzer as it best balances selectivity and utilization. Understanding and quantifying the performance trade-off is necessary to manufacture performance curves for CO_2 electrolyzers, similar to other applications where trade-offs exist (e.g. centrifugal pumps). Such data is essential for positioning CO_2 electrolyzers within integrated process and cost models that assess a broad operational parameter space. Additionally, better design of the reactant flow fields and gas-diffusion layers may improve performance further.

To better quantify the trade-off in utilization and selectivity, the available CO_2 for reduction in the system must be known. To track this a carbon balance of the system is performed at various flow rates (Figure 3.2c). In this analysis the inlet and outlet flow rates of CO_2, CO and formate are all measured directly, with the exception of CO_2 crossing the membrane as carbonate ions which was assumed to complete the carbon balance. Observing the trends in carbon flow rates, two interesting points arise. First, even under low flow rates of 10 sccm, some CO_2 is observed in the outlet of the reactor (5% /v) even though the reaction appears CO_2-limited. This indicates a measure of transport limitations between the serpentine gas channel and the catalyst's surface as a result of transport through the gas-diffusion media and into the catalyst layer. And second, the consumption of CO_2 by OH^- ions is non-linear and varies with the availability of CO_2 throughout the reactor. Both of these observations can be qualitatively interpreted from the presented data, but lack a quantitative interpretation in their present form as a result of the 'black box' measurement approach. Thus, a numerical transport model built upon the experimental results can be used to provide further understanding.

3.2.2. MODELLING CO_2 SPATIAL DISTRIBUTION

To gain deeper understanding of the reactant distribution inside the reactor, a 3D model of the mass transport and fluid flow in the cathode compartment of the MEA cell was created using COMSOL Multiphysics (Figure 3.3a). The ultimate goal of the model is to provide a simple estimate of the concentration of CO_2 at the surface of the catalyst layer for various operating conditions, which can then be used to predict a spatial and average Faradaic efficiency ($FE = f(x,y)$ and $FE_{average}$). The predicted average FE of the system in particular provides a comparison to the experimental data, while the spatial assessment is useful to advance performance further and for the design of scaled systems beyond 5 cm^2. Included within the model are the CO_2 serpentine gas channel and a gas-diffusion layer composed of a carbon fibre backing and a microporous layer (Figure S6). The gas-diffusion electrode is then modelled as a porous media similar to other works [28].

In the model, an inlet flux of CO_2 is provided to the system in the gas channel, while a fixed current density is imposed at the surface of the gas-diffusion electrode to model the electrochemical reactions and consumption of CO_2 by the electrolyte. The physical parameters and properties used in the model are shown in Table S5. Due to the complexity of constructing a fully-representative macroscopic and nanoscopic transport model, we have chosen to set our system boundaries at the interface of the microporous layer and the catalyst layer. The model then does not directly take into account the interaction between the catalyst layer and the membrane, 3D transport effects within the nanopores of the catalyst layer, or the homogenous $CO_2/HCO_3^-/CO_3^{2-}$ reactions occurring within the liquid water and Sustainion membrane.

To account for this, we have constructed three modelling scenarios using experimental mass flows as inputs to construct different empirical models that highlight the effect of different scenarios on CO_2 distribution. The most representative system is then used to continue the discussion on CO_2 utilization and Faradaic Efficiency.

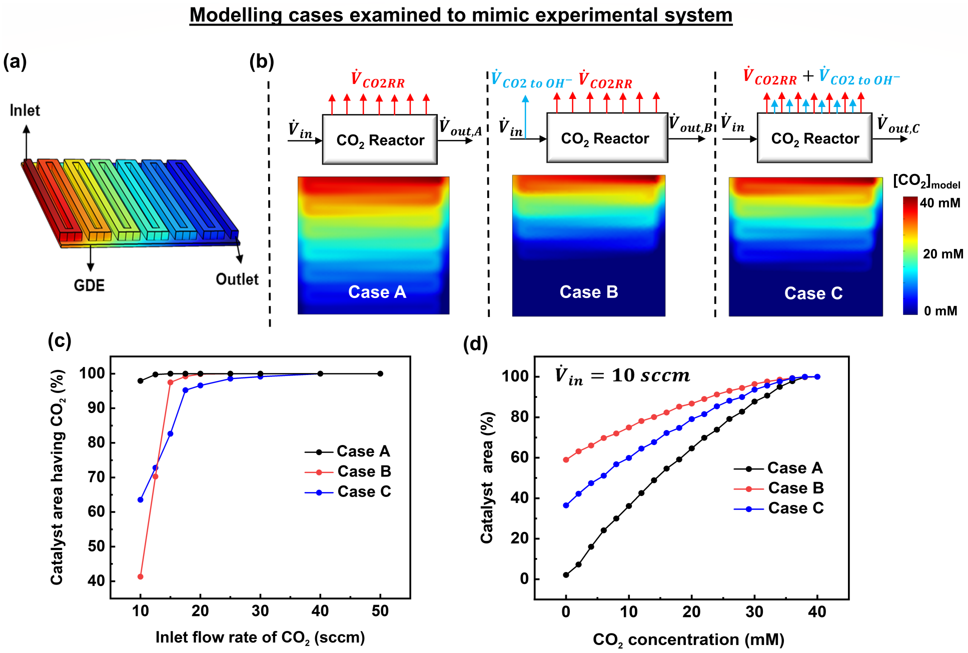

Figure 3.3 : (a) 3D model of the flow channel and gas diffusion electrode. (b) Modelling cases examined to mimic the experimental observations. Shown here are the simulation results of CO_2 concentration at the catalyst surface for an inlet flow rate of 10 sccm and 200 mA/cm^2, (c) A cumulative distribution plot for the three cases showing the [CO_2] distribution at the catalyst surface, (d) Portion of catalyst surface having access to CO_2([CO_2] > 0) for all the inlet flow rates studied experimentally.

The three examined cases are as follows: In Case A, we ignore the fraction of CO_2 reacting with hydroxide ions. In Case B, the amount of CO_2 lost to hydroxide ions is subtracted at the inlet resulting in a reduced inlet flowrate. In Case C, the fraction of CO_2 lost to hydroxide ions is assumed to occur homogeneously throughout the catalyst surface. These three cases are visually depicted in Figure 3.3b along with their resulting simulated CO_2 concentrations at the catalyst layer interface at 10 sccm and 200 mA/cm2. Figure 3.3c shows the analysed data set from Figure 3.3b represented as a cumulative distribution function for the percentage of the catalyst area with a minimum concentration of CO_2.

CASE A: MODELLING THE CATHODE WITHOUT ACCOUNTING FOR CO2 CONSUMPTION TO OH$^-$ IONS

In this approach, CO_2 losses due to its reaction with OH$^-$ ions forming bicarbonate and carbonate ions are ignored. The results obtained for an inlet flowrate of 10 sccm at 200 mA/cm^2 are shown in Figure 3.3c, where the two-dimensional data set has been converted into a cumulative distribution functions as a percentage of the geometric area of the catalyst layer. Thus the percentage of catalyst area with ample and deficient CO_2 can be visualized (Figure S8). From Figure 3.3b, it can be seen that the CO_2 concentration decreases from the inlet to the outlet of the gas channels and at the catalyst surface. As shown in Figure 3.3b, the cumulative distribution plot for CO_2 at the catalyst surface shows that only 2.1% of the catalyst area is deficit of CO_2 for an inlet flow rate of 10 sccm. Hence, Case A shows almost no CO_2 limitation indicating that this reactant feed is sufficient to sustain the current density that is applied (200 mA/cm^2). However, as could be expected, Case A clashes with the experimental observation of a low CO selectivity (35.9 %) and a relatively high H_2 selectivity (38.9 %) at 10 sccm. This discrepancy between the modelling and the experimental results shows that CO_2 losses (due to its reaction with OH^-) cannot be ignored in modelling the spatial CO_2 distribution.

CASE B: MODIFIED INLET FLOWRATE APPROACH

In Case B, the inlet boundary condition of CO_2 flux has been reduced to account for the amount of CO_2 lost to OH^- ions over the entire reactor. Here, the amount of CO_2 lost to OH^- ions was experimentally measured and subtracted from the inlet flow rate to obtain a modified inlet flow rate (Table S2). In contrast to Case A, using the modified inlet flow rate approach, a significant portion of catalyst surface (59 %) is deficit of CO_2 at 10 sccm (Fig. 3b). Although this agrees with the experimental observation of an increased H_2 production (38.9 %) at low flow rates, the change in catalyst area with access to CO_2 is too abrupt under varied flow rates (Fig. 3d), which does not pair well with the gradual change in selectivity seen in the experiments (Fig. 2a). The flaw in a modified inlet flow rate approach is that the CO_2 losses to OH^- ions are not distributed throughout the catalyst surface, meaning that the CO_2 available in the front half of the serpentine channel is unfairly limited. Case B is then too much of a simplification to predict the spatial CO_2 distribution and device selectivity accurately.

Of note, using a modified inlet flow rate would also slightly impact the fluid velocity and pressure drop between the inlet and outlet, altering the actual physical phenomena occurring inside the reactor. Such an approach would then have significant effects when large flow rates are used where a significant pressure drop might exist between the inlet and outlet of the reactor. Critically, Case B over penalizes the CO_2 concentration throughout the majority of the reactor as CO_2 lost to OH^- ions near the exit of the reactor has been removed prior to the reactor inlet.

CASE C: MODIFIED CURRENT DENSITY APPROACH

With the aim of predicting the 2D spatial CO_2 concentration in the reactor while maintaining a simplified modelling approach, Case C aimed to spatially account for CO_2 loss to OH^- ions as well. To institute this within the model without implementing pore scale phenomena and homogeneous reactions, we instead imposed a penalty current density (j_{loss}) that accounts for the additional consumption of CO_2. The magnitude of the imposed penalty current density was calculated using the experimentally-measured loss of CO_2 at each independent flow rate (Equation 3.1 and Figure 3.2c), resulting in an empirical representation of the experiment. This modified current density was then added to the actual applied current density term to provide the spatial rate of CO_2 consumption (Equation 3.2). Fig. S3 shows the modified current densities which have been imposed in the model as a result of Case C, with all current density above 200 mA/cm^2 being deployed as a non-Faradaic consumption of CO_2.

$$j_{\text{loss}} = \frac{\eta^{e} \times \eta_{\text{CO2 to OH}^-} \times F}{A} \tag{3.1}$$

$$R_{\text{CO2}} = \frac{(j_{\text{applied}} + j_{\text{loss}})}{\eta^{e} \times F} \tag{3.2}$$

Here, R_{CO2} is the reaction rate of CO_2, j_{loss} is the modified current density calculated based on the amount of CO_2 lost to OH^- ions (from experimental data), n^e is the number of electrons (2 for CO_2 RR), $n_{\text{CO2 to OH}^-}$ is the moles of CO_2 lost to OH^- , F- Faraday's constant and A is the area of the catalyst surface (6.25 cm^2). Once imposed, Case C provides the spatial distribution of CO_2 observed in Figure 3.3b for an inlet flow rate of 10 sccm. Translating this to the cumulative distribution function in Fig. 3c, the net catalyst area with no access to CO_2 is approximately 37%. Further, Figure 3.3d shows the percentage of catalyst area with access to reagent results for all of the simulated cases and flow rates. Notably at flow rates within the utilization area of interest (10-20 sccm), Case C falls in between Cases A and B. The effect of parasitic CO_2 loss is still not eliminated above 20 sccm, however, which can be attributed to poor CO_2 access on the fringes of the gas-diffusion layer. In this case, this is due to the area of the GDE (6.25 cm^2) expanding beyond the edge of the serpentine flow channel (5 cm^2). Due to accounting for spatial effects, Case C is chosen as the most representative model for the remainder of the work.

3.2.3. PREDICTED SPATIAL AND AVERAGE FARADAIC EFFICIENCY

The previous section provided a set of models to predict the spatial concentration of CO_2 within an experimentally-tested membrane-electrode assembly reactor. As the primary focus is to better understand the trade-offs between selectivity and utilization in these systems, these predicted concentrations of CO_2 must be translated to a predicted spatial and average Faradaic Efficiency. To accomplish this we imposed the following selectivity criteria in equations 3 and 4 based upon the predicted CO_2 concentration and the experimentally-measured Faradaic Efficiency under an excess CO_2 flow rate of 50 sccm (97% CO_2RR / 3% HER). The data has been normalized to 100% (96.8% CO_2RR / 3.2% HER) for the purposes of the model.

$$FE_{\text{CO2RR}}(x,y) = \begin{cases} 96.8\%, & [CO_2 > 0] \\ 0\%, & [CO_2 = 0] \end{cases} \tag{3.3}$$

$$FE_{\text{H2}}(x,y) = \begin{cases} 3.2\%, & [CO_2 > 0] \\ 100\%, & [CO_2 = 0] \end{cases} \tag{3.4}$$

Using this criteria, the spatial Faradaic Efficiency across the catalyst layer of the GDE is visually shown in Figure 3.4a for three different flow rates. Observing the low flow rate case of 10 sccm, the loss of selectivity towards CO_2RR is shown to be primarily due to insufficient CO_2 along the length of the reactor towards the outlet. In the 20 sccm case, however, it is only the edges near the outlet of the reactor that are expected to primarily produce H_2 instead of CO_2RR products. In an actual system the switch in selectivity from primarily CO_2RR to H_2 along the reactor of CO_2-deficient system would be more gradual, but high selectivities are known to be possible even at lower partial pressures[29]. From Figure 3.17, we predict that there would be a third transition region at 0-3 mM CO_2 concentration. A secondary check of the approach is to translate the spatially-predicted Faradaic Efficiency into a device-averaged FE like that reported experimentally.

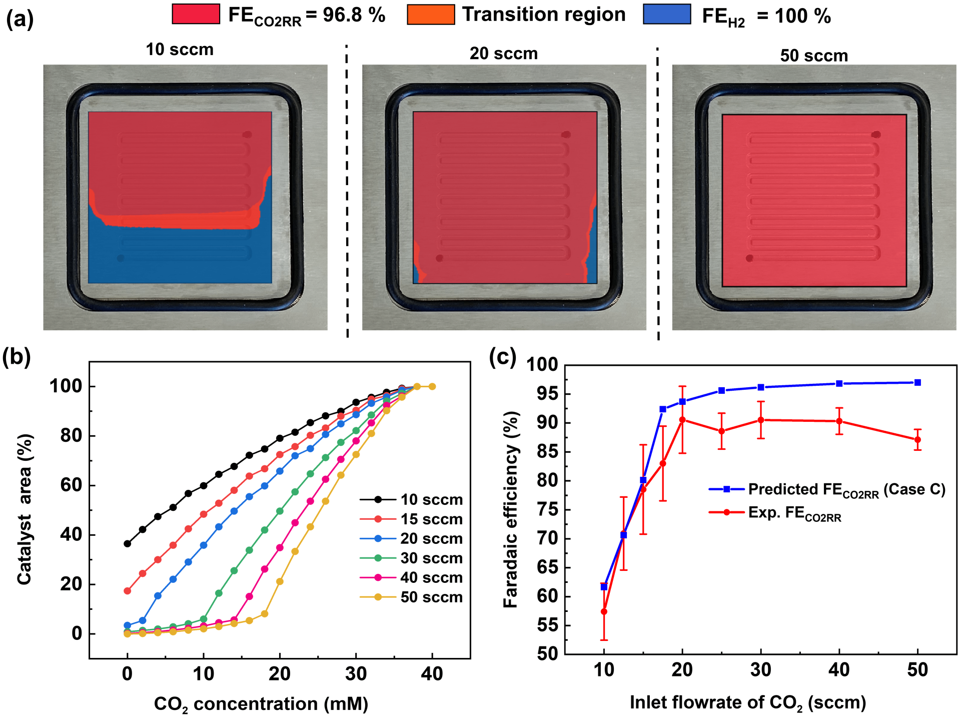

Figure 3.4 : (a) CO_2 concentration map at the catalyst surface determined from the numerical simulations showing the spatial CO_2 distribution at various inlet flowrates, (b) A cumulative distribution plot of CO_2 concentration at the catalyst surface for different inlet CO_2 flow rates studied using a modified current density approach and (c) Comparison of predicted faradaic efficiency of CO_2RR with experimentally determined faradaic efficiency ($FE_{CO} + FE_{HCOO^-}$).

The device-averaged FE can be calculated by using the distribution function in Figure 3.4b for a variety of different flow rates, and combining this with the criteria presented in Equations 1 and 2. The resulting predicted FE of CO_2RR and H_2 for all the inlet flowrates studied are then shown in Figure 3.4c, with the experimentally-measured values overlaid. It can be seen clearly that the predicted FE is in close agreement with the experimental FE of CO_2RR, showing the promise for using predicted CO_2 distribution within the reactor to predict spatial and average device selectivity. The consistent overprediction can be attributed to the experimental FE's being less than 100%, most likely due to the inability to capture all produced formate in MEA cell. Importantly both the trend in selectivity within the higher CO_2 utilization region (10 to 20 sccm), as well as in the lower utilization range (20-50 sccm), follow the experimental data set well. Such a model forms the foundation for comparing GDE's with different permeability, flow fields with different geometries, and the trade-offs with selectivity and utilization under different current densities.

The model can also be used to draw new observations from the experimental data set. For example, the incremental change in CO_2RR from 20-50 sccm is shown to be due to a CO_2 deficiency on the outer edges of the domain where the larger gas-diffusion layer (6.25 cm^2) loses access to CO_2 from the 5 cm^2 serpentine channel area (see 20 sccm plot in Figure 3.4a). Such an area then only produced H_2, which slightly lowers the "black box" measured FE via gas chromatography. We are then able to predict the location on the catalyst surface where CO_2 limitation occurs, which can help in understanding and designing flow channel designs at the cathode.

Finally, we emphasize here that at an applied current density of 200 mA/cm^2, there is an increase in the amount of CO_2 reacting with OH^- ions with an increase in the reactant flow rate, which is identified in the increase in the j_{loss} value (Table S2). This increase is quite reasonable since the local OH^- ions generated at 200 mA/cm^2 is a constant (1.3 x10-5 mol/s) and an increase in the local CO_2 concentration due to increased inlet flowrate shifts the reaction to the right producing more HCO_3^- and CO_3^{2-} ions. Moreover, this reduction in local [OH^-] with increasing inlet flow rates would also reduce the local pH altering the reaction environment around the catalyst surface. A further increase in inlet flow rate (60-100 sccm) would result in the consumption of all the OH^- ions generated at the catalyst producing more HCO_3^{2-} and CO_3^{2-} ions with a subsequent alteration of the local reaction environment. Operating at such high reactant flow rates would however reduce the CO_2 utilization to less than 10% and also increase the pressure drop between the inlet and outlet (serpentine channel) resulting in an increased pumping power[30]. Hence, optimizing the reactant flow rate to overcome CO_2 mass transport losses as well as ensuring a high CO_2 utilization and a low pressure drop is a challenge. Therefore, we restricted our focus of this study to flow rates of up to 50 sccm.

3.2.4. FORMATE PRODUCTION FROM SILVER GDE

While much of the work here focussed on the availability of CO_2 and the subsequent CO_2RR selectivity as a result of this, the experimental data set noted interesting and opposing trends in CO and formate selectivity under a variety of flow rate conditions (Figure 3.2a). In particular, while overall CO_2RR versus HER trended downward as flow rates decreased as could be expected (Figure 3.5a), the selectivity of CO to formate also followed a similar linear trend, both within the CO_2-limited and non-limited flow rate regions (Figure 3.5b). Here, we briefly contextualize these results and offer possible explanations given previous literature reports and our spatial model constructed here. It is worth noting that to measure formate we performed HPLC measurements of the anolyte samples post electrolysis for our Ag GDE system, meaning that only formed formate which crossed the anion exchange membrane could be measured, likely explaining some missing FE in our data set. We will provide speculation in spite of this.

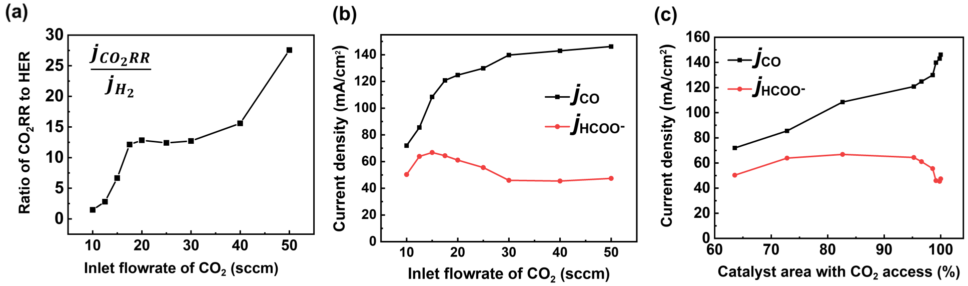

Figure 3.5 : (a) Ratio of partial current densities of CO_2 RR (CO+HCOO-) and H_2. Partial current densities of CO and formate with (b) varying inlet CO_2 flowrates and (c) Cumulative catalyst area with CO_2 access.

The trend in CO to formate within the two flow rate regions have two possible explanations from literature: (i) the reaction pathway to formate exists through surface-adsorbed protons and competition with HER, (ii) formate selectivity supplants some CO selectivity under higher alkalinity conditions. The first point has been reported previously by Bohra et.al[31] using DFT calculations which showed that *OCHO towards formate forms through a bound *H, whereas CO formation proceeds first through direct CO_2 adsorption. Thus, formate formation requires the Volmer step from HER formation in order to be formed. It would then be expected to see a lower CO/formate ratio when *H is more common, which would be the case in decreased and depleted CO_2 conditions like those observed from 10 to 20 sccm. Regarding (ii), previous studies on GDE flow cells have shown increased formate/CO ratios under extremely alkaline conditions (11 M KOH in Seifitokaldani et.al[32]) and decreased formate/CO ratios under higher CO_2 pressures (Gabardo et al.[33]). Both reports indicate that the pH of the reaction environment will influence the ratio of CO to formate produced. Within our system, this hypothesis could help to explain the decreasing trend in formate production as the inlet flow rate ranges from 20-50 sccm. At higher flow rates excess CO_2 is available to negate the formed OH^- from the fixed current density reaction (see $\dot{V}_{CO2toOH-}$ blocks in Figure 3.2c). It is then likely that the reaction environment surrounding the catalyst layer leans to lower alkalinities at 50 sccm versus that of 20 sccm, even though ample CO_2 is available in both cases. The experimental decrease in j_{HCOO-} is also seen when the model and experiments are combined (Figure 3.5c), where formate current density drops when the full catalyst area has access to CO_2.

OPERATING FEED RATE FOR LARGER CELLS AT HIGH CURRENT DENSITIES

While the serpentine flow channel employed in this study is 5cm^2, the diffusion of CO_2 from the gas channel to the catalyst layer remains similar for large area/flow channel as well. However, at large areas, the under rib convection increases CO_2 mass transport due to the large pressure drop which might change depending on the operating reactant flow rate. In addition, as the reactant flow rate increases, the fraction of CO_2 lost to OH^- ions will reach a maximum at a fixed current density. Hence, the results obtained here can be used to formulate design rules for larger cells and higher current densities.

To account for this, we tried to formulate the operating CO_2 feed which best balances CO_2 utilization and device selectivity for a given electrode area and current density. From Figure 3.4(a), it is clear that operating at a CO_2 flow rate of 20 sccm best balances CO_2 utilization (40%) and device selectivity (93%). Normalizing this value with the geometric surface area of the GDE (6.25 cm^2) and partial current density of CO (125 mA/cm^2), we predict that the operating reactant feed for industrial operation should be 0.0256 cm^3/min mA. We compared this value with a study from Endrodi et.al[13] where a similar study using Ag GDE in a zero gap CO_2 electrolyzer at 1 A/cm^2 was performed. In their study, a large geometric surface area of 100 cm^2 was employed and a feed rate of 12.5 cm^{3}min^{-1}cm^{-2} was used to obtain the same CO_2 utilization of 40%. Normalizing this feed rate to their CO partial current density (630 mA/cm^2), the operating feed comes to 0.0198 cm^{3}min^{-1} mA^{-1}) which agrees closely with our predicted value. Hence, we predict that operating at a feed flow rate of about 0.02 cm^{3}min^{-1} mA^{-1} would best balance CO_2 utilization and product selectivity, although the catalyst preparation methods and other operating parameters (eg. temperature, GDE thickness and porosity) might slightly alter this value which can also be predicted by using the empirical model reported in this study.

3.3. CONCLUSION

The balance between CO_2 utilization and selectivity with electrochemical systems will be ever more important as CO_2 electrolyzers are scaled to larger areas and considered within larger chemical processes due to implications they have on reliability, separation processes and system costs. The trade- offs in these metrics are currently measured and reported for an entire reactor, while being driven by spatial variation in concentrations across an entire electrochemical reactor. At present, the experimental ability for direct localized measurement of CO_2 electrolysis products has not been demonstrated however. The work presented here aims to predict this trade-off by paring bulk product measurement with a transport model to provide a measure of spatial resolution to our electrochemical cell. We believe that our approach can provide a starting point for a more extensive modelling study to enhance the understanding of the local reaction environment around the catalyst surface in a membrane electrode assembly configuration, employing anion exchange membranes.

3.4. SUPPLEMENTARY INFORMATION

3.4.1. EXPERIMENTAL

All experiments were performed in a 5 cm^2 area membrane electrode assembly (Dioxide materials) having a serpentine flow channel on both the anode and cathode endplates. Sigracet 38 BC gas diffusion layers (GDL) of 6.25 cm^2 area (2.5cm x 2.5cm) was used as the porous transport layer. Ag catalyst layer was deposited on top of microporous layer of GDL by direct current magnetron sputtering to obtain a thickness of 100 nm. Nickel foam (3cm x 3cm) was used as the anode. Ag GDE and Ni foam were combined with an oversized 16 cm^2 (4cm x 4cm) Sustainion anion exchange membrane (X37-50 Grade RT) to assemble the MEA (Figure 3.6). An exchange MEA configuration using 1M KOH as the anolyte and humidified CO_2 as reactant were fed at the cathode side of the MEA cell.

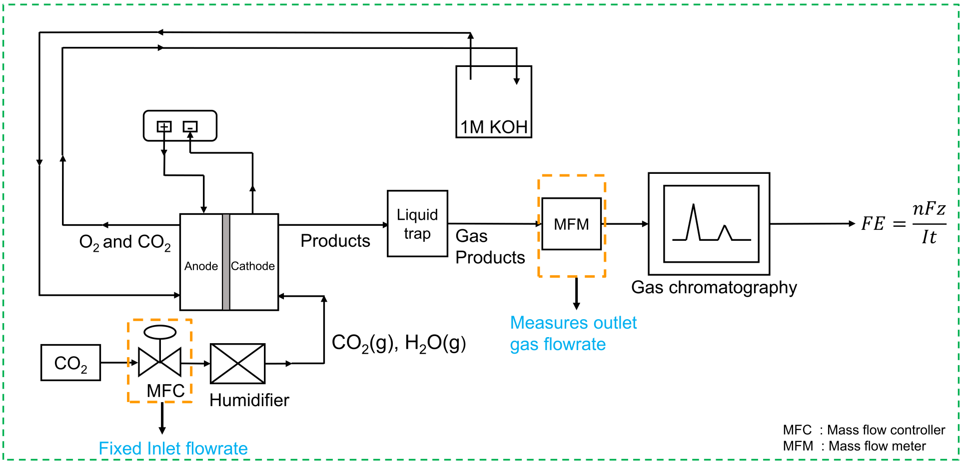

Figure 3.6 : Simplified process flow diagram of the experimental setup used for CO_2 electroreduction in an exchange MEA cell configuration.

CO_2 was humidified by bubbling dry CO_2 into a water bath at room temperature and the relative humidity was measured using a humidity sensor. The MEA was prepared by physical compression of the electrodes and endplates using a torque wrench which were tightened to 4 Nm. This value was chosen to enhance the contact between the GDE and membrane while simultaneously ensuring that no physical damage occurred to the carbon GDE. A series of constant current electrolysis experiments with different reactant flow rates were performed and the gaseous products from the cell were analysed using an online gas chromatography connected to the outlet of the cell equipped with two thermal conductivity detectors and a flame ionization detector. All experiments were performed for 1 hour at a current density of 200 mA/cm^2. Aliquots were collected every 5 min during the reaction resulting in a total of 12 injections in 1 hour. The concentration of gaseous products (CO and H_2) were obtained from GC and the average of 12 injections was used to calculate their faradaic efficiencies. The anolyte samples were collected after each experiments to quantify liquid products produced using HPLC measurements (Agilent Technologies).

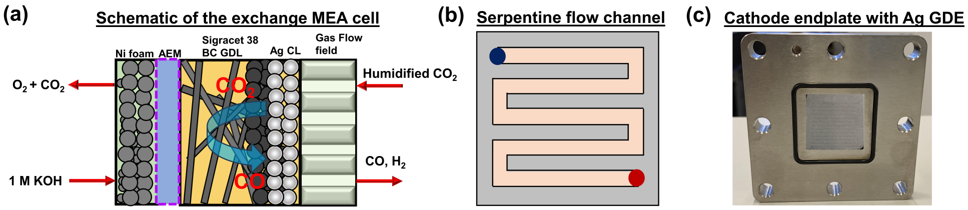

Figure 3.7 : (a) Schematic of the exchange membrane electrode assembly configuration used in the experiments. (b) Serpentine flow channel with alternating turns at the endplate and (c) Dioxide materials cathode endplate with Ag GDE used in the study.

The flow rate at the outlet of the reactor was measured using a mass flow meter (Bronkhorst) in order to estimate the faradaic efficiency of products accurately. A LABVIEW program was built and connected to the mass flow meter for continuous monitoring of the outlet flowrate. The experimental setup and the entire system design used is shown in Figure 3.6. The outlet flow rate of the gas mixture ($CO+H_2$ +residual CO_2) from the reactor was measured $\dot{V}_{outlet}$ using the mass flow meter and the mole fractions of CO and H_2 were estimated from the GC injections. All the calculated values are reported in Table 3.2.

FARADAIC EFFICIENCY CALCULATION

To estimate the Faradaic efficiency of gaseous products, the mole fractions of CO and H_2 were estimated from GC injections. The volume fraction of gas products from GC is equal to the mole fraction for ideal gases. The mole fraction of water vapour exiting the reactor was measured using a humidity sensor and found to be 78% (x_{H_2O} = 0.023). Since the sum of mole fractions is equal to 1, the mole fraction of CO_2 exiting was calculated as,

$$x_{CO_2,out} = 1 - (x_{CO} + x_{H_2O} + x_{H_2}) \tag{3.5}$$

After calculating the mole fractions of all gaseous products, the volumetric flow rate at the outlet of the reactor were measured with the MFM and used to calculate the moles of each product.

$$\eta_{CO} = \frac{P \times x_{CO} \times \dot{V}_{outlet}}{RT} \tag{3.6}$$

$$\eta_{H_2} = \frac{P \times x_{H_2} \times \dot{V}_{outlet}}{RT} \tag{3.7}$$

$$FE_{CO} = \frac{\eta_{CO} \times n^{e} \times F}{I} \times 100\% \tag{3.8}$$

Here: n_{CO} – moles/s of CO produced, n^{e}- number of electrons involved in CO_2RR (2 for CO), F- 96485 C/mol and I - applied current (in Amperes).

Carbon balance at the cathode side

The following equations were then used to calculate the CO_2 consumption with OH^- ions by performing carbon balance at the cathode side.

$$\dot{V}_{CO_2\,to\,CO} = x_{\mathrm{CO}} \times \dot{V}_{outlet} \tag{3.9}$$

$$\dot{V}_{H_2} = x_{\mathrm{H_2}} \times \dot{V}_{outlet} \tag{3.10}$$

$$\dot{V}_{residual\,CO_2} = \dot{V}_{outlet} - (\dot{V}_{CO_2\,to\,CO} + \dot{V}_{H_2}) \tag{3.11}$$

$$\dot{V}_{CO_2\ \mathrm{to\ HCOO^-}} = ((1 - x_{\mathrm{CO}} - x_{\mathrm{H_2}}) \times \frac{jA}{n^{\mathrm{e}}F} mol s^{-1} \times 22.4 L mol^{-1} \times 60 s \times 1000)\ ml min^{-1} \tag{3.12}$$

$$\dot{V}_{\mathrm{OH^-}} = \dot{V}_{\mathrm{inlet}} - (\dot{V}_{\mathrm{residual\ CO_2}} + \dot{V}_{\mathrm{CO_2\ to\ HCOO^-}}) \tag{3.13}$$

$$CO_2\,utilization = \frac{(\dot{V}_{\mathrm{CO_2\ to\ CO}} + \dot{V}_{\mathrm{CO_2\ to\ HCOO^-}})}{\dot{V}_{\mathrm{inlet}}} \times 100\% \tag{3.14}$$

$$j_{\mathrm{loss}} = \frac{n^{\mathrm{e}} \times \dot{V}_{\mathrm{CO_2\ to\ OH^-}} \times F}{A} \tag{3.15}$$

Table S2 shows the carbon balance performed on the cathode side from which the fraction of CO_2 reacting with OH^- ions was calculated. Here, measuring the flowrate of gas products at the outlet of the reactor is an important factor in the estimation of FE of gas products and CO_2 losses. We observed that the sum of FE of CO and H_2 did not add upto 100 % which is possibly due to the formation of some liquid products. To determine this, we collected the anolyte (1M KOH) samples post electrolysis and conducted high performance liquid chromatography (HPLC) analysis. Formate ($HCOO^-$) was the only product detected showing that formate ions produced at the cathode migrates to the anolyte through the AEM. The sum of FE of CO, H_2 and formate reached 96-97.5% for most of the studied inlet flow rates and we suspect that the remaining formate ions possibly oxidized to CO_2 at the anode as reported previously. After this confirmation, we calculated the FE of formate produced as 100 -(FE_{CO} + $FE_{\mathrm{H_2}}$) in order to make a carbon balance at the cathode side with the assumption that no non-faradaic reactions take place. The amount of CO_2 lost to OH^- ions was then calculated for all the studied inlet flowrates.

Table 3.1: CO_2 consumption, utilization rate, modified inlet flow rates and j_{loss} used in the model at an applied current density of 200 mA/cm^2.

Inlet flowrate (sccm)	**$\dot{V}_{CO_2 \text{ to } CO}$ (ml/min)**	**$\dot{V}_{CO_2 \text{ to } HCOO^-}$ (ml/min)**	**$\dot{V}_{\text{residual } CO_2}$ (ml/min)**	**$\dot{V}_{OH^-}$ (ml/min)**	**CO_2 utilization (%)**	**Case B (ml/min)**	**Case C- j^{loss} (mA/cm^2)**
10	3.13	1.95	0.69	4.41	50.8	5.59	106.4
12.5	3.72	2.55	0.81	5.55	50.1	6.95	127.5
15	4.15	3.29	1.67	6.19	49.6	8.81	142.2
17.5	4.41	3.63	2.58	6.78	45.9	10.72	155.7
20	5.49	2.65	4.83	7.35	40.7	12.65	168.9
25	5.65	2.20	10.61	7.41	31.4	17.59	170.3
30	5.93	2.14	14.40	8.01	26.9	21.99	184.1
40	6.17	2.02	23.80	8.78	20.5	31.22	201.7
50	6.18	2.24	33.25	9.31	16.8	40.69	214.1

($\dot{V}_{CO_2 \text{to CO}}$: consumed CO_2 flow rate which is electrochemically converted to gas product CO; $\dot{V}_{\text{residual } CO_2}$: unreacted CO_2 flowrate in the gas outlet; $\dot{V}_{OH^-}$: consumed CO_2 flowrate via the reaction with OH$^-$.)

MODIFIED CURRENT DENSITY USED IN THE MODEL (CASE C)

The modified current density used in the model for various inlet flowrates is shown in figure 3.8, taking into account total electrochemical and non-electrochemical consumption.

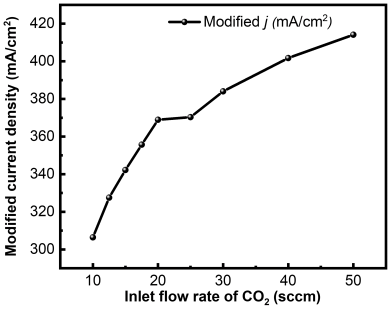

Figure 3.8 : Modified current density used in the model after taking into account of the fraction of CO_2 lost to hydroxide ions from carbon balance.

OUTLET GAS FLOWRATE AND FARADAIC EFFICIENCY MEASUREMENT

Figure 3.9 shows the gas outlet flowrate at the exit of the reactor during CO_2RR and the corresponding faradaic efficiencies of CO and H_2 during the measurement.

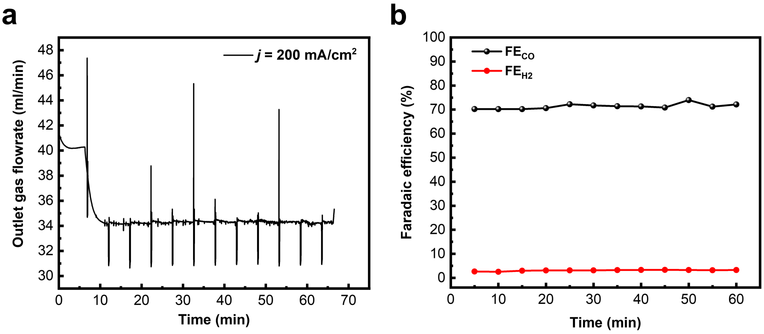

Figure 3.9 : (a) Measured outlet flowrate during electrolysis at 200 mA/cm^2 for an inlet flow rate of 50 sccm. The dip in the peaks occurring every 5 min are due to the periodic GC injections. (b) Faradaic efficiency of CO and H_2 measured from the GC injections.

VOLUMETRIC FLOWRATE OF HUMIDIFIED CO_2

The volumetric flowrate of humidified CO_2 entering the reactor varies slightly for each of the dry CO_2 flowrate due to bubbling of the gas into humidifer. To account for this, we measured the flowrate of humidified CO_2 reacting with OH^- ions since it depends on the inlet flowrate as shown in Equation 3.13.

Table 3.2: CO_2 consumption, utilization rate, modified inlet flow rates and j_{loss} used in the model at an applied current density of 200 mA/cm^2.

Inlet flowrate of dry CO_2 measured from MFC (sccm)	Measured flowrate of humidified CO_2 (sccm)
10	10.1
12.5	12.6
15	15.1
17.5	17.6
20	20.2
25	25.3
30	30.5
40	40.8
50	51.0

RELATIVE HUMIDITY MEASUREMENTS

The relative humidity (R.H) at the outlet of the reactor was measured during electrolysis and was found to remain constant throughout 1 hr of electrolysis. It did not vary for the various inlet flow rates. The measured R.H for an inlet flowrate of 50 sccm of CO_2 is shown in Figure 3.10. The R.H at outlet as shown here is 78% which corresponds to a mole fraction of 0.023 for H_2O and used in FE calculations.

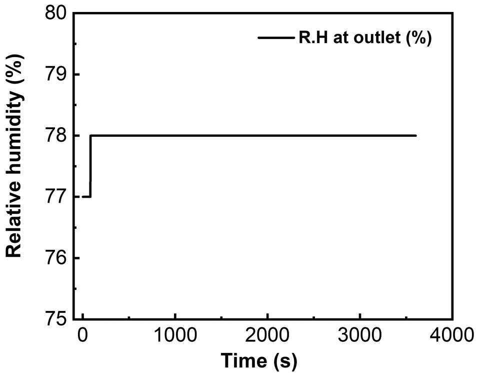

Figure 3.10 : Measured relative humidity at the outlet during CO_2RR at 200 mA/cm^2 and an inlet flowrate of 50 sccm.

Table 3.3: Analysis of liquid product (formate) from the anolyte using HPLC and comparison with the predicted FE.

Inlet flowrate (sccm)	**HCOO$^-$ detected from HPLC (ml/min)**	**FE of HCOO$^-$(%)**	**Predicted FE of HCOO$^-$ (100- FE_{CO}- FE_{H_2})**	**Missing FE (%)**
10	3.13	1.95	0.69	4.41
12.5	3.72	2.55	0.81	5.55
15	4.15	3.29	1.67	6.19
17.5	4.41	3.63	2.58	6.78
20	5.49	2.65	4.83	7.35
25	5.65	2.20	10.61	7.41
30	5.93	2.14	14.40	8.01
40	6.17	2.02	23.80	8.78
50	6.18	2.24	33.25	9.31

3.5. MODEL DESCRIPTION

A 3D geometry of the cathode compartment (5cm^2 area) comprising of the serpentine flow channel with a series of alternating 1800 turns and 12 ribs with same length (2.25 cm), width (1 mm) and depth (1 mm) was modeled in COMSOL Multiphysics. A carbon GDL of dimensions (2.5 cm x 2.5 cm x 0.325 cm) was placed in contact with the flow channel (Figure 3.11b). The numerical simulations were performed using a MUMPS general solver with a relative tolerance of 0.001 to calculate the CO_2 concentration gradient in the gas channels and catalyst surface. For Case A and Case B, a current density of 200 mA/cm^2 was applied at the catalyst surface. For Case C, the modified current density for each of the inlet flow rate was used to estimate the concentration gradient.

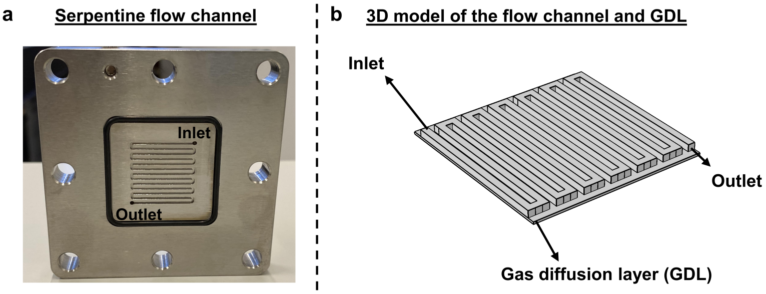

Figure 3.11 : (a) 5 cm ^{2} cathode flow plate used in the experiments comprising the serpentine flow channel and (b) 3D model of the cathode compartment of MEA modelled in COMSOL Multiphysics.

Electrochemical reduction of CO_2 to CO was modelled and the competing hydrogen evolution reaction was not taken into account. The electrochemical reduction reaction occurring at the cathode is a 2e$^-$ reduction reaction:

$$CO_2RR : CO_2 + H_2O + 2e^- \rightarrow CO + 2OH^- \tag{3.16}$$

All parameters used in the model were taken from the experimental setup. The following assumptions were made in the model:

- The system operates at steady-state conditions.
- Carbon GDL is assumed to be isotropic with constant porosity and permeability since the in-plane diffusion is than the through plane diffusion.
- Both diffusion and convection from the channel to the catalyst surface are taken into account.

- A uniform current distribution is assumed on the catalyst surface.

- Isothermal at 298 K with no thermal diffusion gradients.

3.5.1. BRINKMANN EQUATION AND MIXTURE DIFFUSION MODEL

The fluid flow in the serpentine channels was modelled using the Brinkmann equations which is a modified form of the Navier stokes equation for porous media flows. A no-slip boundary condition was imposed on the channel walls. A slip condition was used at the channel-GDL interface since the normal component of velocity is zero at this interface. Single phase compressible flow was assumed. An inlet boundary condition was given by a normal inflow velocity defined by the flowrate ($\dot{V}_{\text{in}}$) over inlet cross sectional area of the channel (Dirichlet boundary condition). $\dot{V}_{\text{in}}$ varied from 10 to 50 sccm which was used in the experiments. A zero pressure boundary condition was imposed at the outlet (Neumann boundary condition) with the suppression of backflow.

The Brinkman equation solves for the velocity and pressure distribution in the GDL. It was coupled with the mixture diffusion model taking into account of the diffusion and convection through the GDL. All parameters used in the model can be found in Table S5. For the meshing, a free tetrahedral mesh with a fine mesh size was used for the channels and a swept mesh was used for the GDL (98023 domain elements, 24196 domain elements and 2894 edge elements) resulting in a run time for 45 minutes for every simulation. The velocity and pressure field in the gas channels were solved using:

$$\rho(\mathbf{u}\bullet\nabla)\mathbf{u} = \nabla\bullet[-p\mathbf{I} + \mu(\nabla\mathbf{u} + (\nabla\mathbf{u})^T) - \frac{2}{3}\mu(\nabla\bullet\mathbf{u})\mathbf{I}] + F \tag{3.17}$$

$$\nabla\bullet(p\mathbf{u}) = 0 \tag{3.18}$$

$$\frac{1}{\epsilon_p}\rho\,(\mathbf{u}\bullet\nabla)\,\mathbf{u}\frac{1}{\epsilon_p} = \nabla\bullet\left[-p\mathbf{I} + \mu\frac{1}{\epsilon_p}((\nabla\mathbf{u}) + (\nabla\mathbf{u})^{\mathbf{T}}) + -\frac{2}{3}\mu\frac{1}{\epsilon_p}\,(\nabla\bullet\mathbf{u})\,\mathbf{I}\right] - \left(\mu\kappa^{-1} + \frac{Q_m}{\epsilon_p^2}\right)\mathbf{u} + F \tag{3.19}$$

$$\nabla\bullet(p\mathbf{u}) = 0 \tag{3.20}$$

In these equations, ρ is the density of the fluid, μ is the dynamic viscosity of the fluid, p is the pressure, **u** is the gas velocity, F is the force term, κ is the gas permeability of the GDL, ϵ_p is the porosity of the GDL and Q_{m} is the mass source.

To solve for the species transport in the system, a mixture diffusion model was used. The relative humidity in the inlet stream was ignored since the humidity measured experimentally remained constant at the inlet. So, we accounted for only 2 species which are the reactant CO_2 and the gas product CO. However, the CO_2 lost to OH^- ions was indirectly accounted for in the model (Case C) by using modified current densities based on total CO_2 consumption. The molar flux of species were calculated using the following equations:

$$\nabla \bullet\ j_i + \rho\,(\mathbf{u} \bullet \nabla)\,\omega_i = R_i \tag{3.21}$$

$$N_j = j_i + \rho \mathbf{u} \omega_\mathbf{i} \tag{3.22}$$

$$\mathbf{j}_i = -(\rho\ D_i^m \nabla \omega_i + \rho \omega_i D_i^m \frac{\nabla M_n}{M_n}) \tag{3.23}$$

$$R_i = \frac{v_i i_v}{nF} + j_{\text{loss}} \tag{3.24}$$

Here:
N is the total flux vector of species i, R_i is the reaction rate for species i, $\mathbf{u}$ is the fluid velocity, j_i is the relative mass flux due to molecular diffusion of species i, ω_i is the mass fraction of species i, i_v is the volumetric current density, j_loss is the modified current density based on moles of CO_2 consumed to hydroxide ions and F is Faraday's constant. Here, equation 3.22 represents the convection-diffusion equation with the first term representing diffusion and second term representing convection, the magnitude of which depends on the inlet velocity 'u'.

MESH INDEPENDENCE STUDY

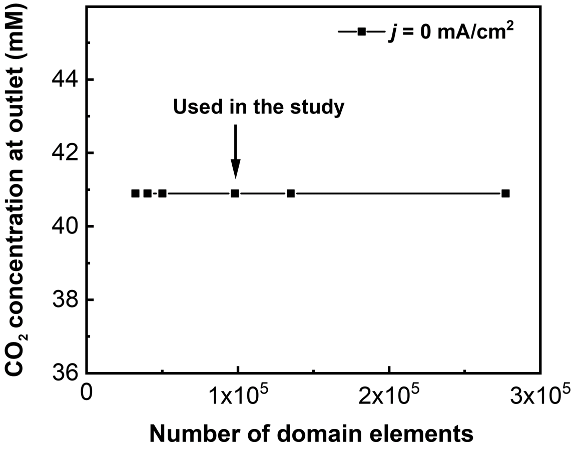

Figure 3.12 : A mesh independence study performed with different mesh element sizes at an inlet flowrate of 50 sccm and a current density of 200 mA/cm^2. The average CO_2 concentration at the catalyst surface was calculated and did not vary within the shown number of domain elements. A mesh independence study was performed to ensure that the right mesh size was chosen. An element size of 0.5 mm was chosen for the free tetrahedral

mesh that generated a total of 98023 domain elements. Figure 3.12 shows the mesh independence study performed to estimate the average CO_2 concentration at the catalyst surface for an inlet flowrate of 50 sccm and 200 mA/cm^2.

3.5.2. SIMULATION RESULTS OF CO_2 CONCENTRATION

The simulation results of CO_2 concentration in the gas channels and at the catalyst surface are shown in Figure 3.13 for an inlet flow rate of 10 sccm. Here, the CO_2 losses to OH^- ions are ignored (Case A).

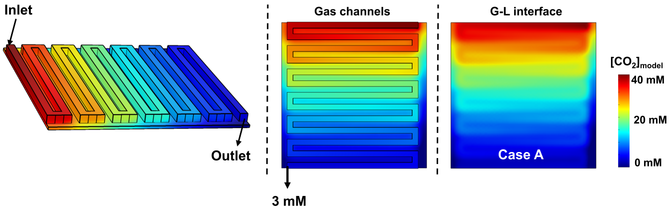

Figure 3.13 : CO_2 concentration at the catalyst surface for an inlet flow rate of 10 sccm and current density of 200 mA/cm^2 without accounting for the fraction of CO_2 reacting with hydroxide ions.

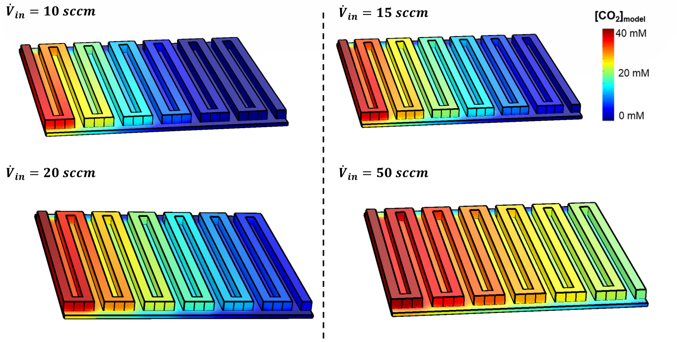

Figure 3.14 : CO_2 concentration at the cathode for different inlet flow rates using a modified current density approach (Case C). Here, the CO_2 losses to OH^- occurring homogeneously throughout the catalyst surface are considered.

AVERAGE CO_2 CONCENTRATION

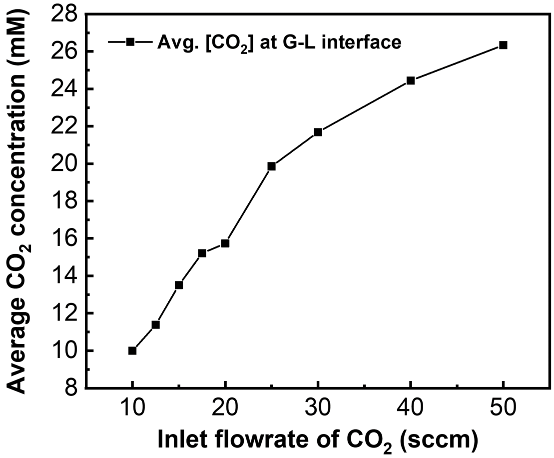

Figure 3.15 : The average CO_2 concentration at the G-L interface for different inlet flow rates calculated from the model (Case C).

CUMULATIVE CATALYST AREA WITH $[CO_2]$=0

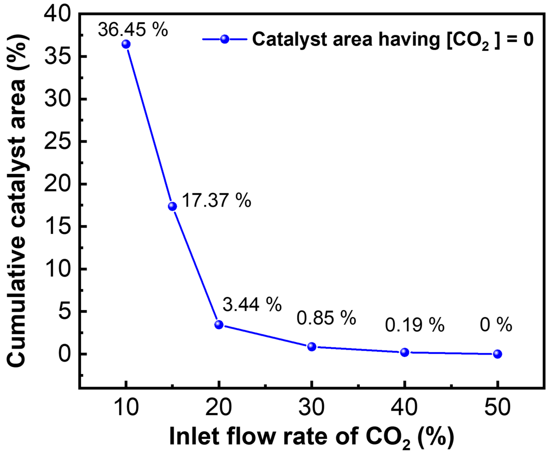

Figure 3.16 : Percentage of catalyst surface area with no CO_2 access for the different inlet flowrates calculated using modified current density approach (Case C)

CUMULATIVE DISTRIBUTION PLOTS OF CO_2 CONCENTRATION

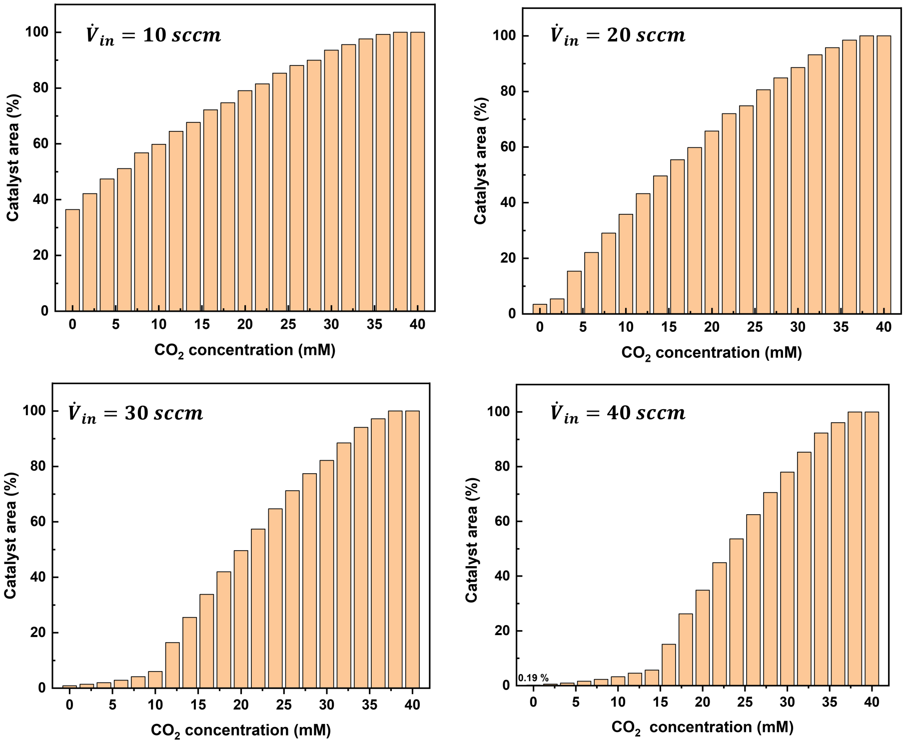

Figure 3.17 : Cumulative distribution plots of CO_2 concentration for various inlet flowrates using modified current density approach.

CELL VOLTAGE AT 200 MA/CM^2

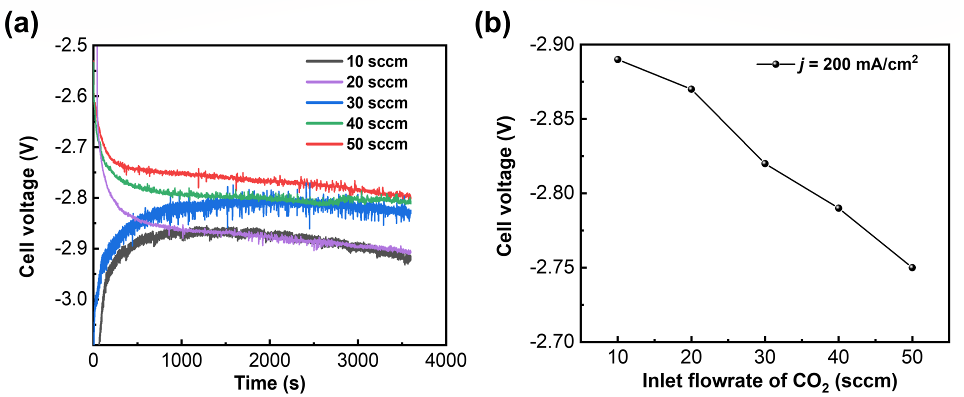

Figure 3.18 : (a) Variation of cell voltage of the MEA cell with time during CO_2RR at various inlet flowrates. (b) Cell voltage decreases with an increase in inlet CO_2 flowrates due to increased CO_2RR and lower HER.

CHARACTERIZATION OF AG CATALYST LAYER

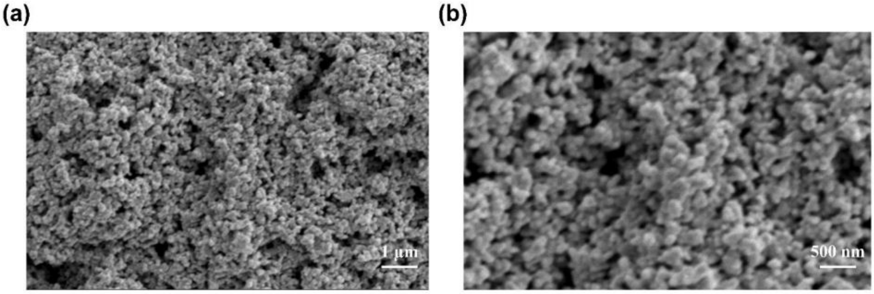

Figure 3.19 : SEM images of Ag catalyst sputtered on the microporous layer of Sigracet 38 BC gas diffusion layer.

X-ray diffraction analysis

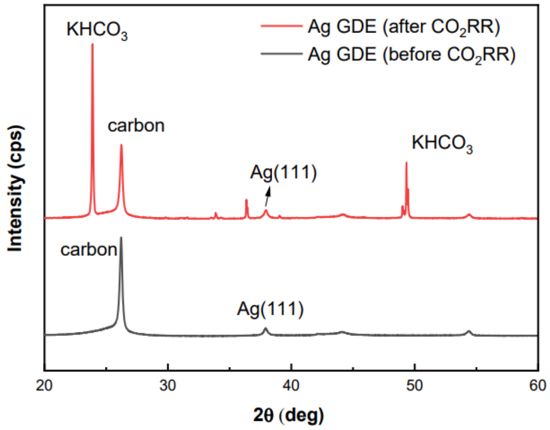

Figure 3.20 : XRD pattern of Ag GDE before and after CO_2 electrolysis showing the presence of Ag(111) facet. Potassium bicarbonate peaks are visible due to precipitation of the salt at the cathode side.

X-ray spectroscopy results

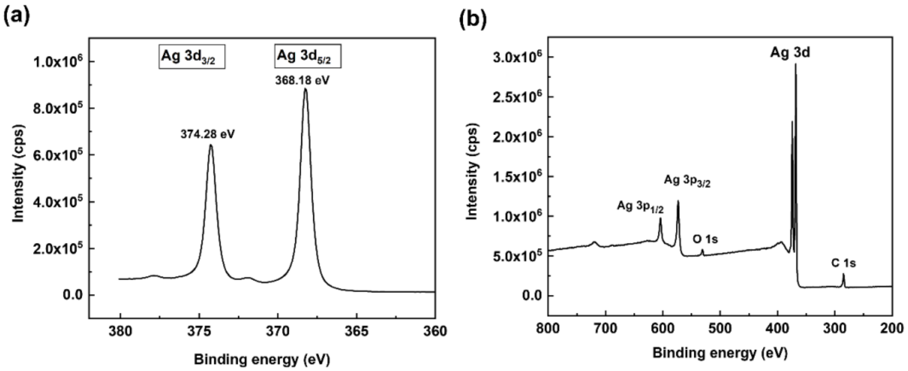

Figure 3.21 : XPS analysis of Ag catalyst coated on microporous layer of Sigracet 38 BC gas diffusion layer

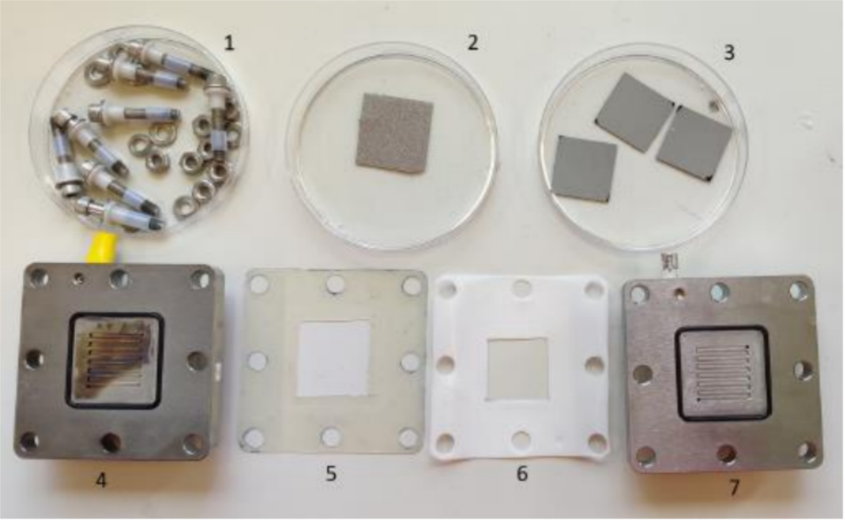

Figure 3.22 : Components used in the MEA cell. 1. Nuts and bolts, 2. Ni foam, 3. GDE with Ag catalyst layer, 4. Titanium anode endplate, 5. Silicone gasket for anode, 6. PTFE gasket for cathode, 7. Stainless steel cathode endplate.

Table 3.4: Parameters used in the 3D mass transport and fluid flow model

Parameter	**Symbol**	**Value**	**Units**
Temperature	T	298	K
Reference Pressure	P	1	atm
Diffusivity of CO into CO_2	$D_{CO_2\text{-}CO}$	1.52×10^{-5}	1.67
Porosity of GDL	ϵ	0.8	-
Permeability of GDL	κ	1 x10^{-12}	m^{-1}
Inlet flowrate	Q	10 to 50	SCCM
Applied Current density	i_{loc}	-2000	A/m^2

REFERENCES

[1] Y. i. Hori. “Electrochemical CO2 reduction on metal electrodes”. In: *Modern aspects of electrochemistry* (2008), pp. 89–189.

[2] W. Tang, A. A. Peterson, A. S. Varela, Z. P. Jovanov, L. Bech, W. J. Durand, S. Dahl, J. K. Nørskov, and I. Chorkendorff. “The importance of surface morphology in controlling the selectivity of polycrystalline copper for CO2 electroreduction”. In: *Physical Chemistry Chemical Physics* 14.1 (2012), pp. 76–81.

[3] Y. Hori, I. Takahashi, O. Koga, and N. Hoshi. “Selective formation of C2 compounds from electrochemical reduction of CO2 at a series of copper single crystal electrodes”. In: *The Journal of Physical Chemistry B* 106.1 (2002), pp. 15–17.

[4] D. Gao, R. M. Arán-Ais, H. S. Jeon, and B. Roldan Cuenya. “Rational catalyst and electrolyte design for CO2 electroreduction towards multicarbon products”. In: *Nature Catalysis* 2.3 (2019), pp. 198–210.

[5] R. I. Masel, Z. Liu, H. Yang, J. J. Kaczur, D. Carrillo, S. Ren, D. Salvatore, and C. P. Berlinguette. “An industrial perspective on catalysts for low-temperature CO2 electrolysis”. In: *Nature nanotechnology* 16.2 (2021), pp. 118–128.

[6] O. G. Sánchez, Y. Y. Birdja, M. Bulut, J. Vaes, T. Breugelmans, and D. Pant. “Recent advances in industrial CO2 electroreduction”. In: *Current Opinion in Green and Sustainable Chemistry* 16 (2019), pp. 47–56.

[7] T. Burdyny and W. A. Smith. “CO 2 reduction on gas-diffusion electrodes and why catalytic performance must be assessed at commercially-relevant conditions”. In: *Energy & Environmental Science* 12.5 (2019), pp. 1442–1453.

[8] M. G. Kibria, J. P. Edwards, C. M. Gabardo, C.-T. Dinh, A. Seifitokaldani, D. Sinton, and E. H. Sargent. “Electrochemical CO2 reduction into chemical feedstocks: from mechanistic electrocatalysis models to system design”. In: *Advanced Materials* 31.31 (2019), p. 1807166.

[9] G. O. Larrazábal, A. J. Martín, and J. Pérez-Ramírez. “Building blocks for high performance in electrocatalytic CO2 reduction: materials, optimization strategies, and device engineering”. In: *The journal of physical chemistry letters* 8.16 (2017), pp. 3933–3944.

[10] S. Ma, P. J. Kenis, *et al.* “Electrochemical conversion of CO2 to useful chemicals: current status, remaining challenges, and future opportunities”. In: *Current Opinion in Chemical Engineering* 2.2 (2013), pp. 191–199.

[11] D. Higgins, C. Hahn, C. Xiang, T. F. Jaramillo, and A. Z. Weber. “Gas-diffusion electrodes for carbon dioxide reduction: a new paradigm”. In: *ACS Energy Letters* 4.1 (2018), pp. 317–324.

[12] D. T. Whipple, E. C. Finke, and P. J. Kenis. “Microfluidic reactor for the electrochemical reduction of carbon dioxide: the effect of pH”. In: *Electrochemical and Solid-State Letters* 13.9 (2010), B109.

[13] B. Endrődi, E. Kecsenovity, A. Samu, T. Halmágyi, S. Rojas-Carbonell, L. Wang, Y. Yan, and C. Janáky. “High carbonate ion conductance of a robust PiperION membrane allows industrial current density and conversion in a zero-gap carbon dioxide electrolyzer cell”. In: *Energy & Environmental Science* 13.11 (2020), pp. 4098–4105.

[14] F. P. García de Arquer, C.-T. Dinh, A. Ozden, J. Wicks, C. McCallum, A. R. Kirmani, D.-H. Nam, C. Gabardo, A. Seifitokaldani, X. Wang, *et al.* “CO2 electrolysis to multicarbon products at activities greater than 1 A cm- 2”. In: *Science* 367.6478 (2020), pp. 661–666.

[15] E. Jeng and F. Jiao. “Investigation of CO 2 single-pass conversion in a flow electrolyzer”. In: *Reaction Chemistry & Engineering* 5.9 (2020), pp. 1768–1775.

[16] M. Ma, E. L. Clark, K. T. Therkildsen, S. Dalsgaard, I. Chorkendorff, and B. Seger. “Insights into the carbon balance for CO 2 electroreduction on Cu using gas diffusion electrode reactor designs”. In: *Energy & Environmental Science* 13.3 (2020), pp. 977–985.

[17] C. M. Gabardo, C. P. O’Brien, J. P. Edwards, C. McCallum, Y. Xu, C.-T. Dinh, J. Li, E. H. Sargent, and D. Sinton. “Continuous carbon dioxide electroreduction to concentrated multi-carbon products using a membrane electrode assembly”. In: *Joule* 3.11 (2019), pp. 2777–2791.

[18] W. A. Smith, T. Burdyny, D. A. Vermaas, and H. Geerlings. “Pathways to industrial-scale fuel out of thin air from CO2 electrolysis”. In: *Joule* 3.8 (2019), pp. 1822–1834.

[19] G. Kyriacou and A. Anagnostopoulos. “Influence CO 2 partial pressure and the supporting electrolyte cation on the product distribution in CO 2 electroreduction”. In: *Journal of applied electrochemistry* 23 (1993), pp. 483–486.

[20] S. Dutta, S. Shimpalee, and J. Van Zee. “Three-dimensional numerical simulation of straight channel PEM fuel cells”. In: *Journal of Applied Electrochemistry* 30 (2000), pp. 135–146.

[21] P. Futerko and I.-M. Hsing. “Two-dimensional finite-element method study of the resistance of membranes in polymer electrolyte fuel cells”. In: *Electrochimica Acta* 45.11 (2000), pp. 1741–1751.

[22] Z. Wang, C. Wang, and K. Chen. “Two-phase flow and transport in the air cathode of proton exchange membrane fuel cells”. In: *Journal of power sources* 94.1 (2001), pp. 40–50.

[23] J. H. Nam, K.-J. Lee, S. Sohn, and C.-J. Kim. “Multi-pass serpentine flow-fields to enhance under-rib convection in polymer electrolyte membrane fuel cells: Design and geometrical characterization”. In: *Journal of Power Sources* 188.1 (2009), pp. 14–23.

[24] L. Rostami, P. M. G. Nejad, and A. Vatani. “A numerical investigation of serpentine flow channel with different bend sizes in polymer electrolyte membrane fuel cells”. In: *Energy* 97 (2016), pp. 400–410.

[25] C. J. Bondue, M. Graf, A. Goyal, and M. T. Koper. “Suppression of hydrogen evolution in acidic electrolytes by electrochemical CO2 reduction”. In: *Journal of the American Chemical Society* 143.1 (2020), pp. 279–285.

[26] H. Ooka, M. C. Figueiredo, and M. T. Koper. “Competition between hydrogen evolution and carbon dioxide reduction on copper electrodes in mildly acidic media”. In: *Langmuir* 33.37 (2017), pp. 9307–9313.

[27] D. Raciti, M. Mao, and C. Wang. “Mass transport modelling for the electroreduction of CO2 on Cu nanowires”. In: *Nanotechnology* 29.4 (2017), p. 044001.

[28] D. G. Wheeler, B. A. Mowbray, A. Reyes, F. Habibzadeh, J. He, and C. P. Berlinguette. “Quantification of water transport in a CO 2 electrolyzer”. In: *Energy & Environmental Science* 13.12 (2020), pp. 5126–5134.

[29] H. Song, J. T. Song, B. Kim, Y. C. Tan, and J. Oh. “Activation of C2H4 reaction pathways in electrochemical CO2 reduction under low CO2 partial pressure”. In: *Applied Catalysis B: Environmental* 272 (2020), p. 119049.

[30] D. Jeon, S. Greenway, S. Shimpalee, and J. Van Zee. “The effect of serpentine flow-field designs on PEM fuel cell performance”. In: *International journal of hydrogen energy* 33.3 (2008), pp. 1052–1066.

[31] D. Bohra, J. H. Chaudhry, T. Burdyny, E. A. Pidko, and W. A. Smith. “Modeling the electrical double layer to understand the reaction environment in a CO 2 electrocatalytic system”. In: *Energy & Environmental Science* 12.11 (2019), pp. 3380–3389.

[32] A. Seifitokaldani, C. M. Gabardo, T. Burdyny, C.-T. Dinh, J. P. Edwards, M. G. Kibria, O. S. Bushuyev, S. O. Kelley, D. Sinton, and E. H. Sargent. “Hydronium-induced switching between CO2 electroreduction pathways”. In: *Journal of the American Chemical Society* 140.11 (2018), pp. 3833–3837.

[33] C. M. Gabardo, A. Seifitokaldani, J. P. Edwards, C.-T. Dinh, T. Burdyny, M. G. Kibria, C. P. O’Brien, E. H. Sargent, and D. Sinton. “Combined high alkalinity and pressurization enable efficient CO 2 electroreduction to CO”. In: *Energy & Environmental Science* 11.9 (2018), pp. 2531–2539.

4

GEOMETRIC CATALYST UTILIZATION IN ZERO-GAP CO_2 ELECTROLYZERS

Research is the process of going up alleys to see if they are blind.

\- Marson Bates

Electrochemical CO_2 reduction reaction (CO_2RR) on silver catalysts has been demonstrated under elevated current density, longer reaction times, and intermittent operation. Maintaining performance requires that CO_2 can access the entire geometric catalyst area, thus maximizing catalyst utilization. Here we probe the time-dependent factors impacting geometric catalyst utilization for CO_2RR in a zero-gap membrane electrode assembly. We use three flow fields (serpentine, parallel, and interdigitated) as tools to disambiguate cell behavior. Cathode pressure drop is found to play the most critical role in maintaining catalyst utilization at all time scales by encouraging in-plane CO_2 transport throughout the gas-diffusion layer (GDL) and around salt and water blockages. The serpentine flow channel with the highest pressure drop is then the most failure-resistant, achieving a CO partial current density of 205 mA/cm^2 at 2.76 V. These findings are confirmed through selectivity measurements over time, double-layer capacitance measurements to estimate GDL flooding, and transport modeling of the spatial CO_2 concentration.

This chapter has been published as "Geometric Catalyst Utilization in Zero-gap CO_2 electrolyzers" by Siddhartha Subramanian, Kailun Yang, Mengran Li, Mark Sassenburg, Maryam Abdinejad, Erdem Irtem, Joost Middelkoop, and Thomas Burdyny. *ACS Energy Letters 8, no. 1 (2022): 222-229.*

4.1. INTRODUCTION

The electrochemical CO_2 reduction reaction (CO_2RR) is a key enabler to the production of value added chemicals such as CO, ethylene, ethanol, formic acid, and other products[1–7]. To achieve industrially relevant reaction rates (>100 mA/cm^2) and lower costs versus alternate production routes, CO_2RR using gas-diffusion electrodes (GDEs) in a membrane electrode assembly (MEA) configuration is an attractive option due to their reduced cell voltages[8–14].

In a MEA configuration for CO_2RR, anion exchange membranes (AEMs) are commonly adopted as the anode and cathode separator, as this maintains an alkaline environment at the cathode, which is more favorable for CO_2RR selectivity than acidic media. Such a configuration is inherently unstable, however, as excess acidic CO_2 is continually fed into the reaction environment, leading to two operational challenges. First, the loss of reactant CO_2 due to its reaction with electrogenerated hydroxide (OH^-) ions decreases CO_2 utilization significantly[15]. Second, due to low liquid volumes and high ion concentrations in the pores of the cathode in an MEA configuration, (bi)carbonate salts are highly prone to precipitate in the cathode catalyst layer, gas-diffusion layer, and CO_2 gas channel[16]. Salt deposits have been shown to block access of CO_2 to catalytic sites while accelerating GDE flooding, which further reduces the amount of CO_2 reaching the catalyst. Each of these aspects causes the spatial catalyst utilization of a planar electrode area to be decreased during operation, resulting in the competing hydrogen evolution reaction (HER) to replace CO_2RR in these regions and an overall lower CO_2RR Faradaic efficiency being measured[17, 18].

Additionally, as the geometric area of electrolyzers increases and higher single-pass conversion efficiencies are targeted [19–21] a spatial variation in reactant distribution will also be present along the gas channel of a reactor as reactant is consumed. Importantly, since the area of the gas channel in contact with the GDL is much less than the geometric catalyst area, gas must also be transported in-plane through the GDL to reach catalytic sites adjacent to the current collector (see Figure 4.1a). Such transport can occur through both diffusion and under-rib convection of CO_2, which is heavily influenced by the flow field design that is used. Without proper consideration of transport from the gas channel to the immersed catalyst layer, some areas of the catalyst layer may be depleted of CO_2 even if ample CO_2 is still present in the gas channel. In brief, there are a multitude of factors which then affect the ability for CO_2 to reach all geometric areas of a CO_2 electrolyzer and for the catalyst to be fully “utilized” for CO_2RR.

These temporal and spatial mass transport effects in CO_2 electrolyzers lower the usefulness of the catalyst layer for CO_2 reduction. A way of combining these mass transport effects is by considering geometric catalyst utilization of a CO_2 electrolyzer, which can then be defined as the ratio of the planar catalyst area utilized for CO_2RR (desired reaction) to the total planar catalyst area present in the system. Recent studies have considered broader mass transport efforts for mapping spatial electrochemical activity[22] and engineering catalyst layers for maximizing multi-carbon products from CO_2RR,[23–25] but these have yet to be considered as changing in time.

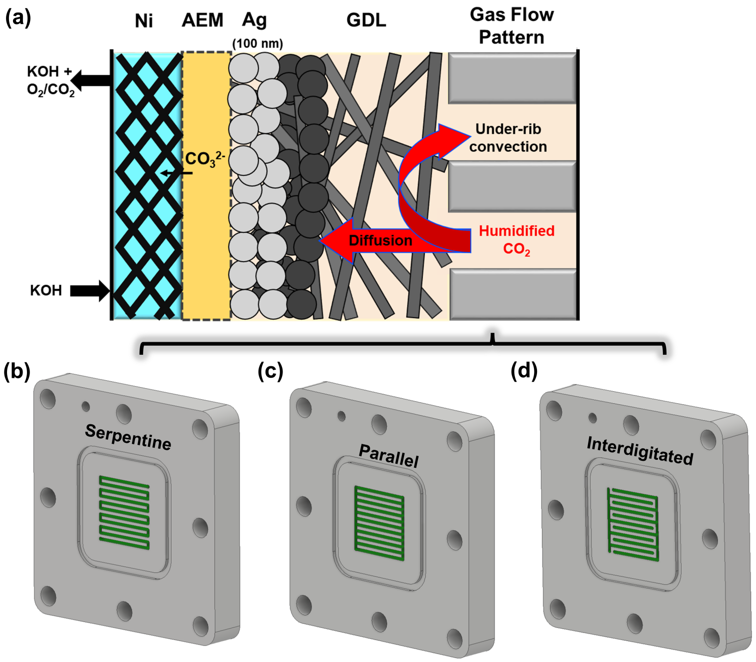

Figure 4.1: (a) Illustration of the components of an exchange MEA cell with the Ag catalyst layer sputtered on a carbon gas-diffusion layer. Shown here are the three different flow patterns at the cathode used in the study: (b) serpentine, (c) parallel and (d) interdigitated.

One way to probe geometric catalyst (GCU) utilization is by measuring changes in activity, selectivity, and stability using modified gas flow patterns at the cathode, which distribute reactants to the GDE. As shown in the parallel electrochemical fields of PEM electrolyzers and fuel cells, the gas flow pattern will impact mass transport and reactant distribution at the catalyst surface significantly[26–28]. The three commonly adopted flow patterns are the serpentine, parallel, and interdigitated designs. As shown in Figure 4.1b, a serpentine flow channel has a single fluid flow path from the inlet to outlet of the reactor, resulting in a plug flow configuration[29].The transport mechanism of reactants through the GDE to the catalyst layer is a combination of diffusion and convection under the ribs (under-rib convection) driven by higher pressure drops[30]. In contrast, a parallel flow channel exhibits a very low pressure drop[31] due to the distribution of fluid into parallel channels (Figure 4.1c). Due to insignificant differences in gas pressure between each channel, through-plane and in-plane diffusion becomes the primary mode of mass transport from the gas channel to the catalyst. The final flow pattern commonly adopted is the interdigitated design where flow paths are dead ended, [32] making the reactant gases flow through the GDE by forced convection (Figure 4.1d). Notably, the parallel and interdigitated designs both have multiple parallel paths to the outlet, while serpentine follows a singular gas channel. The differences in transport properties of each design are then a possible tool for assessing catalyst utilization in CO_2RR systems if paired well with experimental and modeling findings.

In this study, we performed CO_2 electrolysis on a Ag GDE using three different flow patterns at the cathode side of an MEA electrolyzer. The different flow patterns were employed to better understand the factors impacting geometric catalyst utilization using measured Faradaic efficiency and modeled CO_2 concentrations. In addition, mass transport limitations due to salt precipitation were studied by imposing a PTFE blockage at the gas flow pattern, obstructing reactants from reaching catalyst sites. Consequently, the serpentine flow pattern showed the highest partial current density for CO production (205 mA/cm^2) and the highest resistance to flooding, resulting in a higher catalyst utilization. Spatial variations in CO_2 concentration were estimated using a 3D mass transport and fluid flow model, which revealed significant differences in the reactant distribution at the GDE surface. These findings can be used to formulate design rules for industrially relevant CO_2 electrolyzers.

4.2. RESULTS AND DISCUSSION

The MEA cell with a Ag GDE cathode, Ni foam anode, and anion exchange membrane (AEM) combined into one unit is shown schematically in Figure 4.1a. Humidified CO_2 was fed as the reactant through the flow channel at the back of the GDE, which is then distributed to the catalyst layer by diffusion and convection through the GDL. Critically, the gas flow pattern on the flow plate at the back of GDE impacts the degree of CO_2 transport to the entire geometric area (5.06 cm^2), which is much larger than the channel area itself (2.53 cm^2). Gas transport from the gas channel to the covered areas of the GDE is then needed to achieve full geometric catalyst utilization. We designed cathode end plates made of stainless steel with identical gas channel areas and similar rib spacing with serpentine, interdigitated, and parallel flow patterning. The channels differ, however, in their means of gas distribution. For each of these flow fields, we performed CO_2 electrolysis using a Ag GDE for CO and formate production and 0.5 M KOH as anolyte in an exchange MEA configuration (see Figure S1 for details of the setup).

Two types of experiments were performed to analyze different effects related to geometric catalyst utilization. In the first set of experiments, we specifically examined product selectivity under varied current densities in low reaction times (<10 min). We can then assess CO_2 distribution in the absence of flooding or salt precipitation. In the second set of experiments, we analyze longer experiments where flooding and salt formation are known to occur and observe the differences in performance for the different flow fields. We can then separate catalyst utilization into two time scales.

4.2.1. GCU VARIES AT HIGHER CELL VOLTAGES

In the first set of experiments, CO_2RR was performed at constant cell voltages ranging from -2.0 V to -3.0 V in 20 min increments (Figure S2). As shown in Figure 2a,b, we found that CO_2RR using all three flow patterns showed similar partial current densities for CO and H_2 at lower cell voltages. At these lower current densities, we then conclude that CO_2 can then reach all catalytic surfaces equally, and the catalyst performance is similar. However, at a higher cell voltage of -2.76 V, the serpentine flow pattern performed better, achieving a CO partial current density (j_{CO}) of 205 mA/cm^2. The interdigitated flow pattern also showed a similar j_{CO}, but for the parallel flow pattern, a significant decrease in j_{CO} was observed, dropping to 153 mA/cm^2. At the same time, j_{H_2} increased to 74 mA/cm^2 at -2.76 V for the parallel flow pattern, suggesting mass transport limitation arises. To investigate this further, we built a numerical transport model of the gas flow channel and GDE (Table S1) similar to our previous work [33].

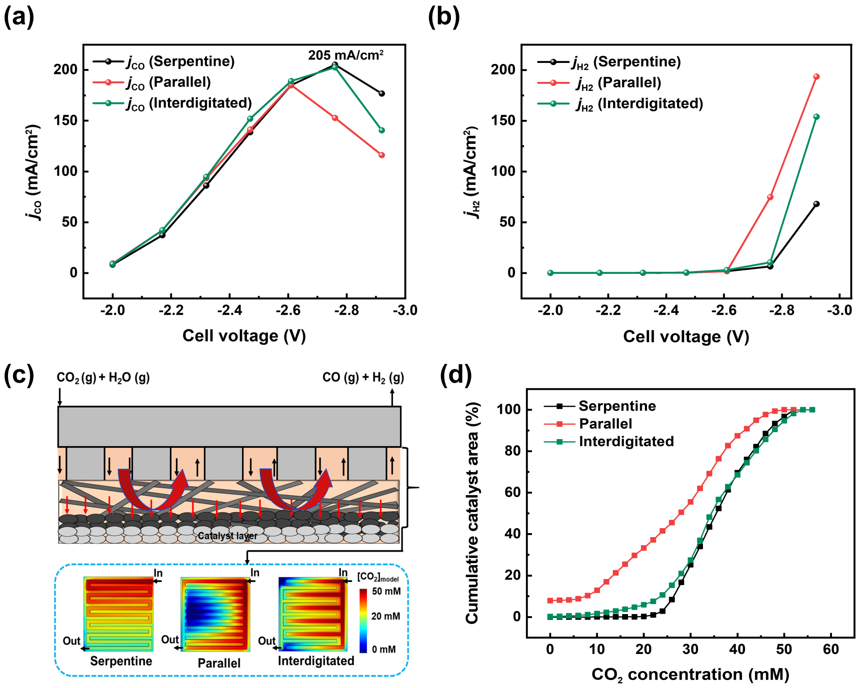

Figure 4.2: Partial current density of (a) CO and (b) H_2 for the different flow channels. (c) Schematic of the transport model used to estimate the spatial CO_2 distribution inside the reactor. (d) Cumulative distribution plot of catalyst area with CO_2 access for the three flow patterns calculated from the model at a cell voltage of -2.76 V.

Observing the modeling results in Figure 2c,d, significant differences in CO_2 distribution are predicted at the interface of the microporous layer and catalyst layer for the three flow patterns. In particular, the modeling results showed a radial distribution of CO_2 on the GDE surface for a parallel flow pattern that forms a dead zone near the center of the GDE (Figure S3). Consequently at -2.76 V, over 8% of the GDE surface has no CO_2 access (Figure 2d), and these regions would primarily produce H_2 from water present at the catalyst surface. In contrast, the serpentine flow pattern shows no CO_2 mass transport limitation and a relatively homogeneous reactant distribution (black line).

The interdigitated flow pattern is closer to the serpentine channel in terms of CO_2 distribution at the GDE surface as shown in Figure 2d, due to convection dominated transport from the gas channel through the GDE that ensures a relatively high CO_2 concentration under the steel channel ribs. The effect of gas channel path length and under-rib convection can be seen directly in the different pressure drops between the inlet and outlet for each flow field. Here, the serpentine channel had a pressure drop 81% larger than the interdigitated channel and 936% larger than the parallel channel (see Table S2).

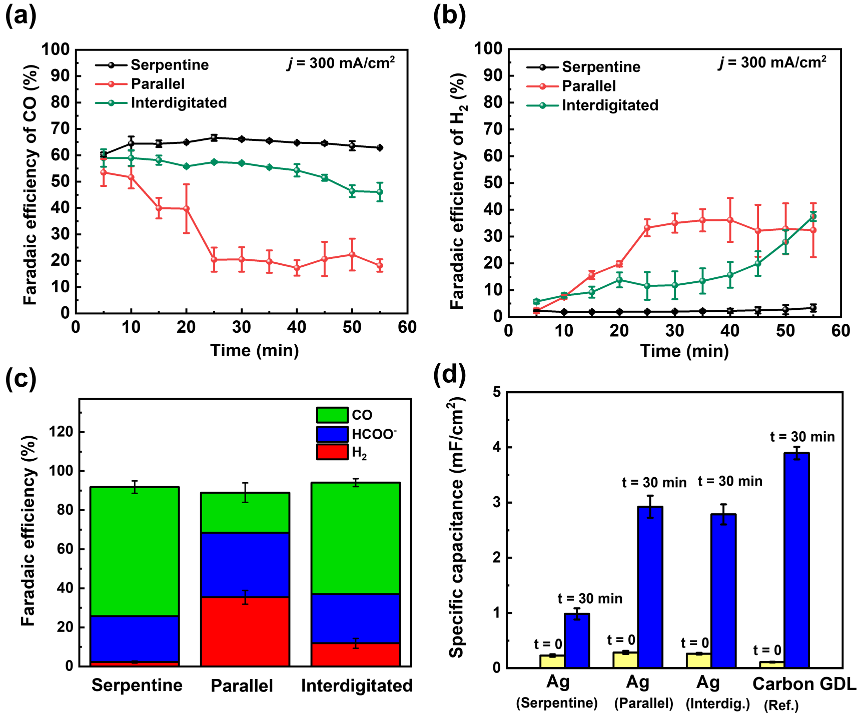

Figure 4.3: Faradaic efficiency of (a) CO and (b) H_2 with time during 1 h of electrolysis.(c) FE of CO, H_2, and HCOO– at 300 mA/cm^2 after 30 min of electrolysis.(d) Specific capacitance of a Ag GDE and bare carbon GDL before and after 30 min of electrolysis. Error bars represent the average of

three independent experiments.

4.2.2. TIME DEPENDENT GCU

To further determine how catalyst utilization changes with time, we performed electrolysis at a geometric current density of 300 mA/cm^2 for 1 h for the three flow fields. This operating range was chosen, as previous literature shows that flooding and salt precipitation will happen in a short period of time, allowing for the catalyst utilization to be assessed during a 1 h test. The advantage of performing constant current operation is that the total charge applied is fixed, which results in a constant mole of 2e– products that are produced (Table S3), in this case, CO, H_2, and formate ($HCOO^-$). Although CO and H_2 can be measured continuously, formate is only measured at the end of the test by sampling the anolyte and flooded drops from the cathode GDE. Formate was quantified using HPLC analysis (Tables S4 and S5), leading to a total FE of 90–93%. Some of the missing products can be attributed to the oxidation of formate ions at the anode as reported previously[34].

As shown in Figure 4.3a and 4.3b, the serpentine flow pattern showed a relatively stable CO selectivity of 65% and a H_2 selectivity of 2.5% during 1 h of operation. However, for the interdigitated and parallel flow patterns, drops in CO selectivity to 46.2% and 19.7% were observed, respectively, after 1 h of operation. The drop in CO selectivity and increase in H_2 indicate that CO_2 is increasingly unable to reach all parts of the Ag catalyst over time and that flooding or salt formation for the three patterns occurs after different periods of time. In addition, a higher formate selectivity was also observed for the parallel flow pattern (Figure 3c). This increase in formate selectivity can be attributed to a higher $^*H$ coverage at the catalyst surface due to the depleted local CO_2 concentration as has been shown in previous reports [35–37].

To examine the effect of flooding on catalyst utilization over time, we performed electrochemical double-layer capacitance (EDLC) measurements before and after 30 min of electrolysis (Figure S4). EDLC is a technique that can be used as a proxy for the wetted area of GDE by observing how the capacitance of a system changes over time[38]. Since the Ag catalyst layer (100 nm sputtered silver) has a fixed surface area that is assumed to be fully wetted, increases in capacitance during operation can be attributed to the wetting of the carbon in the GDL via flooding. One can then obtain specific capacitance values by dividing measured EDLC with the geometric area of the cathode to approximate the degree of flooding of the GDL.

As shown in Figure 3d, specific capacitance values clearly reveal that different degrees of water are present in the carbon GDL when operated using different flow patterns. The serpentine flow pattern showed the lowest specific capacitance of 0.98 mF/cm^2 after 30 min of electrolysis, suggesting a smaller wetted area of the carbon GDL and a higher resistance to flooding. On the other hand, both the parallel and interdigitated flow patterns show around a 3-fold increase in specific capacitance (2.8 mF/cm^2) compared to that of the serpentine case. In addition, a bare carbon GDL with no Ag catalyst layer showed a specific capacitance of 3.7 mF/cm^2 after 30 min of electrolysis. These results reveal three important findings. First, a clear increase in the fraction of flooded catalyst pores occurs for the Ag GDE when operated with parallel and interdigitated flow patterns. Flooded areas will then prevent CO_2 from traveling from the gas channel through the GDE to all catalyst sites, thus lowering catalyst utilization and increasing HER [39]. Second, an inverse correlation between CO selectivity and specific capacitance is observed over time showing that the catalyst utilization for CO_2 electrolysis is significantly affected by the wetted area. And last, despite the interdigitated channel showing a similar degree of flooding to the parallel channel (Figure 3d), the CO performance is maintained over a much longer period.

4.2.3. EFFECT OF PTFE BLOCKAGE IN THE GAS FLOW CHANNEL

Observing the results in Figure 3, the single-path serpentine channel clearly outperforms the two multipath channels. When we look at the salt deposition at the end of the 300 mA/cm^2 experiments, however, all flow field patterns are heavily blocked by $KHCO_3$ (Figure 4.9) and water (Figures 4.10). We then wanted to perform more controlled experiments to determine how gas channel blockages (in the form of liquids or salts) may impact catalyst utilization of an entire GDE and determine the reasons on why some flow patterns can be more resistant to changes in performance. Specifically, these control experiments should be performed with pristine GDEs and gas channels initially devoid of water or salt. To accomplish this, we placed a PTFE blockage in the gas flow channel behind the GDE from time t = 0. We can then observe with more control the distribution of CO_2 to different areas of the silver catalyst surface.

As shown in Figure 4.4a, we found that there was relatively no difference in CO selectivity for the serpentine flow pattern with or without the PTFE block. This suggests that the reactant gas can bypass such blockages due to the continuous flow path from the inlet to the outlet of the reactor while still allowing CO_2 to reach all parts of the 5 cm^2 catalyst area. A consequence of this, however, is that the modeling results predict a substantial increase in the inlet pressure of the reactor from 143 Pa with no PTFE block to 749 Pa with the PTFE block (Table S2). Such a large pressure drop increase indicates that CO_2 flow can subvert the blockage by allowing for the entire flow to go in-plane through the GDE (Figure S8). These observations highlight the benefit of a single-path flow field in the event of flooding or salt formation (Figure S9) in the gas channel, at the expense of increased pressure drops. The modeling results shown in Figure 4c confirm the experimental conclusion, revealing that only a small portion of catalyst area is predicted to be without CO_2 access (3%). Such benefits of higher pressure drop are also in agreement with a recent report on a Au GDE, where a higher pressure drop was found to increase reactant transport and stave off flooding [40].

For the interdigitated flow pattern, a PTFE block was placed in the first set of interdigitated fingers (see Figure 4.4b). In contrast to the serpentine case, the interdigitated flow pattern with the PTFE block showed an 8% drop in CO selectivity compared to the unblocked case (50.9%) after 5 min. This gradually decreased to 41.9% after 30 min (Figure 4b). Further, unlike the modeling of the serpentine channel, which showed little overall difference in predicted CO_2 distribution (Figure 4c), as much as 6.2% of the catalyst area had no access to CO_2, which is twice as large as that observed for the serpentine case. Notably, the modeled pressure drop increase with and without the PTFE blockage was substantially less than for the single-path serpentine case. This result then elucidates the challenges with a multipath gas channel when failures begin to occur. Because gas will follow the path of least resistance, gas flow in a multipath system will avoid blocked areas as evident from the model data (Figures 4d and S7). Such observations for CO_2RR are then not dissimilar to those in fuel cells when water is being removed [41–44].

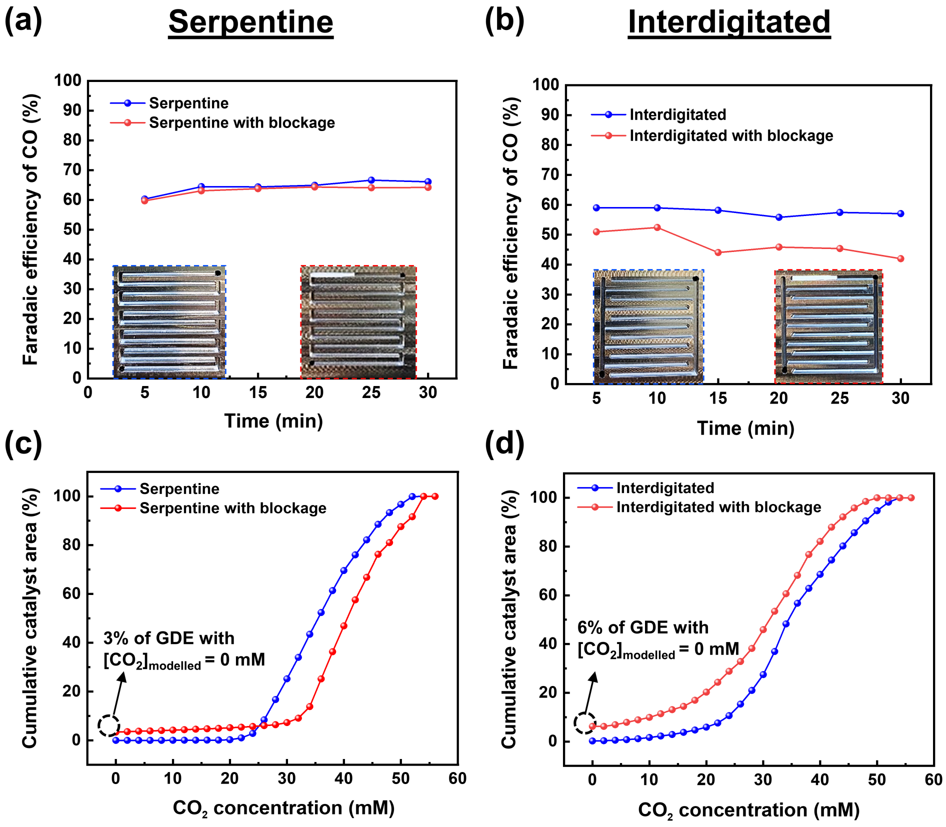

Figure 4.4: Experimental results of CO selectivity with and without the PTFE block for (a) serpentine and (b) interdigitated flow patterns. The insets depict the gas flow pattern with and without the PTFE blockage. Modeling results show the cumulative distribution plot of catalyst area with CO_2 access with and without the PTFE blockage for (c) serpentine and (d) interdigitated flow patterns.

In addition, emphasis on the design parameters of the flow field patterns must be investigated to unravel the differences in CO_2RR activity on different regions at the catalyst surface. The channel area (2.53 cm^2), which is smaller than the surface area of GDE (5.06 cm^2), might then have different activity due to differences in reactant concentration. For example, a higher gas flow channel-to-rib width ratio reduces under-rib convection and pressure drop, thus reducing CO_2 flux to the catalyst surface. Optimizing such parameters might then become crucial to avoid device failures. Finally, the higher fraction of CO_2 lost to hydroxide ions for the serpentine flow pattern (Figure S10) shows that an increase in catalyst utilization is accompanied by an overall increase in (bi)carbonate formation. This apparent contradiction is a combined result of the serpentine flow channels' more even CO_2 distribution throughout the entire catalyst layer (Figure 2d), which leads to overall greater carbonate formation as well as its ability to maintain a less flooded gas-diffusion layer due to under-rib convection (Figure 3d). Alternate strategies such as the use of a bipolar membrane electrode assembly [20, 45] for CO_2 regeneration from carbonate ions might then become promising, albeit at the cost of higher cell voltages required for water dissociation reaction in the membrane. Understanding such trade-offs might pave the way towards commercializing CO_2 electrolyzers for industrial operation.

4.3. CONCLUSION

In conclusion, we have shown that gas flow field design at the cathode side of a CO_2 electrolyzer significantly alters the performance at higher current densities owing to differences in mass transport, spatial reactant distribution and (bi) carbonate precipitation at the cathode. The serpentine flow field owing to the higher pressure drop generated in the reactor, resists flooding of the GDE at 300 mA/cm^2 and maintains a stable CO_2RR performance without significant HER. For large scale reactors, future works should investigate the influence of a design combining the benefits of serpentine and parallel flow field design to ensure sufficient mass transport as well as acceptable pressure drop are obtained in the reactor to reduce overall energy requirements.

4.4. SUPPLEMENTARY INFORMATION

4.4.1. EXPERIMENTAL

All experiments were performed in a custom made membrane electrode assembly (MEA) cell comprising of a serpentine flow channel on the anode and different flow field patterns at the cathode. Sigracet 38 BC gas diffusion layers (GDL) of 5.06 cm$_2$ area (2.25 cm x 2.25 cm) was used as the porous transport layer. Ag catalyst layer was deposited on top of microporous layer of GDL by direct currentmagnetron sputtering under 3 µbar Ar flow to form a uniform film of 100 nm Ag catalyst layer. Nickel foam (3 cm x 3 cm, Recemat BV) was used as the anode. Ag GDE and Ni foam were combined with an oversized 16 cm$_2$ (4cm x 4cm) Sustainion anion exchange membrane (X37-50 Grade RT) to assemble the MEA. 0.5 M KOH solution was fed at the anode at a constant flow rate of 20 ml/min and recirculated using a peristaltic pump.

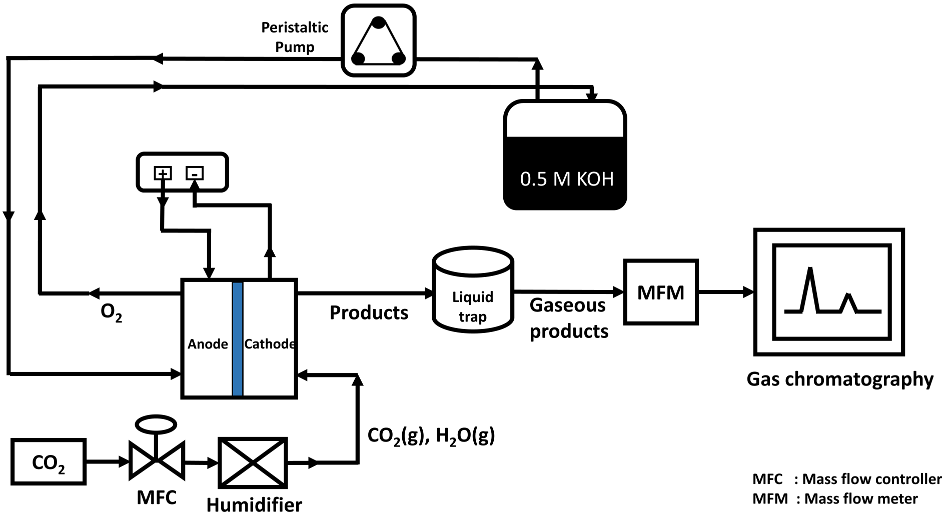

Figure 4.5: Flow diagram of the experimental setup used for CO2 electroreduction in an exchange MEA.

A constant CO_2 feed rate of 50 sccm was used and the humidity at the inlet was fixed at 75%. Electrolysis at constant cell voltages between -2 V and -3 V were performed for 20 minutes each and product quantification was performed using gas chromatography (GC) with periodic injections every 5 minutes.

CATALYST PREPARATION AND CHARACTERIZATION

Direct current magnetron sputter deposition technique was used to sputter a thin layer of Ag catalyst layer on top of Sigracet 38 BC GDL. A thickness of 100 nm was deposited and relationship between thickness and deposition rate was calibrated by depth profiling a glass piece after 10 min of sputtering. Sputter deposition of Ag catalyst on GDL was performed at 3 µbar in an argon atmosphere at a rate of 3.125

Å/s resulting in a mass loading 0.108 mg/cm^2. The morphology of the sputtered catalyst layer was determined using scanning electron microscopy (SEM) analysis (Figure 4.10).

POTENTIOSTATIC CO_2RR RESULTS FOR THE THREE FLOW FIELD PATTERNS

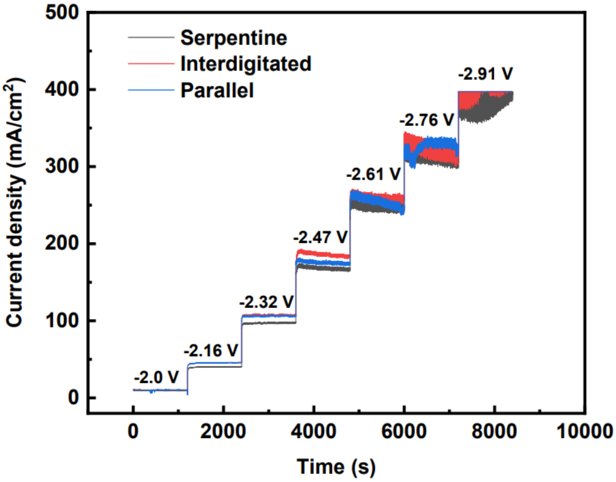

Figure 4.6: Variation of current density at constant cell voltages during CO_2RR for the three flow field patterns. Constant cell voltages were held for 1200 seconds each.

FARADAIC EFFICIENCY AND CARBON BALANCE CALCULATION

The Faradaic efficiency of gaseous products and CO_2 consumption to hydroxide ions were calculated similar to calculations shown in Supplementary section in Chapter 3.

MODEL DESCRIPTION

A 3D geometry of the cathode compartment (5cm^2 area) comprising of the three flow channel designs (serpentine, parallel and interdigitated) were modelled with the same length (2.1 cm), width (1 mm) and depth (1 mm) in COMSOL Multiphysics 5.5. A carbon GDL of dimensions (2.25 cm x 2.25 cm x 0.325 cm) was modelled and placed in contact with the flow field pattern with each one consisting of 11 channels and 10 ribs. The numerical simulations were performed using a MUMPS general solver with a relative tolerance of 0.001 to calculate the CO_2 concentration gradient in the gas channel and catalyst surface. All physics tools for fluid flow and reactant distribution were modelled similar to the modelling work shown in Chapter 3.

MODELLING RESULTS OF CO_2 CONCENTRATION AT THE G-L INTERFACE

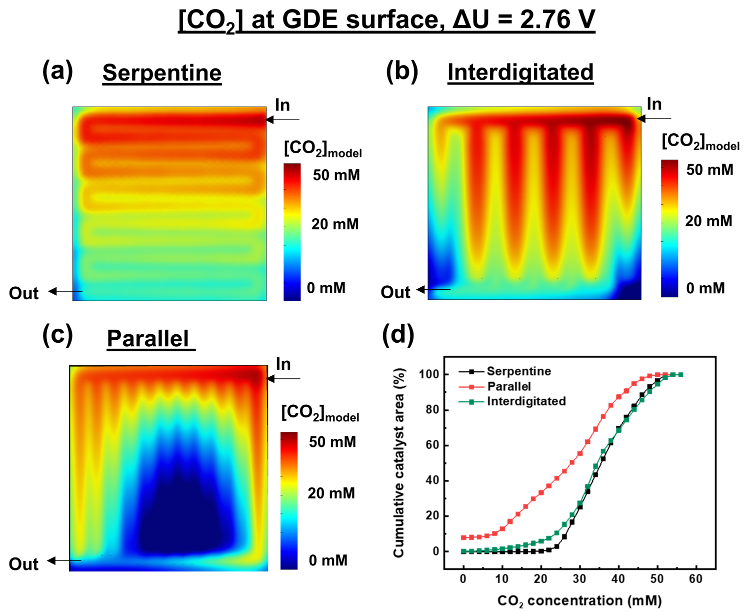

Figure 4.7: Simulation results of gas phase CO_2 concentration at the interface of microporous layer and catalyst layer for (a) serpentine,(b) interdigitated and (c) parallel flow channel design.(d) A cumulative distribution plot of catalyst area with CO_2 access for the three flow patterns.

DOUBLE LAYER CAPACITANCE MEASUREMENTS

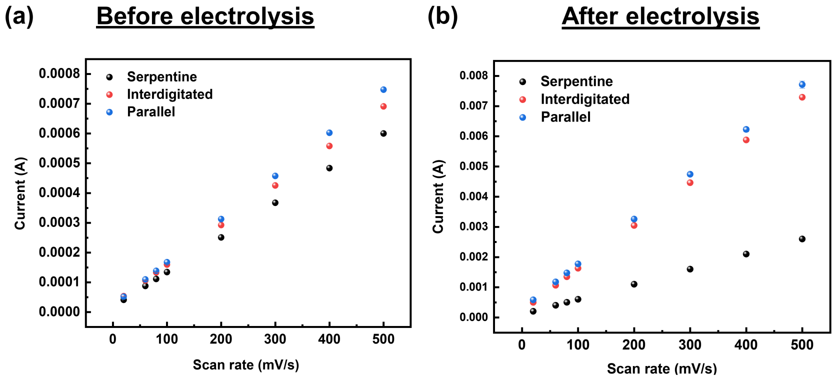

Figure 4.8: Double layer capacitance of Ag sputtered GDE before and after electrolysis of 30 min at a current density of 300 mA/cm^2 for the three flow channel designs. Shown in the y-axis is the charging current averaged by anodic and cathodic currents with the scan rates on the x-axis.

Double layer capacitance measurements were performed before and after CO2RR at 0.1 V non-Faradaic potential range and various scan rates from 500 mV/s to 20 mV/s with multiple cycles. The slope of the charging current as a function of scan rate was taken to be the capacitance.

IMAGES OF SALT PRECIPITATION IN THE GAS FLOW CHANNEL AND GDE

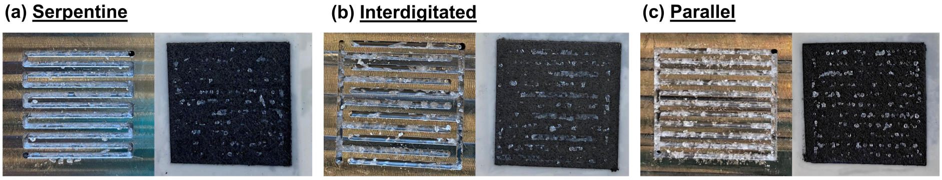

Figure 4.9: Images of cathode flow channel and back of GDE after electrolysis for (a) serpentine, (b) interdigitated and (c) parallel flow channel at 300 mA/cm^2 showing salt crystals blocking the gas flow channels and back of the GDE.

SEM ANALYSIS

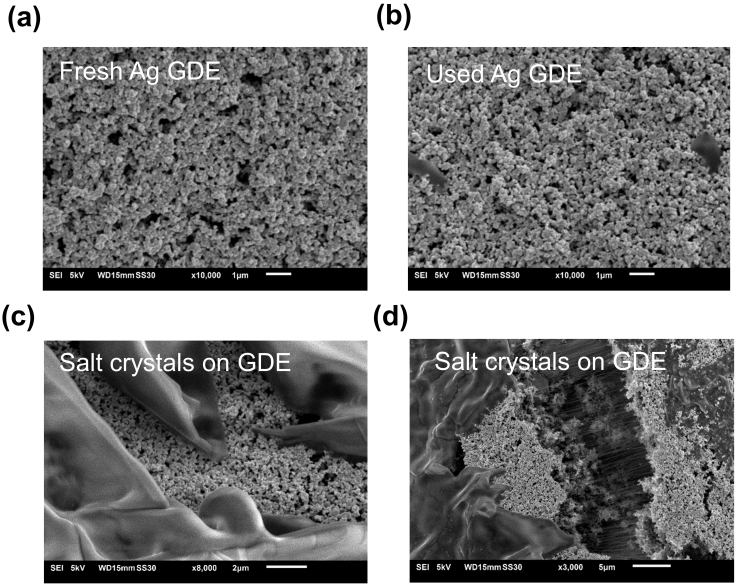

Figure 4.10: SEM images of Ag catalyst sputtered on Sigracet 38 BC gas diffusion layer (a) before electrolysis,(b) after electrolysis for the serpentine flow pattern.(c) and (d) Salt crystals precipitating at the GDE surface and stretching of the carbon fibers are observed.

MODELLING FLOW CHANNEL DESIGN WITH THE PTFE BLOCK

To model the experimental results of serpentine and interdigitated flow channel design with the artificially imposed PTFE blockage, we added a block of same dimensions (2 cm x 0.1 cm x 0.1 cm) in the 1st gas channel from the inlet. An interior wall boundary condition was imposed at the walls of PTFE block to the mimic blockage of gas flow.

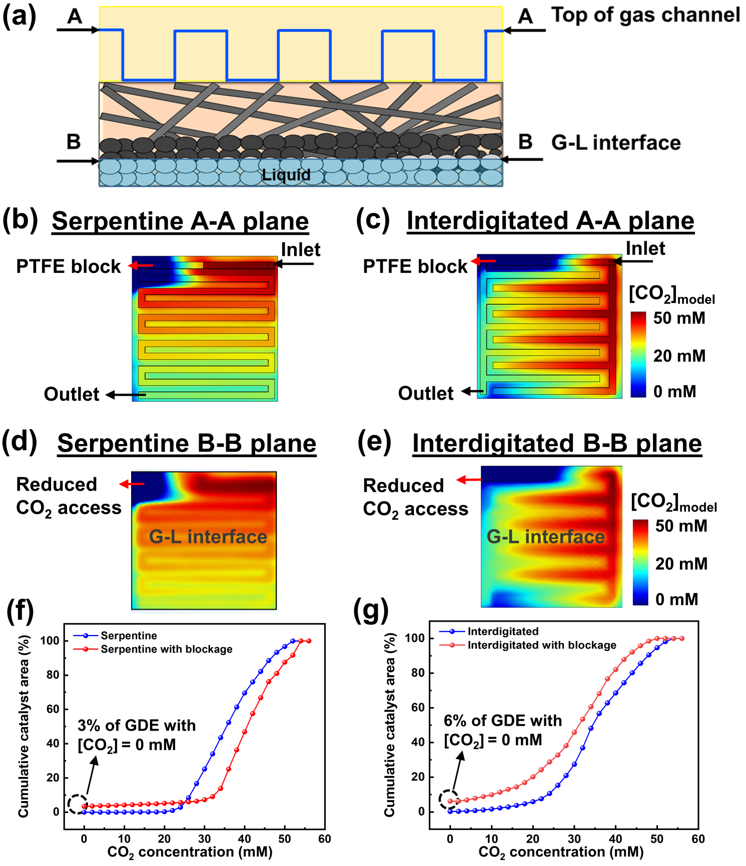

Figure 4.11(a) Schematic of the model with the imposed PTFE blockage in the gas flow channel showing two different planes, A-A plane representing top of gas flow channel and B-B plane for the gas-liquid interface. (b) CO_2 concentration from A-A plane for (b) serpentine case,(c) interdigitated case. CO_2 concentration from B-B plane for (d) serpentine and (e) interdigitated case. Cumulative distribution plot of catalyst area with CO_2 access with and without PTFE block for (f) serpentine (g) interdigitated flow channel is shown.

Table 4.1: Modelling results of pressure drop b/w inlet and outlet for the three flow field patterns with and without the PTFE blockage imposed at the gas channel.

Flow field pattern	ΔP b/w inlet and outlet (Pa)	Pressure drop with PTFE block (Pa)	Avg. velocity through GDL	Avg. velocity through GDL with PTFE blockage	Avg. [CO_2] at G-L interface	Avg. [CO_2] at G-L interface with PTFE blockage
Serpentine	143.0	749.0	7.16	14.47	38.7	36.05
Interdigitated	79.0	61.0	7.36	7.16	36.84	35.58
Parallel	13.8	15.1	0.33	0.36	30.33	26.21

4.4.2. CROSS SECTIONAL SEM ANALYSIS

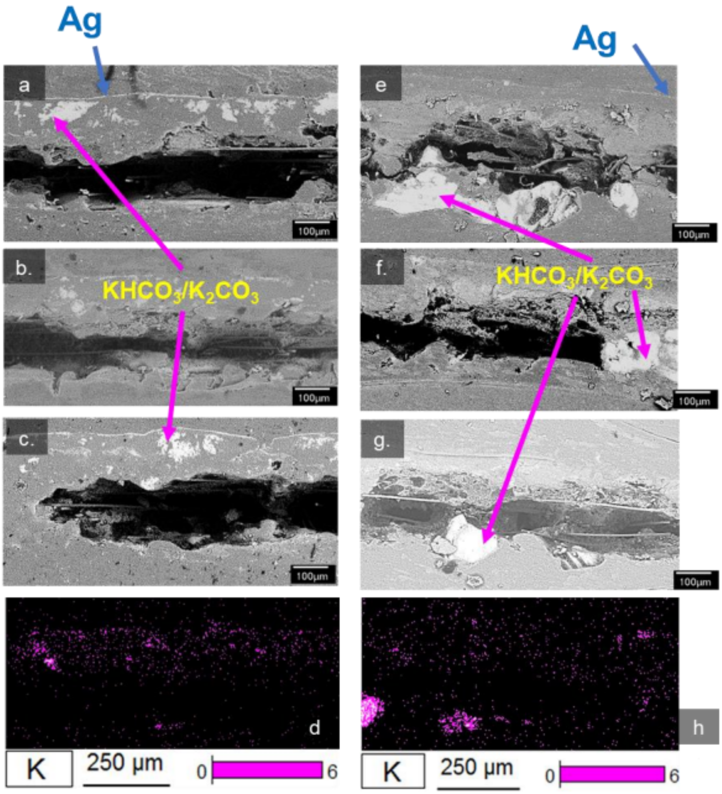

Figure 4.12: Cross sectional SEM images of Ag GDE after 30 min of electrolysis for (a)-(d) serpentine and (e)-(h) interdigitated flow field patterns. Potassium salt crystals are visible in the microporous layer and carbon fiber substrate of the GDL.

Cross sectional SEM analysis was performed for Ag-GDE samples after 30 minutes of electrolysis for serpentine and interdigitated flow patterns. Ag-GDEs after CO_2 electrolysis tests were cast in a mould with a polymeric resin. After an over-night hardening step, the casts were hard polished with emery papers (500 – 2000 grid)until the mid-part of the GDEs followed with a fine-surface finishing dry pads (+4000 and diamond pads). The cross-sectional SEM analysis were conducted with a scanning electron microscope (Jeol JSM-6500F, Japan) coupled with an energy-dispersive X-ray spectrometry detector (Ultradry, Thermofischer, USA).

As shown in Figure 4.12, back-scattered SEM images display a fine bright line which is the sputtered A catalyst layer (100 nm). The potassium (bi) carbonate salt precipitates are visible both in the microporous layer and carbon fiber layer (CFL) of the GDE (Figure 4.12 b,c,f,g). However, Ag-GDE operated with serpentine and interdigitated flow patterns showed differences in salt concentrations throughout the GDE. As shown in Figure 4.12(e), Ag-GDEs operated with interdigitated flow pattern displayed larger salt precipitates at the CFL. Although it is harder to make substantive conclusions from cross-sectional SEM and EDX analysis as shown in a recent study [46], we observed higher concentration of K^+ ions in CFL for the interdigitated case (Figure 4.12h). This suggests a higher degree of electrolyte intrusion (flooding) into the GDE.

In contrast, a more uniform distribution of K^+ ions are visible for the serpentine case suggesting a relatively less electrolyte intrusion (flooding) into the GDE. This agrees closely with the experimental observation of an increased rate of flooding for the interdigitated flow pattern. These differences might stem from the non-uniform CO_2 concentration at the surface of GDE for the interdigitated flow pattern as predicted from the modelling results. In addition, a higher CO_2 concentration under the ribs for the interdigitated case (Figure 4.7) might explain why some regions have a higher salt precipitation. In contrast, a uniform CO_2 distribution throughout the catalyst surface might enable a more uniform salt distribution and a relatively less electrolyte intrusion into the CFL for the serpentine flow pattern.

CARBONATE : HYDROXIDE RATIO AT THE CATHODE

The fraction of CO_2 reacting with OH^- ions varied for the three flow patterns at 300 mA/cm^2 constant current operation.

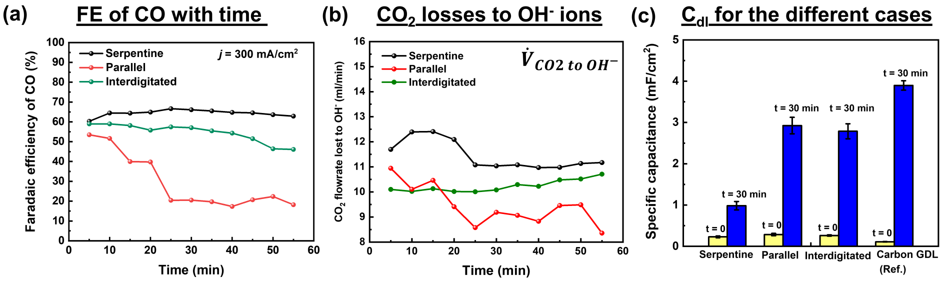

Figure 4.13: (a) FE of CO with time , (b) comparison of the volumetric flowrate of CO_2 reacting with OH^- ions at 300 mA/cm^2 and (c) Double layer capacitance measurements after 30 minutes for the three flow field patterns.

As shown in Figure 4.13, the serpentine flow pattern has the highest fraction of CO_2 lost to OH^- ions followed by the interdigitated and the parallel flow fields. Parallel flow pattern in particular showed a constant drop in this fraction during CO_2RR, suggesting a decrease in carbonate: hydroxide ratio at the cathode due to flooding of the GDL.

4.4.3. STABILITY TEST USING $KHCO_3$ ANOLYTE

Using 0.1 M $KHCO_3$ as anolyte, we performed a stability test for 20 hours at a current density of 200 mA/cm^2. An IrO_2 anode was used for the OER at anode. The obtained results are shown in Figure 4.14.

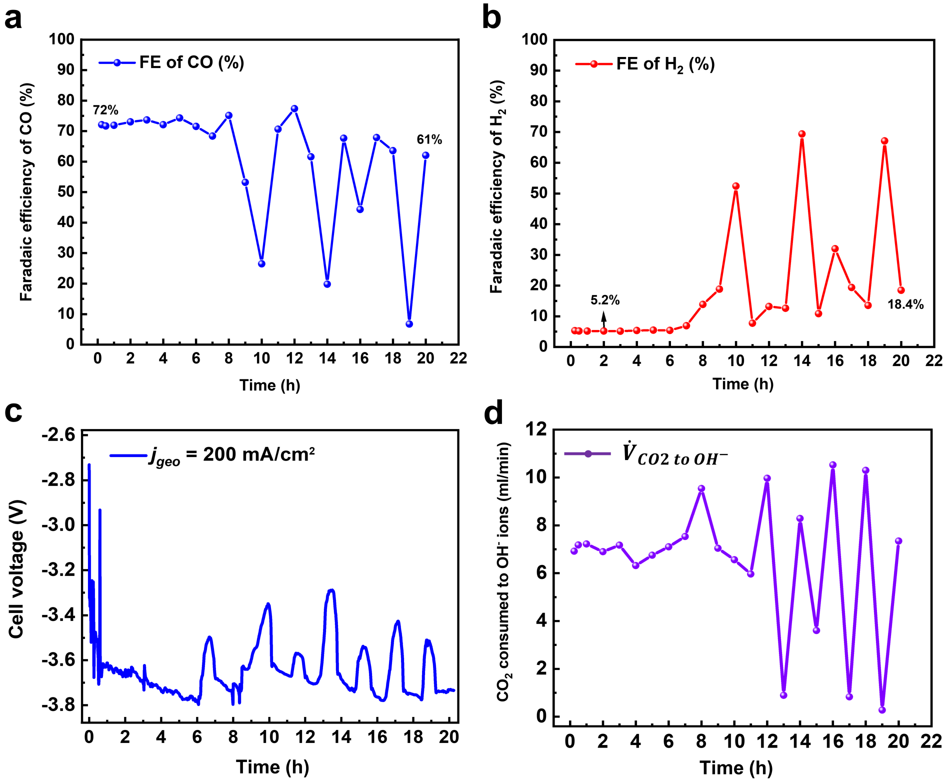

Figure 4.14: (a) FE of CO with time , (b) FE of H_2 with time, (c) Cell voltage at 200 mA/cm^2 during the 20 h test, (d) Volumetric CO_2 flowrate consumed to hydroxide ions during the test, estimated using carbon balance at the cathdode.

An interesting observation is the periodic oscillations in FE of CO and H_2 as shown in Figure 4.13a and 4.13b. For the first 8 hrs, a stable CO FE of 72 % and H_2 FE of 5% is observed. After 8 hrs, a drop in FE of CO and a gradual increase in H_2 FE is seen. This drop in CO selectivity can be attributed to the onset of salt precipitation at the cathode, causing blockage of active sites and gradual decrease of hydrophobicity of MPL of the GDE.

Importantly, after 10 hrs, the FE of CO started rising again from 26.5% to 75% at about 12 hrs. The opposite trend was observed for H_2 with a steady drop from 52% at 10 hrs to 5% at 12 hrs. This clearly shows that the instability of CO_2RR due to salt precipitation and flooding is not linear but an oscillatory effect is seen here. Additionally, similar effects are seen in cell voltage and the fraction of CO_2 consumed to hydroxide ions (Figure 4.14c and d). The drop in total cell voltage during decreased CO_2RR and subsequent drop in CO_2 losses to hydroxide ions shows that the dominant charge carrier across the membrane switches to OH^- instead of CO_3^{2-} ions, during this temporary drop in CO_2RR activity. It is well known that these anion exchange membranes have higher affinity for hydroxide conduction compared to carbonate conduction which then explains the drop in cell voltage during the drop in CO_2RR to CO selectivity.

Recent work by Moss et.al [47] using MEA cell and in- operando X-ray diffraction study showed similar effect, with an important finding of pulsed performance decay. They showed that as salt precipitation blocks CO_2 access to catalyst sites, HER starts increasing with a simultanoeus drop in carbonate formation and a shift in OH^- ion becoming the dominant charge carrier across the membrane. During this temporary drop in performance, some flooding inside the GDE results in partial dissolution of the produced salt crystals. Consequently, this dissolution causes a recovery for CO_2RR resulting in increased selectivity for CO_2RR and subsequent drop in HER. This gradual switch occurs for a certain time and the cycle starts over again. It is essential to mention here that this work had used a Cu based catalyst for CO_2RR. Considering that we used a Ag catalyst for CO_2RR and see oscillatory effect similar to Cu, clearly implies that this phenomena occurs due to salt precipitation and gradual loss of GDE hydrophobicity, both of which are independent of the catalyst used.

REFERENCES

[1] Y. Hori, H. Wakebe, T. Tsukamoto, and O. Koga. “Electrocatalytic process of CO selectivity in electrochemical reduction of CO2 at metal electrodes in aqueous media”. In: *Electrochimica Acta* 39.11-12 (1994), pp. 1833–1839.

[2] Y. Hori, H. Konishi, T. Futamura, A. Murata, O. Koga, H. Sakurai, and K. Oguma. ““Deactivation of copper electrode” in electrochemical reduction of CO2”. In: *Electrochimica acta* 50.27 (2005), pp. 5354–5369.

[3] S. Nitopi, E. Bertheussen, S. B. Scott, X. Liu, A. K. Engstfeld, S. Horch, B. Seger, I. E. Stephens, K. Chan, C. Hahn, *et al.* “Progress and perspectives of electrochemical CO2 reduction on copper in aqueous electrolyte”. In: *Chemical reviews* 119.12 (2019), pp. 7610–7672.

[4] D. Karapinar, C. E. Creissen, J. G. Rivera de la Cruz, M. W. Schreiber, and M. Fontecave. “Electrochemical CO2 reduction to ethanol with copper-based catalysts”. In: *ACS Energy Letters* 6.2 (2021), pp. 694–706.

[5] C. M. Gabardo, C. P. O’Brien, J. P. Edwards, C. McCallum, Y. Xu, C.-T. Dinh, J. Li, E. H. Sargent, and D. Sinton. “Continuous carbon dioxide electroreduction to concentrated multi-carbon products using a membrane electrode assembly”. In: *Joule* 3.11 (2019), pp. 2777–2791.

[6] C.-T. Dinh, T. Burdyny, M. G. Kibria, A. Seifitokaldani, C. M. Gabardo, F. P. García de Arquer, A. Kiani, J. P. Edwards, P. De Luna, O. S. Bushuyev, *et al.* “CO2 electroreduction to ethylene via hydroxide-mediated copper catalysis at an abrupt interface”. In: *Science* 360.6390 (2018), pp. 783–787.

[7] F. S. Roberts, K. P. Kuhl, and A. Nilsson. “High selectivity for ethylene from carbon dioxide reduction over copper nanocube electrocatalysts”. In: *Angewandte Chemie* 127.17 (2015), pp. 5268–5271.

[8] T. N. Nguyen and C.-T. Dinh. “Gas diffusion electrode design for electrochemical carbon dioxide reduction”. In: *Chemical Society Reviews* 49.21 (2020), pp. 7488–7504.

[9] E. W. Lees, B. A. Mowbray, F. G. Parlane, and C. P. Berlinguette. “Gas diffusion electrodes and membranes for CO2 reduction electrolysers”. In: *Nature Reviews Materials* 7.1 (2022), pp. 55–64.

[10] D. Wakerley, S. Lamaison, J. Wicks, A. Clemens, J. Feaster, D. Corral, S. A. Jaffer, A. Sarkar, M. Fontecave, E. B. Duoss, *et al.* “Gas diffusion electrodes, reactor designs and key metrics of low-temperature CO2 electrolysers”. In: *Nature Energy* 7.2 (2022), pp. 130–143.

[11] S. Ma, P. J. Kenis, *et al.* “Electrochemical conversion of CO2 to useful chemicals: current status, remaining challenges, and future opportunities”. In: *Current Opinion in Chemical Engineering* 2.2 (2013), pp. 191–199.

[12] K. Liu, W. A. Smith, and T. Burdyny. “Introductory guide to assembling and operating gas diffusion electrodes for electrochemical CO2 reduction”. In: *ACS energy letters* 4.3 (2019), pp. 639–643.

[13] T. Burdyny and W. A. Smith. “CO 2 reduction on gas-diffusion electrodes and why catalytic performance must be assessed at commercially-relevant conditions”. In: *Energy & Environmental Science* 12.5 (2019), pp. 1442–1453.

[14] M. Abdinejad, E. Irtem, A. Farzi, M. Sassenburg, S. **Subramanian**, H.-P. Iglesias van Montfort, D. Ripepi, M. Li, J. Middelkoop, A. Seifitokaldani, *et al.* “CO_2 Electrolysis via Surface-Engineering Electrografted Pyridines on Silver Catalysts”. In: *ACS catalysis* 12.13 (2022), pp. 7862–7876.

[15] E. Jeng and F. Jiao. “Investigation of CO 2 single-pass conversion in a flow electrolyzer”. In: *Reaction Chemistry & Engineering* 5.9 (2020), pp. 1768–1775.

[16] J. A. Rabinowitz and M. W. Kanan. “The future of low-temperature carbon dioxide electrolysis depends on solving one basic problem”. In: *Nature Communications* 11.1 (2020), p. 5231.

[17] E. R. Cofell, U. O. Nwabara, S. S. Bhargava, D. E. Henckel, and P. J. Kenis. “Investigation of electrolyte-dependent carbonate formation on gas diffusion electrodes for CO2 electrolysis”. In: *ACS Applied Materials & Interfaces* 13.13 (2021), pp. 15132–15142.

[18] D. G. Wheeler, B. A. Mowbray, A. Reyes, F. Habibzadeh, J. He, and C. P. Berlinguette. “Quantification of water transport in a CO 2 electrolyzer”. In: *Energy & Environmental Science* 13.12 (2020), pp. 5126–5134.

[19] J. E. Huang, F. Li, A. Ozden, A. Sedighian Rasouli, F. P. García de Arquer, S. Liu, S. Zhang, M. Luo, X. Wang, Y. Lum, *et al.* “CO2 electrolysis to multicarbon products in strong acid”. In: *Science* 372.6546 (2021), pp. 1074–1078.

[20] K. Yang, M. Li, S. **Subramanian**, M. A. Blommaert, W. A. Smith, and T. Burdyny. “Cation-driven increases of CO_2 utilization in a bipolar membrane electrode assembly for CO_2 electrolysis”. In: *ACS Energy Letters* 6.12 (2021), pp. 4291–4298.

[21] C. P. O’Brien, R. K. Miao, S. Liu, Y. Xu, G. Lee, A. Robb, J. E. Huang, K. Xie, K. Bertens, C. M. Gabardo, *et al.* “Single pass CO2 conversion exceeding 85% in the electrosynthesis of multicarbon products via local CO2 regeneration”. In: *ACS Energy Letters* 6.8 (2021), pp. 2952–2959.

[22] H.-P. Iglesias van Montfort and T. Burdyny. “Mapping Spatial and Temporal Electrochemical Activity of Water and CO2 Electrolysis on Gas-Diffusion Electrodes Using Infrared Thermography”. In: *ACS Energy Letters* 7.8 (2022), pp. 2410–2419.

[23] T. Zhang, Z. Li, J. Zhang, and J. Wu. “Enhance CO2-to-C2+ products yield through spatial management of CO transport in Cu/ZnO tandem electrodes”. In: *Journal of catalysis* 387 (2020), pp. 163–169.

[24] C. Kim, J. C. Bui, X. Luo, J. K. Cooper, A. Kusoglu, A. Z. Weber, and A. T. Bell. “Tailored catalyst microenvironments for CO2 electroreduction to multicarbon products on copper using bilayer ionomer coatings”. In: *Nature Energy* 6.11 (2021), pp. 1026–1034.

[25] B. Cao, F.-Z. Li, and J. Gu. “Designing Cu-based tandem catalysts for CO2 electroreduction based on mass transport of CO intermediate”. In: *ACS Catalysis* 12.15 (2022), pp. 9735–9752.

[26] X. Li and I. Sabir. “Review of bipolar plates in PEM fuel cells: Flow-field designs”. In: *International journal of hydrogen energy* 30.4 (2005), pp. 359–371.

[27] A. C. Olesen, S. H. Frensch, and S. K. Kær. “Towards uniformly distributed heat, mass and charge: A flow field design study for high pressure and high current density operation of PEM electrolysis cells”. In: *Electrochimica acta* 293 (2019), pp. 476–495.

[28] C. Wang, Q. Zhang, S. Shen, X. Yan, F. Zhu, X. Cheng, and J. Zhang. “The respective effect of under-rib convection and pressure drop of flow fields on the performance of PEM fuel cells”. In: *Scientific Reports* 7.1 (2017), p. 43447.

[29] D. Jeon, S. Greenway, S. Shimpalee, and J. Van Zee. “The effect of serpentine flow-field designs on PEM fuel cell performance”. In: *International journal of hydrogen energy* 33.3 (2008), pp. 1052–1066.

[30] Q. Ye, T. Zhao, and C. Xu. “The role of under-rib convection in mass transport of methanol through the serpentine flow field and its neighboring porous layer in a DMFC”. In: *Electrochimica Acta* 51.25 (2006), pp. 5420–5429.

[31] S. Toghyani, E. Afshari, E. Baniasadi, and S. Atyabi. “Thermal and electrochemical analysis of different flow field patterns in a PEM electrolyzer”. In: *Electrochimica acta* 267 (2018), pp. 234–245.

[32] J. S. Yi and T. Van Nguyen. “Multicomponent transport in porous electrodes of proton exchange membrane fuel cells using the interdigitated gas distributors”. In: *Journal of the electrochemical society* 146.1 (1999), p. 38.

[33] S. **Subramanian**, J. Middelkoop, and T. Burdyny. “Spatial reactant distribution in CO_2 electrolysis: balancing CO 2 utilization and faradaic efficiency”. In: *Sustainable Energy & Fuels* 5.23 (2021), pp. 6040–6048.

[34] G. O. Larrazábal, P. Strøm-Hansen, J. P. Heli, K. Zeiter, K. T. Therkildsen, I. Chorkendorff, and B. Seger. “Analysis of mass flows and membrane cross-over in CO2 reduction at high current densities in an MEA-type electrolyzer”. In: *ACS applied materials & interfaces* 11.44 (2019), pp. 41281–41288.

[35] C. M. Gabardo, A. Seifitokaldani, J. P. Edwards, C.-T. Dinh, T. Burdyny, M. G. Kibria, C. P. O’Brien, E. H. Sargent, and D. Sinton. “Combined high alkalinity and pressurization enable efficient CO 2 electroreduction to CO”. In: *Energy & Environmental Science* 11.9 (2018), pp. 2531–2539.

[36] M.-Y. Lee, S. Ringe, H. Kim, S. Kang, and Y. Kwon. "Electric field mediated selectivity switching of electrochemical CO2 reduction from formate to CO on carbon supported Sn". In: *ACS Energy Letters* 5.9 (2020), pp. 2987–2994.

[37] D. Bohra, I. Ledezma-Yanez, G. Li, W. de Jong, E. A. Pidko, and W. A. Smith. "Lateral adsorbate interactions inhibit HCOO- while promoting CO selectivity for CO2 electrocatalysis on silver". In: *Angewandte Chemie* 131.5 (2019), pp. 1359–1363.

[38] P. K. Sow, Z. Lu, H. Talebian, L. Damron, and W. Mérida. "Double layer capacitance measurements to characterize the water intrusion into porous materials". In: *The Journal of Physical Chemistry C* 120.43 (2016), pp. 24794–24802.

[39] K. Yang, R. Kas, W. A. Smith, and T. Burdyny. "Role of the carbon-based gas diffusion layer on flooding in a gas diffusion electrode cell for electrochemical CO2 reduction". In: *ACS Energy Letters* 6.1 (2020), pp. 33–40.

[40] A. Q. Fenwick, A. J. Welch, X. Li, I. Sullivan, J. S. DuChene, C. Xiang, and H. A. Atwater. "Probing the catalytically active region in a nanoporous gold gas diffusion electrode for highly selective carbon dioxide reduction". In: *ACS Energy Letters* 7.2 (2022), pp. 871–879.

[41] L. Xing, Y. Xu, Ž. Penga, Q. Xu, H. Su, W. Shi, and F. Barbir. "A novel flow field with controllable pressure gradient to enhance mass transport and water removal of PEM fuel cells". In: *AIChE Journal* 66.6 (2020), e16957.

[42] M. Rahimi-Esbo, A. Ranjbar, A. Ramiar, E. Alizadeh, and M. Aghaee. "Improving PEM fuel cell performance and effective water removal by using a novel gas flow field". In: *international journal of hydrogen energy* 41.4 (2016), pp. 3023–3037.

[43] J. S. Yi, J. D. Yang, and C. King. "Water management along the flow channels of PEM fuel cells". In: *AIChE journal* 50.10 (2004), pp. 2594–2603.

[44] D. Spernjak, A. K. Prasad, and S. G. Advani. "In situ comparison of water content and dynamics in parallel, single-serpentine, and interdigitated flow fields of polymer electrolyte membrane fuel cells". In: *Journal of Power Sources* 195.11 (2010), pp. 3553–3568.

[45] M. A. Blommaert, D. Aili, R. A. Tufa, Q. Li, W. A. Smith, and D. A. Vermaas. "Insights and challenges for applying bipolar membranes in advanced electrochemical energy systems". In: *ACS Energy Letters* 6.7 (2021), pp. 2539–2548.

[46] Y. Kong, H. Hu, M. Liu, Y. Hou, V. Kolivoška, S. Vesztergom, and P. Broekmann. "Visualisation and quantification of flooding phenomena in gas diffusion electrodes used for electrochemical CO2 reduction: A combined EDX/ICP–MS approach". In: *Journal of Catalysis* 408 (2022), pp. 1–8.

[47] A. B. Moss, S. Garg, M. Mirolo, C. A. G. Rodriguez, R. Ilvonen, I. Chorkendorff, J. Drnec, and B. Seger. “In operando investigations of oscillatory water and carbonate effects in MEA-based CO2 electrolysis devices”. In: *Joule* 7.2 (2023), pp. 350–365.

5

CO RESIDENCE TIME MODULATES C_{2+} FORMATION RATES IN A COPPER BASED ZERO-GAP CO_2 ELECTROLYZER

Science is what you know, philosophy is what you don't know.

\- Bertrand Russell

Carbon dioxide (CO_2) electrolysis on copper (Cu) catalysts has attracted interest for its direct production of C_{2+} feedstocks. Using the knowledge that CO_2 reduction on copper is primarily a tandem reaction of CO_2 to CO and CO to C_{2+} products, we show that modulating CO concentrations within the liquid catalyst layer allows for C_{2+} selectivity of >80% at 200 mAcm^{-2} over broad conversion conditions. The importance of CO pooling is demonstrated through residence time distribution curves, varying flow fields (serpentine/parallel/interdigitated), and flow rate. While serpentine flow fields require high conversions to limit CO selectivity and maximize C_{2+} selectivity, the longer CO residence times of parallel flow fields reach similar selectivity over broad flow rates. Critically, we show that parts of the catalyst area are predominantly reducing CO instead of CO_2 as supported by CO reduction experiments, transport modelling, and achieving a CO_2 utilization efficiency greater than the theoretical limit of 25% for C_{2+} products.

This chapter has been submitted as a manuscript (Under review) titled "CO residence time modulates multi-carbon formation rates in a zero-gap Cu based CO2 electrolyzer" by Siddhartha Subramanian, Jesse Kok, Pratik Gholkar, Asvin Sajeev Kumar, Hugo-Pieter Iglesias van Montfort, Ruud Kortlever, Atsushi Urakawa, Bernard Dam and Thomas Burdyny.

5.1. INTRODUCTION

Electrochemical CO_2 reduction reaction (CO_2RR) using copper (Cu) based catalysts are attractive due to copper's ability to produce hydrocarbons and oxygenates [1–7]. As a result, extensive efforts have gone into unravelling the reaction pathways and intermediates in both H-cell and gas diffusion electrode (GDE) cell architectures to understand and improve, what enables such broad C1 and C2 product spectrums[8–13]. These studies have shown that copper's unique ability to moderately bind carbon monoxide (CO) facilitates the coupling of two CO species[14–19]. Critically, the coupling of CO-species has been shown to occur through both surface dimerization of two adsorbed CO-species and tandem reactions where CO_2 is first converted to CO, desorbs into the aqueous environment as CO(aq). A recent study has also shown the presence of two distinct active sites on Cu for CO_2 to CO conversion and CO to C_{2+} conversion[20]. Copper is then not simply a unique CO_2/CO to C_{2+} catalyst, but an excellent CO_2 to CO catalyst.

A number of CO_2RR experiments performed in fully-aqueous reaction environments have sought to understand the effect of CO(aq) on multi-carbon product formation[21–23] through a variety of control experiments and modelling. The importance of local CO(aq) concentration has further motivated tandem catalyst and bimetallic systems where one catalyst is included for CO_2 to CO conversion, and a copper catalyst further facilitates CO_2/CO reduction. A few studies for instance have shown that such spatial variations can be used to tune CO coverage over a Cu catalyst to achieve higher partial current densities of C_{2+} products[24–26]. While this premise is attractive and shows increased oxygenate production rates as a result, these fully tandem systems commonly produce CO in excess amounts except at very precise flow rates and current densities. We conclude that a primary reason for this is because copper itself already reaches excessive CO(aq) concentrations during CO_2RR, particularly at elevated current densities. We then posit that the need for local CO regulation can also be met by further understanding and modulating the residence times of CO(aq) in copper-based systems.

Suitable platforms to examine local CO regulation are zero gap membrane electrode assemblies (MEA) using anion exchange membranes due to their elevated reaction rates (>100 mA/cm^2), low cell voltages and ability to maintain a favourable alkaline environment around the catalyst surface which reduces by-product H_2 production[27–29]. A notable consequence of these flow-based systems is the spatial variation in the concentration of reactants (CO_2, CO and H_2O) and products (CO, C_2H_4) within the catalyst layer as flow rate and current density are varied[30]. These spatial variations will impact the localized Faradaic efficiency, but cannot be resolved through common measurements which give averaged Faradaic efficiency due to external product measurement.

In this work, we study the influence of CO residence time on C_{2+} production rates for a Cu catalyst coated on carbon gas-diffusion layer in an alkaline MEA cell. We use pulse and negative tracer gases to generate residence time distribution curves under various flow rate conditions and flow field patterns (serpentine, parallel and interdigitated) using ex-situ mass spectrometry. When contrasting these findings with electrochemical data we are able to infer both local and spatial phenomena related to CO concentrations throughout the MEA cell. We find that C_{2+} production rates increase at decreased CO_2 flowrates because of near-complete CO consumption, achieving a maximum selectivity of 84% at 200 mA/cm^2. We further demonstrate how modulating CO concentrations via the choice of flow rate and flow field can enable regions of greater CO reduction instead of CO_2 reduction, allowing for elevated CO_2 utilization efficiency.

5.2. RESULTS AND DISCUSSION

Within a MEA CO_2 electrolyzer, CO and other products are produced within the liquid-immersed catalyst layer. These products can then either diffuse across a gas-liquid interface and through the gas diffusion layer (GDL) into the gas channel, or in the case of CO they can further be reduced on the catalyst (Supplementary Figure 5.1). To better understand the statistical amount of time that products reside within the liquid layer, we performed residence time distribution experiments of an ex-situ CO_2 electrolysis cell.

As illustrated in Figure 5.1, a non-reactive tracer gas of 5% CO and 95% He is injected into an assembled electrolyzer, and a time-resolved output signal of CO is measured by a mass spectrometer (See Supplementary Figure 5.7). By using defined input profiles of the tracer gas such as a pulse or negative tracers, the profile and delay of the output signal, known as a residence time distribution (RTD) curve, will give us information about the convective and diffusive properties of the MEA electrolyzer. Inside a CO_2 electrolyzer employing a gas diffusion electrode, however, contributions from the gas flow channel, the GDE and the liquid filled catalyst layer all affect the RTD and the dominant transport factor needs to be determined.

In this regard, previous studies from fuel cells have shown that pulse RTD tests predominantly show the gas flow field channel characteristics as gases pass through the system components (see Figure 5.1a center)[31–33]. In contrast, a negative tracer test saturates the entirety of the system for longer periods of time and provides information on the time required for gases to leave all parts of the cell[34]. A negative tracer then gives a good perspective of products that are formed in the liquid phase leaving as the gas channel partial pressure is decreased[35]. Here, the eventual release of the tracer is then maximized at the tail.

We began our non-electrochemical RTD tests by first examining the importance of the liquid layer in an MEA system as liquid diffusion and liquid-to-gas diffusion of CO are expected to be the largest transport barriers. For the experiments we used the most common flow field pattern (FFP), a serpentine channel which has a single fluid flow path from the inlet to outlet, creating a significant pressure drop in the reactor. There are then two scenarios in Figure 5.1b. For the non-wetted case, we assembled the MEA cell as usual but without applying a potential, which means that no water wets the anion exchange membrane or is present on the cathode GDL. For the wetted case, we used a porous Zirfon membrane which is wetted by the anolyte flow. When we compare a 30 s pulse RTD test for the two cases, we see a stark difference in the RTD curves (Figure 1c). For the non-wetted case, we see a CO RTD profile almost identical to the pulse input with a mean residence time of 28 s, whereas the wetted case shows a substantially longer mean residence time of 118 s. This control experiment confirms the impact of the water layer on transport properties and confirms its importance in future tests.

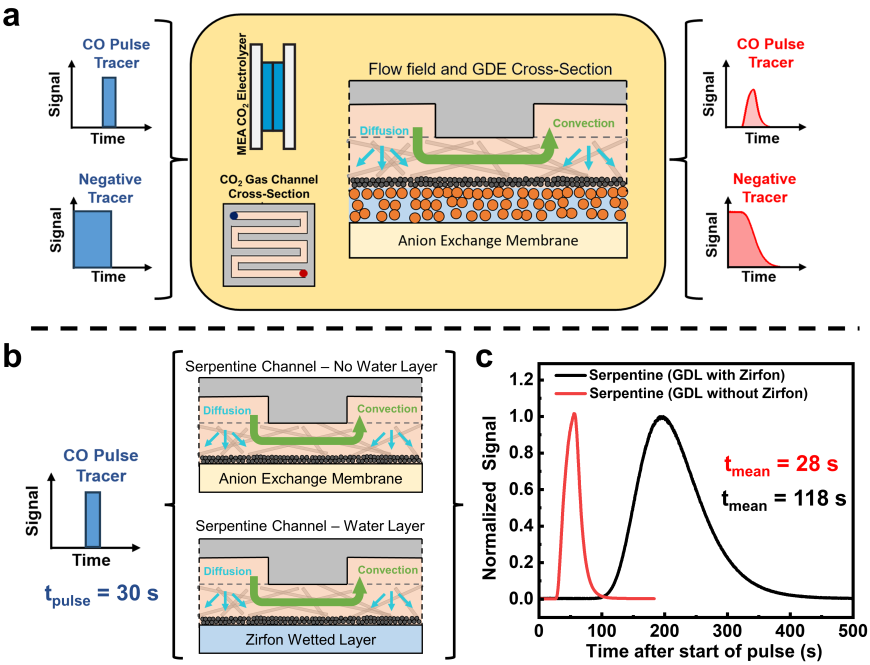

Figure 5.1 : (a) Schematic of residence time distribution (RTD) curves measurements in the zero gap CO_2 electrolyzer using carbon monoxide as a tracer gas. (b) Overview of control RTD curves measurement for a 30 s carbon monoxide tracer pulse for two different zero gap configurations at 10 standard cubic centimeters per minute. The top configuration uses a non-wetted anion exchange membrane adjacent to the gas-diffusion layer. The bottom configuration uses a wetted Zirfon membrane to provide a water layer next to the gas-diffusion layer. (c) RTD curves for the non-wetted and wetted configurations showing the increase in residence time due to a water layer.

We then performed pulse and negative RTD measurements on the Zirfon wetted system for varied inlet flow rates (Figure 2a, 2b). Here a clear difference is observed between a 10 sccm flow (representative of a high CO_2 conversion scenario) and 50 sccm (a low CO_2 conversion scenario). Consequently, the mean residence time for the tracer at 10 sccm was 118 s, higher than at 50 sccm (110 s). If we relate this finding to a CO_2 electrolyzer in operation, it indicates that a CO molecule in either the liquid layer or the gas channel will on average reside there for 8 s longer at 10 sccm than 50 sccm.

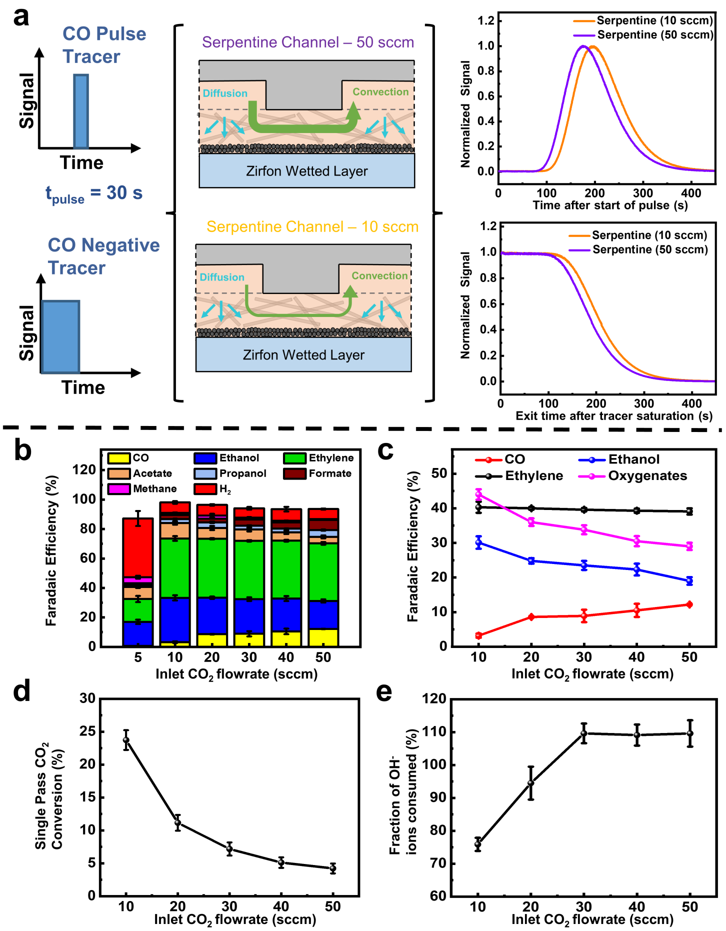

Figure 5.2 : (a) Non-electrochemical pulse RTD results for a serpentine flow field with 30s CO tracer flowrates of 10 and 50 SCCM. (b) Faradaic efficiency of products obtained from CO_2RR on Cu catalyst in the MEA cell under flow rates ranging from 5 SCCM to 50 SCCM at a geometric current density of 200 mA/cm^2. (c) Comparison of CO and C_{2+} product selectivity at 200 mA/cm^2. (d) Single pass conversion of CO_2 to C_{2+} products at the studied inlet flowrates. (e) Fraction of OH^- ions consumed to CO_2 during the reaction, estimated using carbon balance over the system. Error bars represent the mean and standard deviation of triplicate experiments.

To contrast these non-electrochemical RTD measurements with electrochemical data, we performed CO_2 electrolysis experiments in an MEA cell using a Ni foam anode, Cu sputtered carbon GDE (5 cm^2) and humidified CO_2 as the reactant. The measurement techniques and instrumentation are shown in Supplementary Figure S13. For our tests, we used a fixed geometric current density of 200 mA/cm^2 with CO_2 fed at various flowrates ranging from low to high CO_2 conversion conditions.

As shown in Figure 5.2b and 5.2c, we find that the product distribution varies as CO_2 flowrates decrease from 50 sccm to 5 sccm. Notably, we see a decrease in the Faradaic efficiency (FE) of CO from 12.6% at 50 sccm to just 3% at 10 sccm. In contrast, the FE of ethanol increases substantially from 20.3% at 50 sccm to 30.8% at 10 sccm. The shift is even more stark when observing the oxygenate (ethanol + acetate) trend in Figure 5.2c. In particular, the product spectrum where oxygenates outcompete ethylene FE is more indicative of CO RR on copper than that of CO_2RR[36, 37]. When coupled to the non-electrochemical RTD data it implies that the production rate of CO in both the 10 and 50 sccm cases may actually be similar, but the CO produced in the 10 sccm case remains longer in the gas channel and liquid layer such that it is further reduced, providing a more oxygenated product spectrum. Interestingly, rates of ethylene production remain unchanged (FE 40%) across all flow rates, implying that any decrease in CO(aq) predominantly contributed to ethanol product pathways (Equation S38 in Supplementary Notes)[38]. When flowrates were further decreased (5 sccm), competing HER took over (FE H_2 of 40%) due to mass transport limitations of CO_2 reaching the entire 5 cm^2 Cu GDE (Figure 5.2c). Here, however, the oxygenate to ethylene trend continues.

A single pass conversion efficiency of 24% (Figure 5.2d) and a maximum C_{2+} selectivity of 84% (j_{C2+} of 168 mA/cm^2) are then achieved at 10 sccm, due to the higher residence time of CO in the reactor. A higher residence time ensures that there is sufficient time for dimerization of two *CO molecules, thereby achieving a CO utilization of 87.6% for C_{2+} production at 10 sccm (See Equations S28-S30 in Supplementary Notes and Supplementary Table 2). Notably then we can say that the highest combined Faradaic efficiency and single-pass conversion at a fixed current density both occur at low flow rates for a serpentine channel. At a higher flowrate of 50 sccm however, the C_{2+} selectivity drops to 65% with a single-pass conversion of only 4%. Additionally, a very low stoichiometric CO_2 excess of 1.13 (See Supplementary Table 2) is obtained at 10 sccm, which is beneficial for achieving product rich gas streams and reducing downstream gas separation costs as shown in a recent study[39].

Lastly, for the serpentine results, we found during our experiments that we lost less CO_2 to OH^- interactions than expected at 10 and 20 sccm. In particular, only 75% of OH^- ions generated at the cathode are converted to CO_3^{2-}/HCO_3^- due to buffer reactions with CO_2 at 10 sccm, whereas all OH^- is reacted above 30 sccm (Fig. 2e). Assuming that these 75% of OH^- ions reacting with CO_2 are converted to CO_3^{2-} ions at these higher reaction rates (local pH > 12), this would mean that the ions transported across the AEM (towards the anode) is a mixture of CO_3^{2-} and OH^- ions. Typically, we would expect such a result only in CO_2 depleted cases where high H_2 FE's are seen. However, the total CO_2RR FE are 92% and H_2 FE is only 7%. This finding implies that we have regions in the reactor where reactions can proceed to

C_{2+} products without parasitic reactions of CO_2 and OH^- ions. We then conclude that regions of our 5cm^2 electrode are CO_2 depleted but not CO depleted. A portion of catalyst performing CO electrolysis then also explains the constant ethylene selectivity observed across various flowrates (Figure 5.2c) since selectivity shift to oxygenates rather than ethylene occurs when moving from CO_2 to CO electrolysis [40, 41].

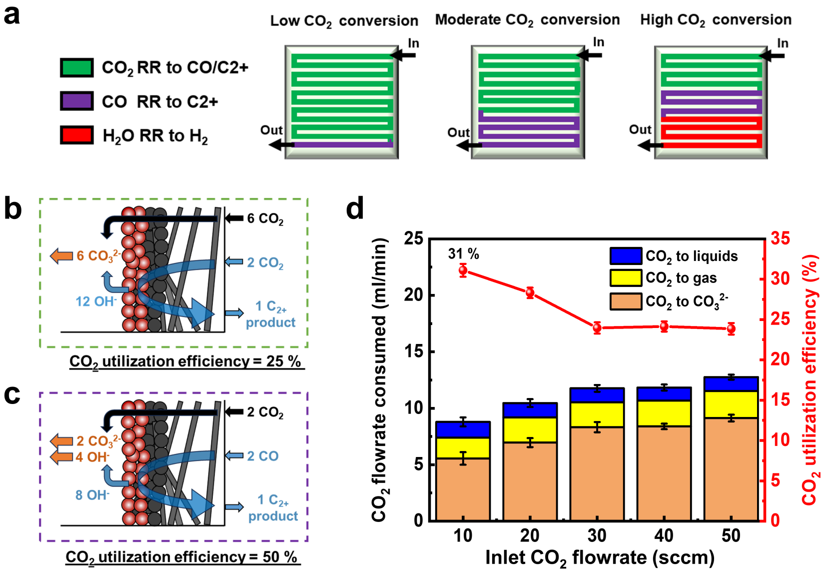

Figure 5.3 : (a) Schematic of the predicted dominant reactions occurring along a serpentine flow field during CO_2RR under varying CO_2 conversion regimes. (b) Schematic depicting the theoretical CO_2 utilization efficiency of 25% for 100% Faradaic production of ethylene and ethanol from CO_2. (c) Schematic depicting how CO_2 deplete regions with access to by-product CO can exceed the theoretical CO_2 utilization efficiency. Shown here is an example when it can reach 50% (d) A carbon balance of the consumed input CO_2 in the serpentine MEA tests system and CO_2 utilization efficiencies at the studied inlet flowrates.

Using the above findings, we can then predict the dominant electrochemical reaction occurring along the flow channel length for low, moderate, and high CO_2 conversion cases (Figure 5.3a). In green regions the primary reactant is CO_2, whereas in purple regions, CO is more in abundance than CO_2. As discussed elsewhere [42], the maximum CO_2 utilization efficiency to ethylene and ethanol products for the green region is 25% (Figure 5.3b). However, the purple region performing primarily CORR has no such limitation as there may not be enough CO_2 present to react with the formed OH^-(Figure 5.3c). Indeed when we calculate the CO_2 utilization efficiency across various flow rates, we reach a value of 31% (Figure 5.3d), breaking the limit of 25% obtained for pure C_{2+} product formation when $CO_3{}^{2-}$ ions act as the sole charge carrier.

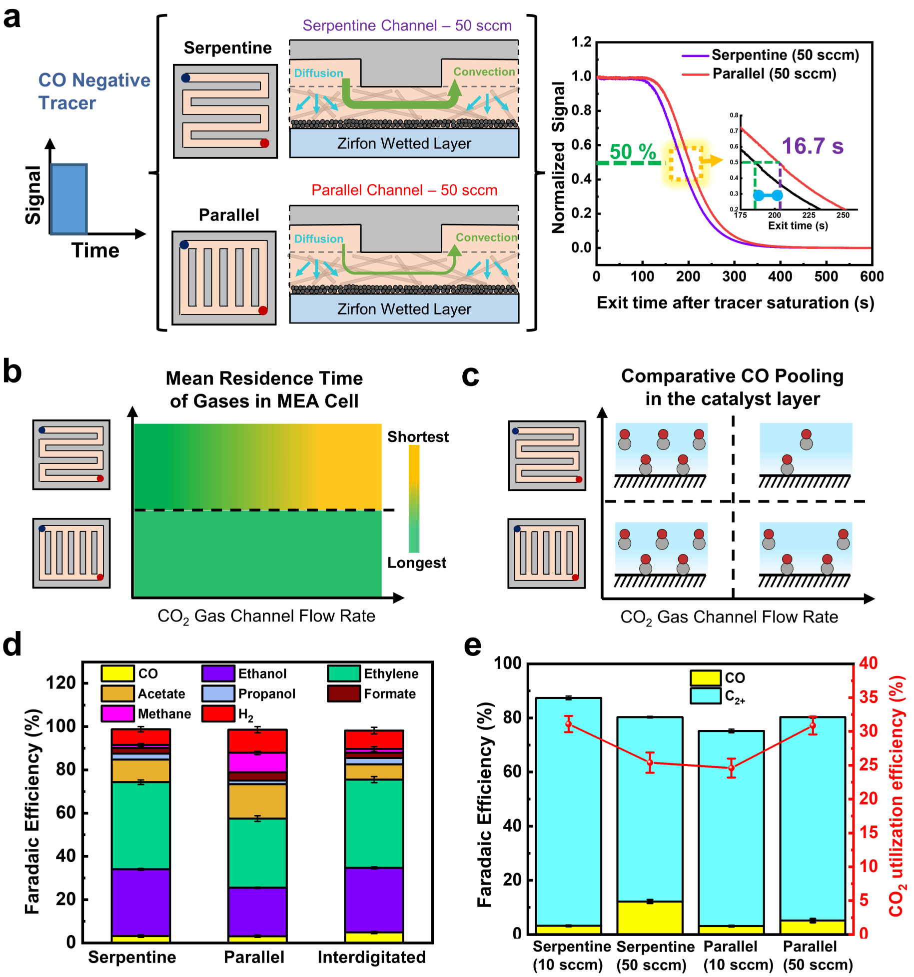

Figure 5.4 : (a) Non-electrochemical negative tracer RTD results for serpentine and parallel flow fields at tracer flowrates of 50 SCCM showing longer residence times for parallel flow fields as a result of lower convective forces. (b) A qualitative comparison of the RTD results as a function of flow rate and flow field. (c) A qualitative assessment of the CO pooling inside the catalyst layer during CO_2 electrolysis as a function of flow rate and flow field. (d) Faradaic efficiency of products obtained from CO_2RR in an MEA cell at 10 SCCM and 200 mA/cm^2 for serpentine, parallel and interdigitated flow fields. (e) Comparable CO and C_{2+} product selectivity for varied flow rates and flow fields. Inset (red line) shows the calculated CO_2 utilization efficiencies. Error bars represent the mean and standard deviation of triplicate experiments.

To further test the above conclusion regarding CO residence times, we performed further RTD and electrochemical tests on parallel flow fields. In contrast to serpentine channels, a parallel FFP has channels divided into parallel paths with a very low pressure drop between the inlet and outlet[43]. Mass transport through the GDE is then dominated predominantly by diffusion. Due to fundamental differences in GDE transport between FFP's, we performed negative tracer RTD measurements to compare the release of gases from each system (Figure 5.4a and Supplementary Figure 5.11). Again, all components of our standard electrochemical MEA cell were assembled except with a pretreated Zirfon membrane pressed against the carbon GDL to mimic the wetted catalyst in real CO_2RR conditions (See Supplementary Information for details).

Observing the normalized RTD curves in (Figure 5.4a), the negative tracer experiments show a large difference in the serpentine and parallel FFP curves at 50 sccm. Despite being at identical flow rates, there is 16.7 s delay for the tracer to exit the reactor using a parallel FFP in comparison to the serpentine FFP, illustrating an increased residence time of the tracer gas inside the reactor. The higher residence time shows that the use of a parallel FFP creates the likelihood of higher reactant pooling in the wetted regions of the GDL surface. These results can be anticipated as the parallel flow field has lower channel velocities than the serpentine channel (Supplementary Table 4), which impacts concentration gradients between the gas channel and liquid layer, thus slowing gas removal from the liquid.

By combining the flow rate and flow field RTD data together we can compose the qualitative graph in Figure 5.4b. Here we see that the serpentine channel can have long or short residence times depending on the flow rate inputted. Conversely, the parallel channel has a lower sensitivity to flow rate as the fluid velocity is always at a substantially lower value than the serpentine channel at equivalent volumetric rates. These conclusions then lead to a representative image of CO pooling during electrochemical CO_2 reduction for each of the different cases as shown in Figure 5.4c.

We then performed CO_2RR using varied gas flow field patterns (FFP) at the cathode Figure 5.4d shows the product distribution using all three different FFP's at 200 mA/cm^2 and a CO_2 inlet flowrate of 10 sccm. While all three FFPs show a similar selectivity of CO (3-4%), there were differences in the individual C_{2+} product distribution. For both the serpentine and interdigitated FFPs, FE of ethylene (40%) and oxygenates (40%) remain quite similar, achieving a C_{2+} selectivity of 82-84% with a low CH_4 (FE 1%) and H2 (FE 8%). However, when a parallel FFP is used at the cathode, the FE of acetate doubles to 16% and CH_4 increases to 9%. This comes at the expense of decreased ethylene (FE 32%) and ethanol (FE 22%), leading to a drop in total C_{2+} selectivity of 72% (Figure 5.3b). The selectivity switch from ethylene/ethanol to acetate for the parallel FFP suggests that a higher local alkalinity around the catalyst is more likely, due to CO_2 depletion within the GDE[44].

The higher CH_4 production also shows that an increased *H coverage (from $^*H_2O$) occurs within the catalyst layer due to depleted CO_2 in some parts of the catalyst layer. An increased *H coverage is plausible since CH_4 formation is well known to occur through a surface recombination of *CO and *H via a Langmuir-Hinshelwood mechanism[45]. Overall, the use of a parallel FFP at the cathode at 10 sccm results in decreased CO_2 access at some portions of the Cu catalyst layer and a subsequent increase in local alkalinity, producing higher CH_4 and acetate respectively. Previous studies on CO reduction on Cu have also attributed the increased acetate production to the abundance of OH^- ions, which leads to a higher local pH around the catalyst surface[46, 47].

Further, this depletion in CO_2 access for a parallel FFP, suggests that a significant portion of catalyst surface is predominantly used for electrolysis of CO (produced from CO_2) to C1 (methane) and C_{2+} products. Supporting this hypothesis are the results from our empirical numerical transport model which shows that about 18% of GDE has no CO2 access when a parallel FFP is used at the cathode (Supplementary Figure 12). The total C_{2+} selectivity is however lower (72%) for the parallel FFP due to depleted CO_2 and increased *H coverage as is evident from the increased CH_4 selectivity. This would then imply that, if excess CO_2 is fed into the system to ensure no mass transport limitations, the parallel FFP should maximize C_{2+} production due to the increased residence time of CO within the GDE as shown earlier (Figure 5.4a).

To assess some of the above statements, we operated the serpentine and parallel FFPs at 200 mA/cm^2 and at an excess CO_2 flowrate of 50 sccm to ensure sufficient CO_2 is available for both the cases to prevent CO_2-deplete regions. Interestingly, we find a switch in the product distribution, with a significantly higher C_{2+} selectivity for the parallel FFP (75.2%), compared to the serpentine case (68%). As shown in Fig. 4e, the FE of CO was then more than twice lower (5%) for the parallel FFP compared to the serpentine case (FE 12.6%). This increased CO utilization to C_{2+} products for the parallel FFP shows the benefit of an increased residence time within the GDE for dimerization of two CO molecules. A modified FFP taking the benefit of both the parallel FFP to achieve higher CO residence time and a serpentine FFP to increase under-rib convection might then be attractive to achieve both higher C_{2+} production and higher single pass conversion efficiencies. Such considerations however, are beyond the scope of this study.

The calculated CO utilization rate towards C_{2+} products then reached 83.6% for the parallel FFP (See Supplementary Table 5.2) at 50 sccm, significantly higher than 65% obtained for the serpentine case. Operating electrolyzers using a parallel FFP is then beneficial at higher flowrates, but comes at a cost of lower single pass conversion of CO_2 fed into the reactor. Recent studies have however shown that operating at lower single pass conversion efficiencies (5-10%) are sufficient since the energy required for gas separation is 100 times lower than the actual electrolyzer energy requirements[48]. Considering this aspect, a parallel FFP might be beneficial at higher and a broader range of flowrates due to its inherent ability to increase reactant residence time inside the liquid filled catalyst layer. In addition, a parallel FFP also benefits from a very low pressure drop in the reactor (Supplementary Table 5.4), which might be beneficial as CO_2 electrolyzers are scaled to larger areas (>100 cm^2).

5.3. CO ELECTROLYSIS RESULTS

While much of the work here showcased the influence of residence time of CO on C_{2+} production, the Faradaic efficiency results of individual C_2 products (ethylene, ethanol and acetate) also showed distinct trends. For instance, the use of a parallel FFP at the cathode produced the highest acetate (FE 15-16%) at both 10 and 50 sccm inlet flowrates, which was twice higher than the serpentine and interdigitated FFPs. We hypothesized that the local catalyst microenvironment, specifically the local alkalinity as a result of differences in CO_2 availability might be altered due to the FFP used, which may explain selectivity differences. We then performed CO electrolysis at 200 mA/cm^2.

Figure 5.5a shows the product distribution obtained from electrochemical CO reduction reaction (CORR) for the three FFPs. As the reactant feed is switched from CO_2 to CO, we see a clear selectivity switch from ethylene/ethanol to acetate for all the three FFP. Acetate production in these conditions is similar to existing CORR literature but it is interesting that the differences we observed in CO_2RR have mostly been removed here. When we consider that most of the CO_2RR differences for serpentine vs parallel channels are explained to be a result of CO pooling and tandem reactions, it then makes sense that we do not see a stark serpentine-parallel difference for CO electrolysis in Figure 5.5a where no products can be further reduced.

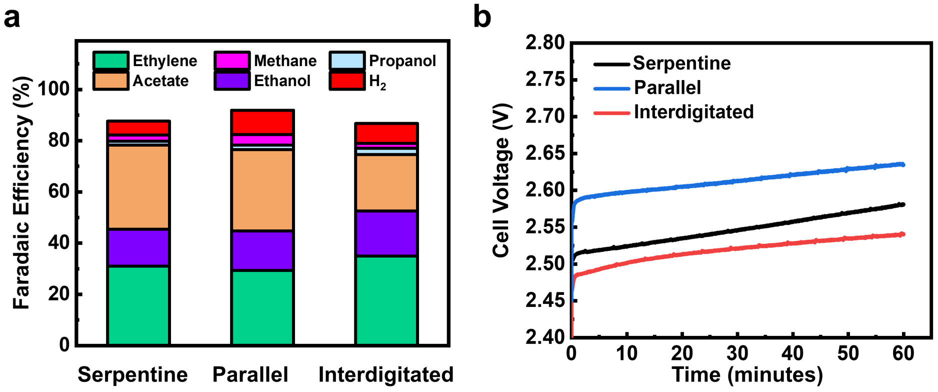

Figure 5.5:Product distribution from CO electroreduction for the three flow field patterns at a geometric current density of 200 mA/cm$_2$. (b) Cell voltages obtained CORR for the three FFP at 200 mA/cm$_2$.

The higher acetate production observed during this reactant switch from CO_2 to CO for all FFPs also suggests a stronger dependence of product distribution on local alkalinity around the catalyst layer. The concentration of local OH^- ions during CORR are more than one order of magnitude higher than for CO_2RR[44], where neutralization by buffering reactions with CO_2 occurs. It has been shown before that these abundant hydroxide ions react with the CH_2CO intermediates (Equation S40 in Supplementary Notes) relevant for ethylene and ethanol, leading to a switch in product towards acetate[49, 50]. A moderate interfacial pH, observed during CO_2RR (pH <12-13)[51] is then beneficial to avoid this switch from ethylene/ethanol to acetate. However, modulating interfacial pH in these catholyte free MEA cells at higher current densities is quite challenging, as this would require modifications either in the type of the ion exchange membrane used or ionomers[52] within the catalyst coated GDL.

This interplay of product formation rates highlight important implications for CO electrolysis in zero gap MEA electrolyzers. Although CORR is beneficial due to the absence of carbonate crossover and lower full cell voltages (Figure 5.5b), the findings here show that these advantages comes at the expense of lower ethylene and ethanol formation rates. In addition, the calculated full cell energy efficiency (Supplementary Table 7) for a combined ethylene and ethanol production from ECOR is similar (23.4%) to CO_2RR (29%), highlighting the main benefit of CORR lies in the long term operational stability, due to absence of carbonate formation at the cathode. Overall, this shows that CO_2 electrolysis still has potential for producing high rates of ethylene and ethanol if stability issues due to (bi) carbonate formation and Cu stability can be addressed as shown in recent studies[53, 54].

Finally, the major challenge that hinders commercialization of CO_2 electrolyzers using Cu based catalysts lies in the inability to selectively produce ethylene or ethanol with high selectivity (> 70%). Most studies have however shown that a combined 70-80% selectivity towards ethylene and ethanol can be obtained at industrially relevant current densities. While these branching pathways towards ethylene and ethanol cannot be well controlled as shown in a recent study[55], we posit here that researchers must look into a combined ethylene + ethanol selectivity as a performance metric. This is because, ethanol as a liquid product can be separated from the MEA reactor and further be used as a starting material to produce ethylene through catalytic dehydration reaction[56].

Importantly, the energy requirements for this ethanol dehydration reaction to ethylene (45 kJ/mol of ethylene) are two orders of magnitude lower than a CO_2 electrolyzer producing ethylene (2900 KJ/mol of CO_2)[57]. We then argue here that the research community should look into integrating catalytic dehydration of ethanol to ethylene as an additional process step to CO_2 electrolysis in order to make it energy efficient and industrially viable.

5.4. Conclusion

In conclusion, the residence time of CO in the liquid catalyst region greatly impacts product distribution from CO_2 electrolysis. Here we show that modulating CO residence time is possible with varied inlet flowrates and flow field patterns, and is an important consideration for both catalyst and system studies. We show that while both the interdigitated and serpentine flow patterns require higher single pass conversions to limit CO selectivity, a parallel flow pattern shows the highest C_{2+} selectivity at larger and a broader range of flowrates. Under lower flow conditions we also show that the electrolyzers begins to split into CO_2 and CO dominated regions, which has implications for selectivity, CO_2 utilization efficiencies, and local catalytic and component effects.

5.5. SUPPLEMENTARY INFORMATION

SCHEMATIC OF A CARBON GDE IN MEA CELL

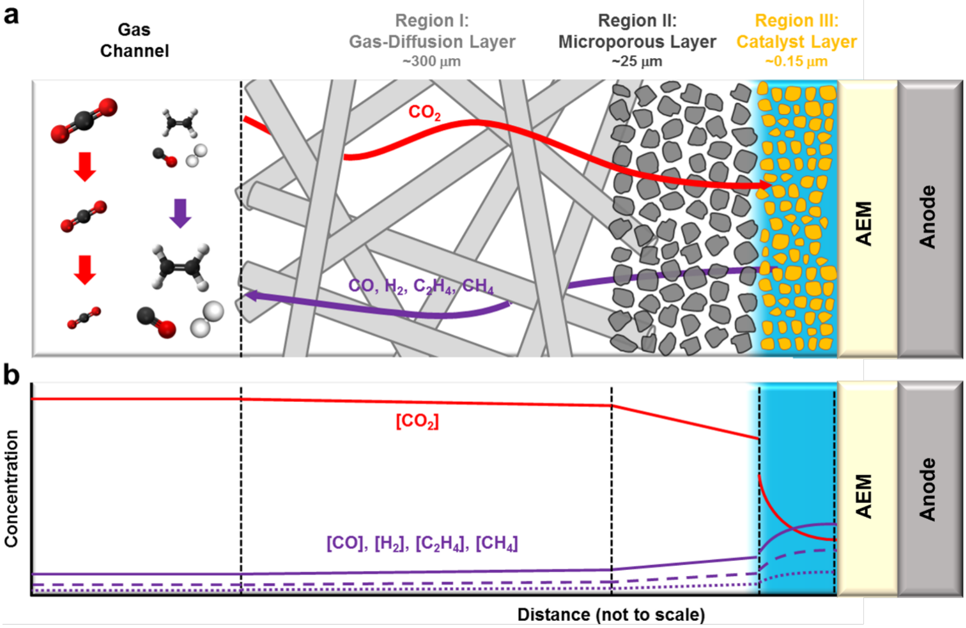

Figure 5.6 : Schematic of a gas diffusion electrode (GDE) architecture in an anion exchange MEA configuration. Shown here are the concentration gradients of various species inside the GDE.

5.5.1. RESIDENCE TIME DISTRIBUTION (RTD) MEASUREMENTS USING MASS SPECTROMETRY

RTD measurements were performed using a Omnistar Pfeiffer Vacuum mass spectrometer with a time resolution of 100 ms. The schematic of the tracer injection system is shown in Supplementary Figure 2. A pneumatic valve was used to switch the two gas streams, one containing the tracer (5% CO in He) and the other containing pure He gas. The check valve depending on the position, switches the gas streams either to the cathode side of the MEA cell or to the exhaust. A LabVIEW program was used to control the injection and turn off for a fixed duration. For the pulse tracer tests, the tracer was injected for 30 s. For the negative tracer tests, the tracer was injected until the reactor reached saturation and turned off thereafter to record the release of the tracer.

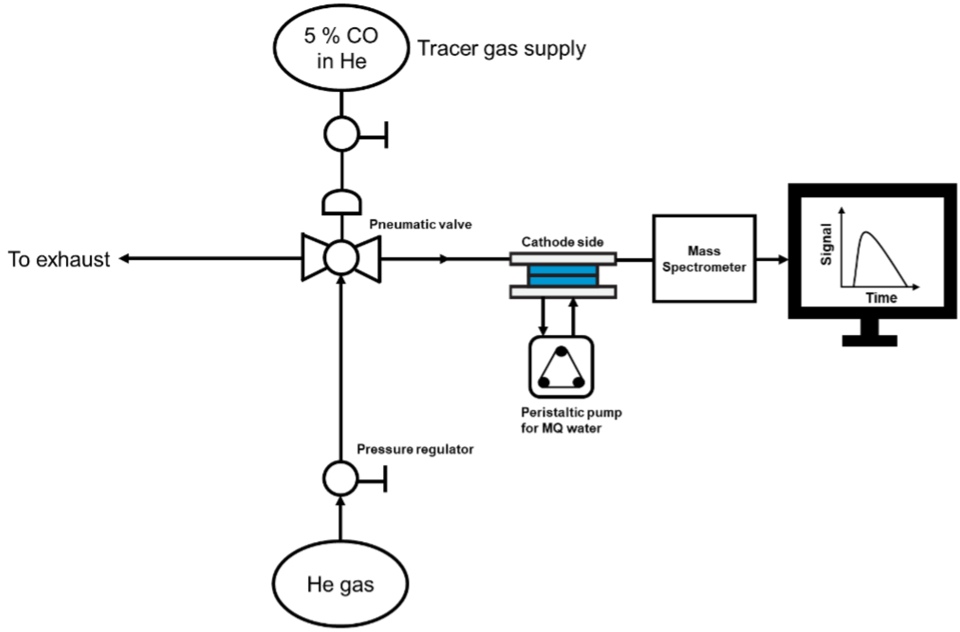

Figure 5.7 : Simplified process flow diagram of the RTD system used in the study.

All RTD tests were performed using commercially purchased carbon based GDL (Sigracet 39 BC) with a microporous layer. Two tests were performed to elucidate the differences between the dry and wetted MPL cases. In the first case, MEA cells were assembled similar to a CO_2 electrolyzer with carbon GDL, Sustainion AEM, Ni foam anode and the two gaskets for both sides. MQ water was constantly flowed at the anode compartment to keep the membrane wetted during RTD tests. At the cathode side, CO tracer was injected to monitor the RTD measurements. In the second type of test, a pretreated Zirfon membrane was pressed on top of the microporous layer side of the GDL inside the MEA cell (Supplementary Figure 5.8b). Since water was flowing at the other compartment (anode side on Ni foam), porous

Zirfon membrane was wetted and acted as a reservoir of water in contact with the carbon GDL at the cathode. This then mimicked a 'wetted catalyst layer' during real CO_2RR experiments. In both these tests, Ni foam and two gaskets (Silicone for Ni and PTFE for GDL) were used to maintain actual compression occurring in the CO_2 electrochemical tests. For all tests, a non-reactive tracer (5% CO in He gas) was used. Pulse and negative tracer tests were performed for varied inlet flowrates and two flow field patterns (serpentine and parallel).

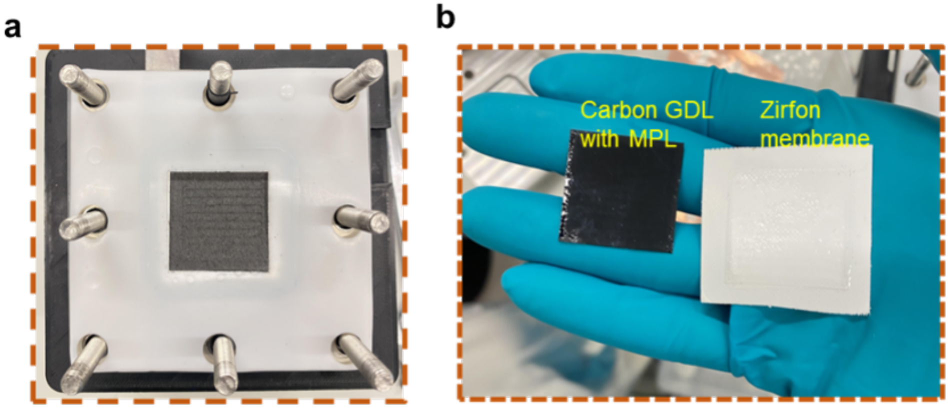

Figure 5.8 : (a) Images of Sigracet 39 BC carbon GDL and the MEA setup used in the RTD measurements. (b) Snapshots of MPL side of the carbon GDL and Zirfon membrane post RTD experiments.

CALCULATION OF MEAN RESIDENCE TIME

Mean residence time of the tracer inside the reactor was calculated for the pulse RTD tests for the 10 and 50 sccm flowrates. For the pulse RTD measurements, the RTD curves with the normalized tracer vs. time were first plotted. To eliminate the contribution from the tubing to the reactor, we performed RTD measurements without the MEA cell to measure the 'blank' test. Time taken for the tracer signal to exit during the blank test was then subtracted from the original MEA cell pulse RTD tests. From the resulting plot, the mean residence time was calculated using Equation 5.1.

$$\mathbf{t_{mean}} = \frac{\sum \mathbf{t_i\, C_i}}{\sum \mathbf{C_i}} \tag{5.1}$$

Here **t** represents the time, **C** is normalized tracer concentration, i represents the 'i^{th}' data point in the concentration vs time plot.

DIFFERENCES BETWEEN GAS AND LIQUID PHASE PULSE RTD MEASUREMENTS

Pulse RTD measurements performed with the non-wetted sigracet GDL (without Zirfon membranes) showed faster times for the tracer to exit the reactor. Supplementary Figure 5.9 shows the pulse RTD measurements for serpentine flow channel performed at 10 sccm with and without the Zirfon membrane in contact with the MPL side of GDL.

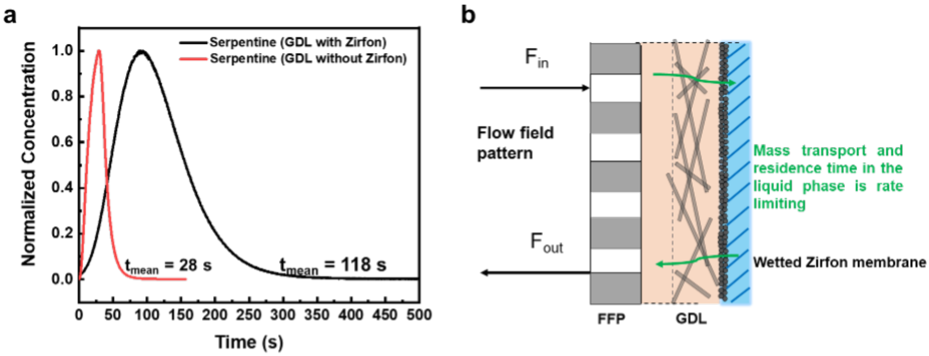

Figure 5.9 : (a) RTD pulse tracer output for an inlet flowrate of 10 sccm using serpentine flow field pattern. Black curve shows results for tests with Zirfon membrane placed on top of carbon GDL. Red curve shows output for carbon GDL without Zirfon membrane. (b) Schematic of the wetted zirfon membrane in contact with the GDL creating a reservoir of liquid where mass transport is rate limiting.

The mean residence time of the tracer in the first case without Zirfon membrane is only 28 s. Whereas, for the carbon GDL placed in contact with the Zirfon membrane, the calculated mean residence time comes out to be 118 s. This enhanced residence time with the Zirfon membrane clearly shows that the residence time differences for the flowrates and flow fields stems from the mass transport differences in the liquid phase. Hence, mass transport from the liquid phase of the catalyst is rate limiting during CO_2RR which is why the differences in product distribution are observed for the various flowrates and gas flow field patterns.

In addition to this difference in mean residence time, another evidence supporting this rate limiting step is the shape of the RTD curves as shown in Figure 5.9. The red curve (without Zirfon) is more sharper than the black curve case (with Zirfon membrane). This clearly shows the delayed residence time occurs in the liquid region in direct contact with the MPL side of the GDL.

Differences between gas and liquid phase negative tracer measurements

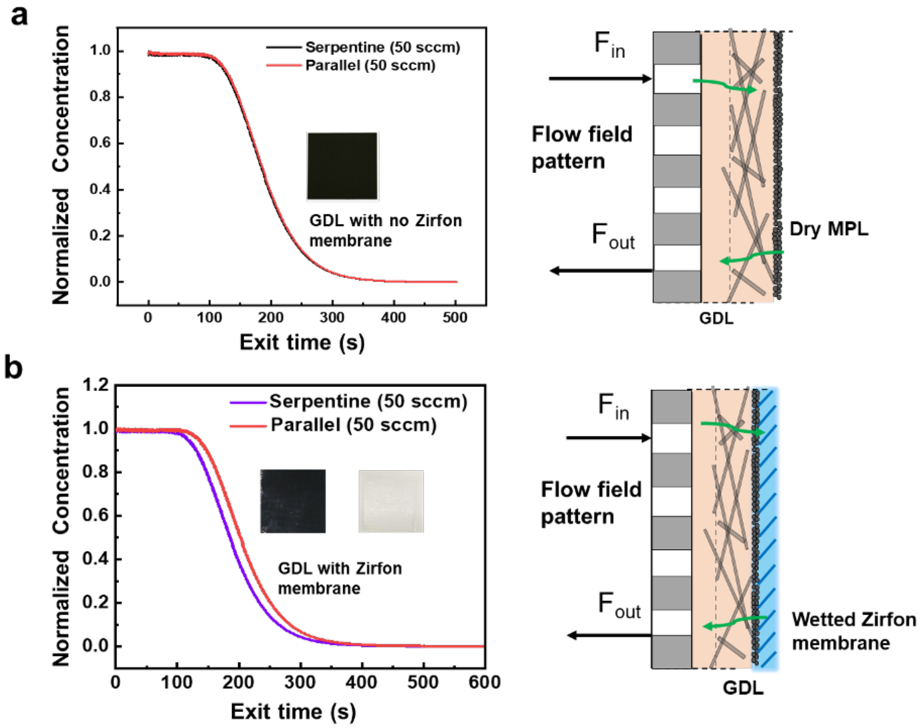

Figure 5.10 : Negative tracer results for the serpentine and parallel FFP at an inlet flowrate of 50 sccm without (a) Zirfon membrane pressed against the carbon GDL, (b) with Zirfon membrane pressed against the carbon GDL.

COMPARISON OF NEGATIVE TRACER MEASUREMENTS WITH ZIRFON MEMBRANE FOR BOTH FFP

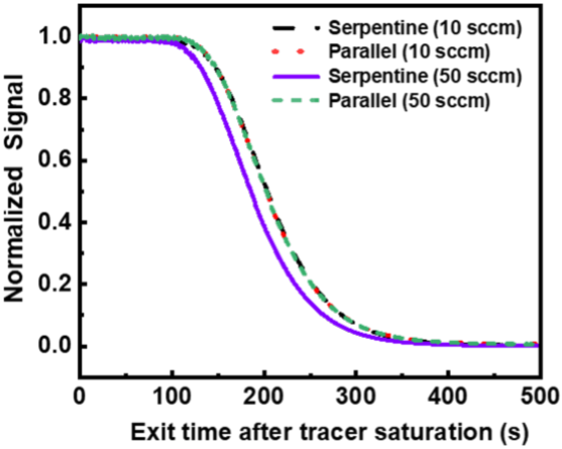

Figure 5.11 : Negative tracer results for the serpentine and parallel FFP at an inlet flowrate of 10 and 50 sccm with a wetted Zirfon membrane pressed against the carbon GDL.

COMPARISON OF PULSE TRACER MEASUREMENTS WITH ZIRFON MEMBRANE FOR PARALLEL FFP

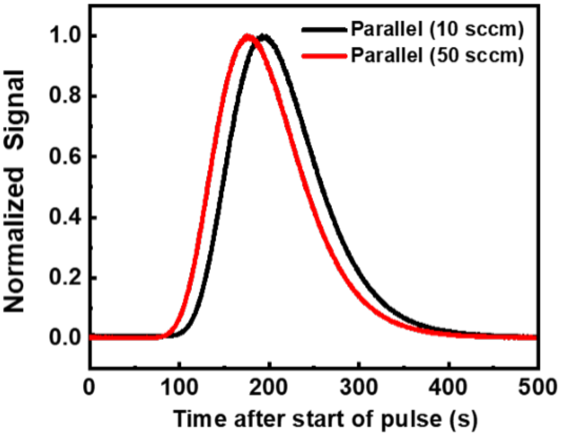

Figure 5.12 : Pulse RTD results of the parallel flow field pattern at an inlet flowrate of 10 and 50 sccm with a wetted Zirfon membrane pressed against the carbon GDL.

EXPERIMENTAL SETUP FOR CO_2 ELECTROLYSIS

All experiments were performed in a custom made membrane electrode assembly (MEA) cell comprising of a pin type flow field on the anode and different flow field patterns at the cathode. Sigracet 38 BC gas diffusion layers (GDL) of 5.06 cm^2 area (2.25 cm x 2.25 cm) was used as the porous transport layer. Cu catalysts were deposited on top of microporous layer of GDL by direct current magnetron sputtering under 3 μbar Ar flow at 20 sccm to form a uniform film of 100 nm. Nickel foam (3 cm x 3 cm, Recemat BV) was used as the anode. Cu coated GDL and Ni foam were combined with an oversized 16 cm^2 (4cm x 4cm) Sustainion anion exchange membrane (X37-50 Grade RT) to assemble the MEA. 0.5M KOH solution was fed at the anode at a constant flow rate of 20 ml/min and recirculated using a peristaltic pump similar to Figure 4.5 shown in previous chapter 4. Different CO_2 flowrates were used and the humidity at the inlet was measured to be 75%. Electrolysis at a geometric current density of 200 mA/cm^2 was performed under various operating conditions. Gas product quantification was performed by measuring outlet gas flowrates using a mass flow meter (MFM) followed by a gas chromatography (GC) with periodic injections every 5 minutes.

Electrochemical reactions at the cathode

$$CO_2 + H_2O + 2e^- \rightarrow CO + 2OH^- \tag{5.2}$$

$$CO_2 + 6H_2O + 8e^- \rightarrow CH_4 + 8OH^- \tag{5.3}$$

$$2CO_2 + 8H_2O + 12e^- \rightarrow C_2H_4 + 12OH^- \tag{5.4}$$

$$2CO_2 + 9H_2O + 12e^- \rightarrow C_2H_5OH + 12OH^- \tag{5.5}$$

$$2CO_2 + 6H_2O + 8e^- \rightarrow CH_3COOH + 8OH^- \tag{5.6}$$

$$3CO_2 + 13H_2O + 18e^- \rightarrow C_3H_7OH + 18OH^- \tag{5.7}$$

$$CO_2 + H_2O + 2e^- \rightarrow HCOO^- + 18OH^- \tag{5.8}$$

Carbon balance at the cathode

The faradaic efficiency of gaseous products were calculated using GC injections and measured outlet gas flowrate. The liquid products were quantified using H-NMR analysis. An overall carbon balance was performed and the following equations were then used to calculate the volumetric flowrate of CO_2 reacting with hydroxide ions at the cathode.

$$x_{CO_2,out} = 1 - (x_{CO} + x_{H_2} + x_{C_2H_4} + x_{CH_4} + x_{H_2O}) \tag{5.9}$$

After calculating the mole fractions of all gaseous products, the volumetric flow rate at the outlet of the reactor measured with the MFM and was used to calculate the moles of each product.

$$n_{CO} = x_{\mathrm{CO}} \times \dot{V}_{outlet} \tag{5.10}$$

$$n_{C_2H_4} = x_{\mathrm{C_2H_4}} \times \dot{V}_{outlet} \tag{5.11}$$

$$n_{CH_4} = x_{\mathrm{CH_4}} \times \dot{V}_{outlet} \tag{5.12}$$

$$n_{H_2} = x_{\mathrm{H_2}} \times \dot{V}_{outlet} \tag{5.13}$$

$$FE_{gas\ product} = \frac{n_{gas\ product} \times n^e \times F}{I} \tag{5.14}$$

Here: $n_{gas\ product}$ is the moles of produced gas product, n^e number of electrons involved in CO_2RR, F is Faraday's constant (96485 C/mol) and I is applied current (in Amperes).
The following equations were then used to calculate the CO_2 consumption with OH^- ions by performing an overall carbon balance at the cathode.

$$\dot{V}_{CO_2\ to\, CO} = x_{CO} \times \dot{V}_{outlet} \tag{5.15}$$

$$\dot{V}_{CO_2\ to\, C_2H_4} = x_{C_2H_4} \times \dot{V}_{outlet} \tag{5.16}$$

$$\dot{V}_{CH_4} = x_{CH_4} \times \dot{V}_{outlet} \tag{5.17}$$

$$\dot{V}_{H_2} = x_{H_2} \times \dot{V}_{outlet} \tag{5.18}$$

$$\dot{V}_{residual\, CO_2} = \dot{V}_{outlet} - (\dot{V}_{CO_2\ to\, CO} + \dot{V}_{CO_2\ to\, C_2H_4} + \dot{V}_{CO_2\ to\, CH_4} + \dot{V}_{H_2}) \tag{5.19}$$

$$\dot{V}\ _{CO_2\ to\ liquid\ prod} = \left((1 - x_{CO} - x_{H2}) \times \frac{j\,A}{n^e\,F} mol/s \right) \tag{5.20}$$

$$\dot{V}_{CO_2} to\, gas\ =\ \dot{V}_{CO_2\ to\, CO} + 2\,(\dot{V}_{CO_2\ to\, C2H4}) + \dot{V}\ _{CO_2\ to\ CH_4} \tag{5.21}$$

$$\dot{V}_{CO2\ to\ OH^-} = \dot{V}_{inlet} - (\dot{V}_{residual\ CO_2} + \dot{V}\ _{CO_2\ to\ gas\ products} + \dot{V}_{CO_2 to\ liquids}) \tag{5.22}$$

$$n_{CO2\ to\ OH^-} = \frac{\dot{V}_{CO2\ to\ OH^-}}{(24.42\ \times 60 \times 1000)}\ mol/s \tag{5.23}$$

$$\lambda_{stoich} = \frac{\dot{V}_{CO2,in}}{\dot{V}_{CO2,consumed}} \tag{5.24}$$

$$Single\ pass\ CO_2\ conversion = \frac{\dot{V}_{CO2\ to\ C2+\ products}}{\dot{V}_{inlet}} \tag{5.25}$$

$$CO_2\ util.\ efficiency = \frac{\dot{V}_{CO2\ to\ gas}\ + \dot{V}_{CO2\ to\ liquid\ prod}}{\dot{V}_{CO2\ to\ gas} + \dot{V}_{CO2\ to\ liquid\ prod}\ + \dot{V}_{CO2\ to\ OH^-}} \tag{5.26}$$

Moles of OH.- ions generated during the reaction can be calculated using Faraday's law. For every mole of OH^- ions produced during reactions (5.2-5.8), $1e^-$ is used.So,

$$n_{OH^-} = \frac{j_{geo} \times\ A}{1 \times F} = \frac{200\ mAcm^{-2} \times 5cm^2}{96485\ Cmol^{-1}} = 1.049 \times 10^{-5}\ moles \tag{5.27}$$

5.5.2. CO UTILIZATION TOWARDS C_{2+} PRODUCTS

From equations 5.4-5.6, the normalized partial current densities of hydrocarbons and oxygenates by the number of e⁻ transferred per CO reduced to a specific product is as follows:

$$CO_{generation\ rate} = j_{CO} + \frac{j_{CH_4}}{4} + \frac{j_{C_2H_4}}{3} + \frac{j_{C_2H_5OH}}{3} + \frac{j_{CH_3COO^-}}{2} + \frac{j_{C_3H_7OH}}{3} \tag{5.28}$$

$$CO_{dimerization\ rate} = \frac{j_{C_2H_4}}{3} + \frac{j_{C_2H_5OH}}{3} + \frac{j_{CH_3COO^-}}{2} + \frac{j_{C_3H_7OH}}{3} \tag{5.29}$$

$$CO_{utilization\ rate} = \frac{CO_{dimerization\ rate}}{CO_{generation\ rate}} \tag{5.30}$$

Table 5.1: Faradaic efficiency of CO and C_{2+} products obtained from CO_2RR for the three FFP at 200 mA/cm^2.

Flow field pattern	FE CO (%)	FE C_2H_4(%)	FE C_2H_5OH (%)	FE acetate (%)	FE n-propanol (%)	FE CH_4 (%)	FE H_2(%)
Serpentine (10 sccm)	3.2	40.3	30.8	10.5	2.7	1.4	7.2
Serpentine (50 sccm)	12.2	39.1	20.3	4.1	4.6	0.3	6.3
Parallel (10 sccm)	3.1	32	22.4	15.9	1.7	9.0	10.7
Parallel (50 sccm)	5.1	36.2	22.1	14.7	2.3	3.1	10.8
Interdigitated (10 sccm)	4.8	40.8	30.1	7.1	2.9	1.7	8.6

Table 5.2: Calculated single pass CO_2 conversion and CO utilization to C_{2+} products at 200 mA/cm^2.

CO_2flowrate (sccm)	Single pass conversion (%)	Stoichiometric excess of CO_2	CO generation rate(mA/cm^2)	CO dimerization rate (mA/cm^2)	CO utilization towards C_{2+}products (%)
10	23.91	1.13	66.4	59.7	89.9
20	14.25	1.92	71.0	53.1	74.7
30	9.28	2.56	70.3	51.5	74.2
40	6.63	3.44	70.0	48.4	69.2
50	5.42	4.01	71.7	46.8	65.3
10 (parallel)	19.38	1.16	63.9	53.4	81.5
50 (parallel)	3.92	5.61	67.8	55.3	83.6

NMR ANALYSIS FOR LIQUID PRODUCTS

The NMR experiments were conducted with a Bruker-400 NMR spectrometer. A water suppression technique was applied to make the products' peaks more visible. 25 mM of maleic acid dissolved in D_2O was used as the internal standard. 550 microlitres of aliquot from the anolyte of the MEA cell was taken and added to 50 microlitres of maleic acid (25 mM) for NMR analysis.

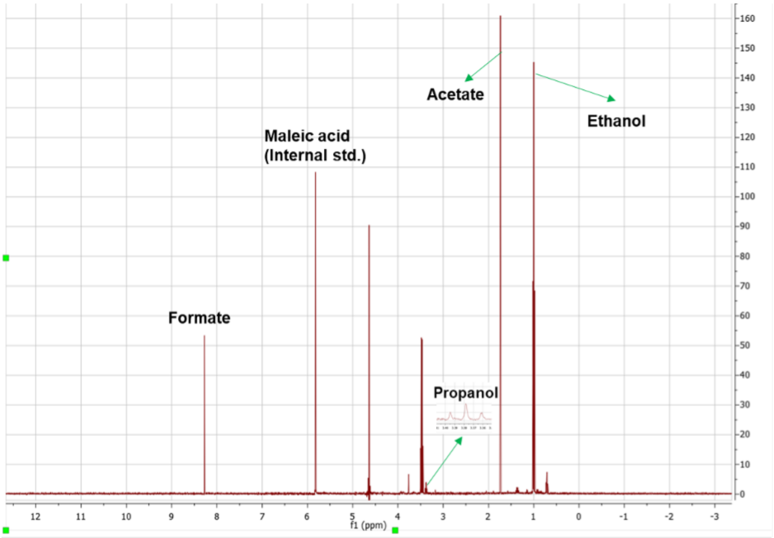

Figure 5.13 :H-NMR spectra of liquid products obtained from CO_2RR at an inlet flowrate of 10 sccm.

A total of 128 scans were performed for all tests and the molar concentration of liquid products were calculated using the equation:

$$C_x = \frac{I_x}{I_{std}} \times \frac{N_{std}}{N_x} \times C_{std} \tag{5.31}$$

Here, “C_x " is the molar concentration of the product, “I_x” is integral of the product, “I_{std}” is integral of the internal standard (maleic acid), "N_{std}” is the number of protons in maleic acid, "N_x” is the number of protons in the product, and "C_{std}" is the total concentration of maleic acid. “n” is the number of electrons for the specific product produced from CO_2. A sample NMR spectra for products obtained at the inlet flowrate of 10 sccm for the serpentine FFP is shown in Figure 5.13.

We also collected tiny liquid droplets from the cathode GDE into the liquid trap to quantify if any liquid products were present at the cathode side. The liquid drops from the liquid trap were diluted by adding MQ water to make a 10 mL solution and analyzed thereafter by NMR spectroscopy. NMR analysis showed only traces of ethanol with FE of 1-3%, suggesting that most of the produced liquid products migrated to the anode through the AEM.

Table 5.3: Liquid product selectivity produced from anode and cathode sides at different inlet CO_2 flowrates for the serpentine FFP.

Inlet flow rate of CO_2 (sccm)	FE of ethanol detected from anolyte (%)	FE of ethanol detected from cathode side (%)	Total FE of ethanol (%)
10	29.8	0.4	30.2
% 20	23.0	1.8	24.8
30	21.5	1.1	22.6
40	18.9	3.4	22.3
50	18.0	2.1	20.1

SEM ANALYSIS OF COPPER COATED GDL BEFORE AND AFTER CO_2RR

a **Before CO_2 RR**

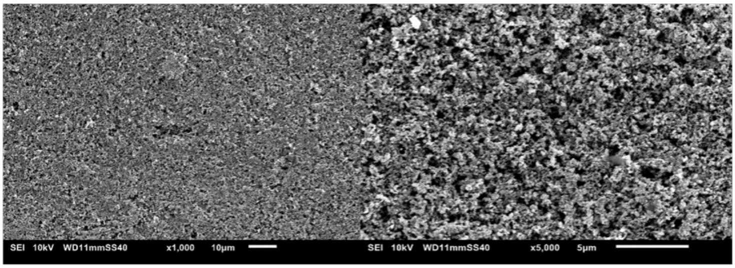

b **After CO_2 RR**

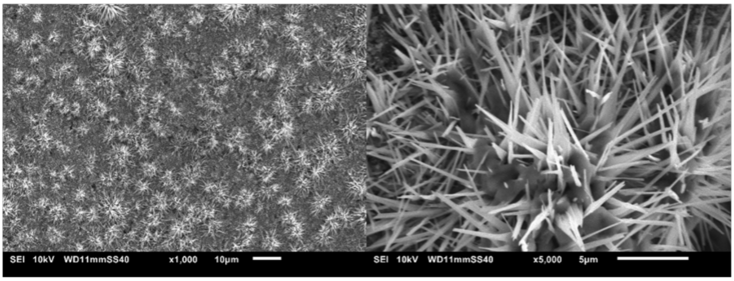

Figure 5.14 : SEM images of Cu catalyst layer sputtered on Sigracet 38 BC gas diffusion layer (a) before and (b) after 1h of CO_2 electrolysis.

5.6. MODEL DESCRIPTION

A 3D geometry of the cathode compartment (5cm^2 area) comprising of the three flow channel designs were modelled with the same length (2.1 cm), width (1 mm) and depth (1 mm) in COMSOL Multiphysics 5.5, similar to our previous work. A carbon GDL of dimensions (2.25 cm x 2.25 cm x 0.325 cm) was modelled and placed in contact with the flow field pattern with each one consisting of 11 channels and 10 ribs. The numerical simulations were performed using a MUMPS general solver with a relative tolerance of 0.001 to calculate the CO_2 concentration gradient in the gas channel and catalyst surface similar to the model described in chapter 4.
All parameters used in the model were taken from the experimental conditions and the properties of the Sigracet 38BC GDL. To solve for the species transport in the system, a mixture diffusion model was used. We accounted for only 2 gas species which are CO_2 at the inlet and C_2H_4 as the outlet since it was the dominant gas product. Other consumption of CO_2 was accounted for indirectly using experimentally calculated CO_2 consumption.

5.6.1. CO_2 CONSUMPTION CALCULATION

Electrochemical reduction of CO_2 to C_2H_4 was modelled which is a 12e$^-$ reduction reaction:

$$2CO_2 + 8H_2O + 12e^- \rightarrow C_2H_4 + 12OH^- \tag{5.32}$$

The CO_2 consumption to CO_2RR was calculated based on number of electrons involved for each molecule of CO_2 for the different products and their corresponding FEs. The FE of various products obtained from experiments was used for calculating CO_2 consumption.

$$z_{avg} = \left\{ \sum \left(\frac{FE_{C_i}}{FE_{CO2RR}} \times \frac{z_{e,C_i}}{\nu_{CO2}} \right) \right\} \tag{5.33}$$

Here z_{avg} is the average number of electrons utilized for CO_2RR, z_{e,C_i} is the number of electrons involved in CO_2RR to the specific product C_i (equations 5.2-5.8), ν_{CO2} is the stoichiometric coefficient of CO_2 for the specific CO_2RR. The moles of CO_2 lost to OH$^-$ ions calculated experimentally using carbon balance (Equation 5.22) was used in the model and assumed to occur homogenously throughout the catalyst layer. Using z_{avg} calculated from Equation 5.50, an equivalent current density was calculated and incorporated into the model for calculating CO_2 consumption.

$$j_{CO2\ to\ OH^-} = \frac{n_{CO2\ to\ OH^-} \times z_{avg} \times F}{A} \tag{5.34}$$

$$j_{total} = j_{CO2RR} + j_{CO2\ to\ OH^-} \tag{5.35}$$

Here, $j_{CO2\ to\ OH^-}$ is the equivalent current density per mole of CO_2 consumed due to reaction with OH$^-$ ions, F is Faraday's constant and A is the geometric area of the GDE (5.06 cm^2).

CALCULATED CO_2 CONCENTRATION AT THE G-L INTERFACE AT 10 SCCM

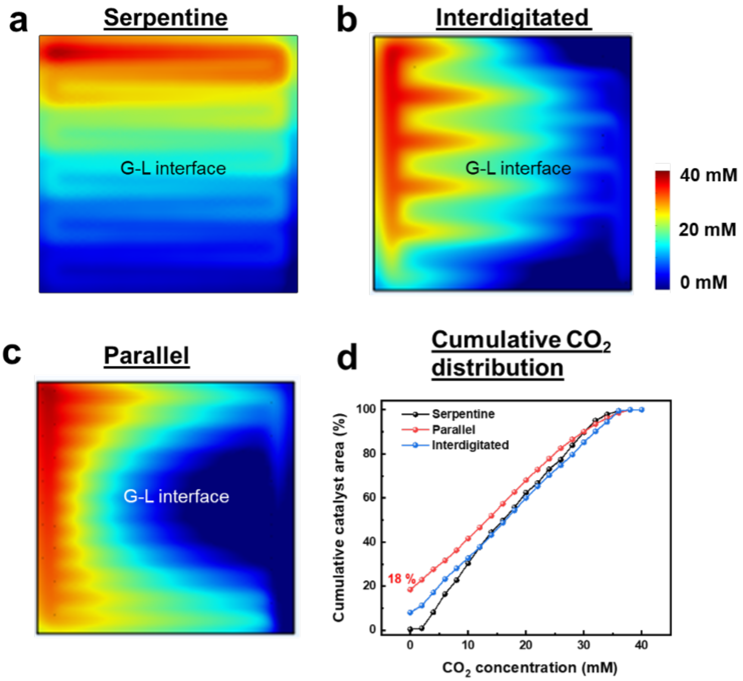

Figure 5.15 : Calculated gas phase CO_2 concentration at the G-L interface for (a) Serpentine, (b) Parallel and (c) Interdigitated flow field patterns at an inlet flowrate of 10 sccm and 200 mA/cm^2. (d) Cumulative CO_2 distribution at the G-L interface for all three FFPs.

CALCULATED CO_2 CONCENTRATION AT THE G-L INTERFACE FOR CO_2RR AT 50 SCCM

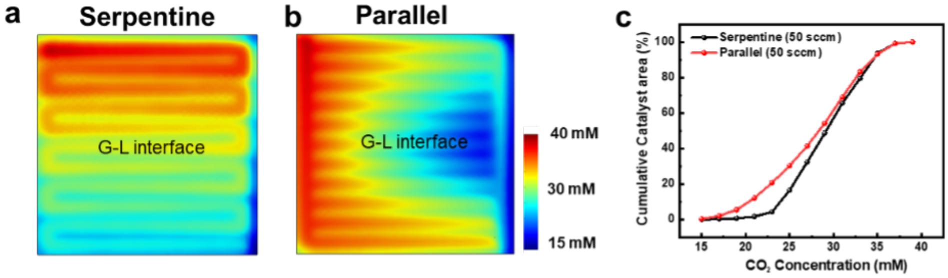

Figure 5.16 : Calculated gas phase CO_2 concentration at the G-L interface for (a) Serpentine, (b) Parallel flow field design at an inlet flowrate of 50 sccm and 200 mA/cm^2. (c) Cumulative CO_2 distribution for the two FFPs.

Table 5.4: Calculated pressure drop and gas phase CO_2 concentration at the G-L interface from the model for the three flow field patterns.

Flow field pattern	Inlet CO_2flowrate (sccm)	ΔP b/w inlet and outlet (Pa)	Avg. velocity in gas channels (mm/s)	Avg. [CO2] at G-L interface (mM)
Serpentine	10	22.2	1.3	17.8
Serpentine	50	112.4	5.7	30.9
Parallel	10	1.3	0.5	15.2
Parallel	50	6.4	1.9	28.9
Interdigitated	10	15.2	0.6	15.6

CO ELECTROLYSIS DATA

Electrochemical CO reduction tests were performed at 200 mA/cm_2 and an inlet flow rate of 20 sccm, inside a fumehood containing potentiostat, mass flow meter and gas chromatography setup. All experiments for the three flow field patterns were repeated twice to verify reproducibility. The electrical energy efficiency for ethylene+ethanol production is calculated using the following equation :

$$eEE = \left(\frac{FE_{C2H4} \times \mathbf{E^0_{cell,\ C_2H_4}}}{E_{cell}} \right) + \left(\frac{FE_{C2H5OH} \times \mathbf{E^0_{cell,\ C_2H_5OH}}}{E_{cell}} \right) \tag{5.36}$$

Table 5.5: Selectivity of products obtained from CORR at 200 mA/cm^2.

Flow field pattern	FE C_2H_4(%)	FE C_2H_5OH (%)	FE acetate (%)	FE n-propanol (%)	FE CH_4 (%)	FE H_2(%)
Serpentine	30.84	14.43	32.9	1.5	2.38	5.4
Parallel	29.3	15.5	31.7	1.7	4.15	9.5
Interdigitated	35.01	18	22.0	2.4	1.9	7.8

Table 5.6: Comparison of performance metrics for ethylene production from CO_2RR and CORR at 200 mA/cm^2.

Reaction	Full cell voltage obtained	TD Cell voltage for C_2H_4	TD Cell voltage for C_2H_5OH	FE of C_2H_4 (%)	FE of ethanol (%)	Electrical Energy efficiency, (eEE) (%)
CO_2RR	2.81	1.15	1.14	41.5	29.5	28.96
CO ER	2.47	1.06	1.04	35.0	20	23.42

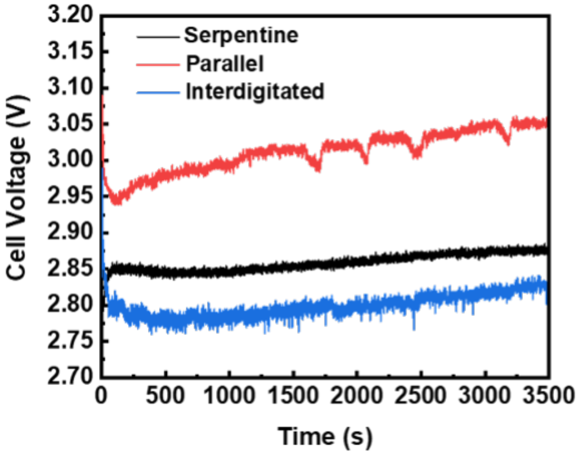

Figure 5.17 : Cell voltage during CO_2RR for the three FFP at an inlet flowrate of 10 sccm.

REFERENCES

[1] Y. Hori, I. Takahashi, O. Koga, and N. Hoshi. "Selective formation of C2 compounds from electrochemical reduction of CO2 at a series of copper single crystal electrodes". In: *The Journal of Physical Chemistry B* 106.1 (2002), pp. 15–17.

[2] A. J. Garza, A. T. Bell, and M. Head-Gordon. "Mechanism of CO2 reduction at copper surfaces: pathways to C2 products". In: *Acs Catalysis* 8.2 (2018), pp. 1490–1499.

[3] M. Gattrell, N. Gupta, and A. Co. "A review of the aqueous electrochemical reduction of CO2 to hydrocarbons at copper". In: *Journal of electroanalytical Chemistry* 594.1 (2006), pp. 1–19.

[4] K. P. Kuhl, E. R. Cave, D. N. Abram, and T. F. Jaramillo. "New insights into the electrochemical reduction of carbon dioxide on metallic copper surfaces". In: *Energy & Environmental Science* 5.5 (2012), pp. 7050–7059.

[5] A. A. Peterson, F. Abild-Pedersen, F. Studt, J. Rossmeisl, and J. K. Nørskov. "How copper catalyzes the electroreduction of carbon dioxide into hydrocarbon fuels". In: *Energy & Environmental Science* 3.9 (2010), pp. 1311–1315.

[6] G. Mangione, J. Huang, R. Buonsanti, and C. Corminboeuf. "Dual-facet mechanism in copper nanocubes for electrochemical CO2 reduction into ethylene". In: *The Journal of Physical Chemistry Letters* 10.15 (2019), pp. 4259–4265.

[7] Y. Zheng, A. Vasileff, X. Zhou, Y. Jiao, M. Jaroniec, and S.-Z. Qiao. "Understanding the roadmap for electrochemical reduction of CO2 to multi-carbon oxygenates and hydrocarbons on copper-based catalysts". In: *Journal of the American Chemical Society* 141.19 (2019), pp. 7646–7659.

[8] T. K. Todorova, M. W. Schreiber, and M. Fontecave. "Mechanistic understanding of CO2 reduction reaction (CO2RR) toward multicarbon products by heterogeneous copper-based catalysts". In: *Acs Catalysis* 10.3 (2019), pp. 1754–1768.

[9] K. Rossi and R. Buonsanti. "Shaping copper nanocatalysts to steer selectivity in the electrochemical CO2 reduction reaction". In: *Accounts of Chemical Research* 55.5 (2022), pp. 629–637.

[10] G. L. De Gregorio, T. Burdyny, A. Loiudice, P. Iyengar, W. A. Smith, and R. Buonsanti. "Facet-dependent selectivity of Cu catalysts in electrochemical CO2 reduction at commercially viable current densities". In: *ACS catalysis* 10.9 (2020), pp. 4854–4862.

[11] C. Zhan, F. Dattila, C. Rettenmaier, A. Bergmann, S. Kühl, R. García-Muelas, N. López, and B. R. Cuenya. “Revealing the CO coverage-driven C–C coupling mechanism for electrochemical CO2 reduction on Cu2O nanocubes via operando Raman spectroscopy”. In: *ACS catalysis* 11.13 (2021), pp. 7694–7701.

[12] C.-T. Dinh, T. Burdyny, M. G. Kibria, A. Seifitokaldani, C. M. Gabardo, F. P. García de Arquer, A. Kiani, J. P. Edwards, P. De Luna, O. S. Bushuyev, *et al.* “CO2 electroreduction to ethylene via hydroxide-mediated copper catalysis at an abrupt interface”. In: *Science* 360.6390 (2018), pp. 783–787.

[13] F. P. García de Arquer, C.-T. Dinh, A. Ozden, J. Wicks, C. McCallum, A. R. Kirmani, D.-H. Nam, C. Gabardo, A. Seifitokaldani, X. Wang, *et al.* “CO2 electrolysis to multicarbon products at activities greater than 1 A cm- 2”. In: *Science* 367.6478 (2020), pp. 661–666.

[14] S. Nitopi, E. Bertheussen, S. B. Scott, X. Liu, A. K. Engstfeld, S. Horch, B. Seger, I. E. Stephens, K. Chan, C. Hahn, *et al.* “Progress and perspectives of electrochemical CO2 reduction on copper in aqueous electrolyte”. In: *Chemical reviews* 119.12 (2019), pp. 7610–7672.

[15] A. Bagger, W. Ju, A. S. Varela, P. Strasser, and J. Rossmeisl. “Electrochemical CO2 reduction: a classification problem”. In: *ChemPhysChem* 18.22 (2017), pp. 3266–3273.

[16] C. W. Li, J. Ciston, and M. W. Kanan. “Electroreduction of carbon monoxide to liquid fuel on oxide-derived nanocrystalline copper”. In: *Nature* 508.7497 (2014), pp. 504–507.

[17] K. J. P. Schouten, E. P. Gallent, and M. T. Koper. “The influence of pH on the reduction of CO and CO2 to hydrocarbons on copper electrodes”. In: *Journal of Electroanalytical Chemistry* 716 (2014), pp. 53–57.

[18] R. Kortlever, J. Shen, K. J. P. Schouten, F. Calle-Vallejo, and M. T. Koper. “Catalysts and reaction pathways for the electrochemical reduction of carbon dioxide”. In: *The journal of physical chemistry letters* 6.20 (2015), pp. 4073–4082.

[19] X. Wang, J. F. de Araújo, W. Ju, A. Bagger, H. Schmies, S. Kühl, J. Rossmeisl, and P. Strasser. “Mechanistic reaction pathways of enhanced ethylene yields during electroreduction of CO2–CO co-feeds on Cu and Cu-tandem electrocatalysts”. In: *Nature nanotechnology* 14.11 (2019), pp. 1063–1070.

[20] W. Gao, Y. Xu, L. Fu, X. Chang, and B. Xu. “Experimental evidence of distinct sites for CO2-to-CO and CO conversion on Cu in the electrochemical CO2 reduction reaction”. In: *Nature Catalysis* 6.10 (2023), pp. 885–894.

[21] S. Louisia, D. Kim, Y. Li, M. Gao, S. Yu, I. Roh, and P. Yang. “The presence and role of the intermediary CO reservoir in heterogeneous electroreduction of CO2”. In: *Proceedings of the National Academy of Sciences* 119.18 (2022), e2201922119.

[22] C. G. Morales-Guio, E. R. Cave, S. A. Nitopi, J. T. Feaster, L. Wang, K. P. Kuhl, A. Jackson, N. C. Johnson, D. N. Abram, T. Hatsukade, *et al.* "Improved CO2 reduction activity towards C2+ alcohols on a tandem gold on copper electrocatalyst". In: *Nature Catalysis* 1.10 (2018), pp. 764–771.

[23] Y. Lum and J. W. Ager. "Sequential catalysis controls selectivity in electrochemical CO 2 reduction on Cu". In: *Energy & Environmental Science* 11.10 (2018), pp. 2935–2944.

[24] T. Zhang, Z. Li, J. Zhang, and J. Wu. "Enhance CO2-to-C2+ products yield through spatial management of CO transport in Cu/ZnO tandem electrodes". In: *Journal of catalysis* 387 (2020), pp. 163–169.

[25] C. Chen, Y. Li, S. Yu, S. Louisia, J. Jin, M. Li, M. B. Ross, and P. Yang. "Cu-Ag tandem catalysts for high-rate CO2 electrolysis toward multicarbons". In: *Joule* 4.8 (2020), pp. 1688–1699.

[26] T. Zhang, J. C. Bui, Z. Li, A. T. Bell, A. Z. Weber, and J. Wu. "Highly selective and productive reduction of carbon dioxide to multicarbon products via in situ CO management using segmented tandem electrodes". In: *Nature Catalysis* 5.3 (2022), pp. 202–211.

[27] L.-C. Weng, A. T. Bell, and A. Z. Weber. "A systematic analysis of Cu-based membrane-electrode assemblies for CO 2 reduction through multiphysics simulation". In: *Energy & Environmental Science* 13.10 (2020), pp. 3592–3606.

[28] C. M. Gabardo, C. P. O'Brien, J. P. Edwards, C. McCallum, Y. Xu, C.-T. Dinh, J. Li, E. H. Sargent, and D. Sinton. "Continuous carbon dioxide electroreduction to concentrated multi-carbon products using a membrane electrode assembly". In: *Joule* 3.11 (2019), pp. 2777–2791.

[29] E. W. Lees, B. A. Mowbray, F. G. Parlane, and C. P. Berlinguette. "Gas diffusion electrodes and membranes for CO2 reduction electrolysers". In: *Nature Reviews Materials* 7.1 (2022), pp. 55–64.

[30] H. Simonson, W. E. Klein, D. Henckel, S. Verma, K. Neyerlin, and W. A. Smith. "Direct Measurement of Electrochemical Selectivity Gradients over a 25 cm2 Copper Gas Diffusion Electrode". In: *ACS Energy Letters* 8.9 (2023), pp. 3811–3819.

[31] U. Krewer, Y. Song, K. Sundmacher, V. John, R. Lübke, G. Matthies, and L. Tobiska. "Direct methanol fuel cell (DMFC): analysis of residence time behaviour of anodic flow bed". In: *Chemical Engineering Science* 59.1 (2004), pp. 119–130.

[32] F. Barreras, A. Lozano, L. Valino, C. Marin, and A. Pascau. "Flow distribution in a bipolar plate of a proton exchange membrane fuel cell: experiments and numerical simulation studies". In: *Journal of Power sources* 144.1 (2005), pp. 54–66.

[33] F. Trachsel, A. Günther, S. Khan, and K. F. Jensen. "Measurement of residence time distribution in microfluidic systems". In: *Chemical Engineering Science* 60.21 (2005), pp. 5729–5737.

[34] J. Diep, D. Kiel, J. St-Pierre, and A. Wong. “Development of a residence time distribution method for proton exchange membrane fuel cell evaluation”. In: *Chemical engineering science* 62.3 (2007), pp. 846–857.

[35] N. T. Nesbitt, T. Burdyny, H. Simonson, D. Salvatore, D. Bohra, R. Kas, and W. A. Smith. “Liquid–solid boundaries dominate activity of CO2 reduction on gas-diffusion electrodes”. In: *ACS Catalysis* 10.23 (2020), pp. 14093–14106.

[36] P. Wei, D. Gao, T. Liu, H. Li, J. Sang, C. Wang, R. Cai, G. Wang, and X. Bao. “Coverage-driven selectivity switch from ethylene to acetate in high-rate CO2/CO electrolysis”. In: *Nature Nanotechnology* 18.3 (2023), pp. 299–306.

[37] D. S. Ripatti, T. R. Veltman, and M. W. Kanan. “Carbon monoxide gas diffusion electrolysis that produces concentrated C2 products with high single-pass conversion”. In: *Joule* 3.1 (2019), pp. 240–256.

[38] J. Li, A. Xu, F. Li, Z. Wang, C. Zou, C. M. Gabardo, Y. Wang, A. Ozden, Y. Xu, D.-H. Nam, *et al.* “Enhanced multi-carbon alcohol electroproduction from CO via modulated hydrogen adsorption”. In: *Nature communications* 11.1 (2020), p. 3685.

[39] S. Brückner, Q. Feng, W. Ju, D. Galliani, A. Testolin, M. Klingenhof, S. Ott, and P. Strasser. “Design and Diagnosis of high-performance CO2-to-CO electrolyzer cells”. In: (2023).

[40] E. Bertheussen, A. Verdaguer-Casadevall, D. Ravasio, J. H. Montoya, D. B. Trimarco, C. Roy, S. Meier, J. Wendland, J. K. Nørskov, I. E. Stephens, *et al.* “Acetaldehyde as an intermediate in the electroreduction of carbon monoxide to ethanol on oxide-derived copper”. In: *Angewandte Chemie International Edition* 55.4 (2016), pp. 1450–1454.

[41] M. Jouny, W. Luc, and F. Jiao. “High-rate electroreduction of carbon monoxide to multi-carbon products”. In: *Nature Catalysis* 1.10 (2018), pp. 748–755.

[42] M. Ma, E. L. Clark, K. T. Therkildsen, S. Dalsgaard, I. Chorkendorff, and B. Seger. “Insights into the carbon balance for CO 2 electroreduction on Cu using gas diffusion electrode reactor designs”. In: *Energy & Environmental Science* 13.3 (2020), pp. 977–985.

[43] S. **Subramanian**, K. Yang, M. Li, M. Sassenburg, M. Abdinejad, E. Irtem, J. Middelkoop, and T. Burdyny. “Geometric Catalyst Utilization in Zero-Gap CO_2 Electrolyzers”. In: *ACS Energy Letters* 8.1 (2022), pp. 222–229.

[44] J. Li, Z. Wang, C. McCallum, Y. Xu, F. Li, Y. Wang, C. M. Gabardo, C.-T. Dinh, T.-T. Zhuang, L. Wang, *et al.* “Constraining CO coverage on copper promotes high-efficiency ethylene electroproduction”. In: *Nature Catalysis* 2.12 (2019), pp. 1124–1131.

[45] M. Schreier, Y. Yoon, M. N. Jackson, and Y. Surendranath. “Competition between H and CO for active sites governs copper-mediated electrosynthesis of hydrocarbon fuels”. In: *Angewandte Chemie* 130.32 (2018), pp. 10378–10382.

[46] W. Luc, X. Fu, J. Shi, J.-J. Lv, M. Jouny, B. H. Ko, Y. Xu, Q. Tu, X. Hu, J. Wu, *et al.* “Two-dimensional copper nanosheets for electrochemical reduction of carbon monoxide to acetate”. In: *Nature Catalysis* 2.5 (2019), pp. 423–430.

[47] L. Wang, S. A. Nitopi, E. Bertheussen, M. Orazov, C. G. Morales-Guio, X. Liu, D. C. Higgins, K. Chan, J. K. Nørskov, C. Hahn, *et al.* “Electrochemical carbon monoxide reduction on polycrystalline copper: effects of potential, pressure, and pH on selectivity toward multicarbon and oxygenated products”. In: *Acs Catalysis* 8.8 (2018), pp. 7445–7454.

[48] S. C. da Cunha and J. Resasco. “Maximizing single-pass conversion does not result in practical readiness for CO2 reduction electrolyzers”. In: *nature communications* 14.1 (2023), p. 5513.

[49] H. H. Heenen, H. Shin, G. Kastlunger, S. Overa, J. A. Gauthier, F. Jiao, and K. Chan. “The mechanism for acetate formation in electrochemical CO (2) reduction on Cu: selectivity with potential, pH, and nanostructuring”. In: *Energy & Environmental Science* 15.9 (2022), pp. 3978–3990.

[50] S. Guo, Y. Liu, Y. Huang, H. Wang, E. Murphy, L. Delafontaine, J. “ Chen, I. V. Zenyuk, and P. Atanassov. “Promoting Electrolysis of Carbon Monoxide toward Acetate and 1-Propanol in Flow Electrolyzer”. In: *ACS Energy Letters* 8.2 (2023), pp. 935–942.

[51] T. Burdyny and W. A. Smith. “CO 2 reduction on gas-diffusion electrodes and why catalytic performance must be assessed at commercially-relevant conditions”. In: *Energy & Environmental Science* 12.5 (2019), pp. 1442–1453.

[52] C. Kim, J. C. Bui, X. Luo, J. K. Cooper, A. Kusoglu, A. Z. Weber, and A. T. Bell. “Tailored catalyst microenvironments for CO2 electroreduction to multicarbon products on copper using bilayer ionomer coatings”. In: *Nature Energy* 6.11 (2021), pp. 1026–1034.

[53] B. Endrődi, A. Samu, E. Kecsenovity, T. Halmágyi, D. Sebők, and C. Janáky. “Operando cathode activation with alkali metal cations for high current density operation of water-fed zero-gap carbon dioxide electrolysers”. In: *Nature energy* 6.4 (2021), pp. 439–448.

[54] T. N. Nguyen, Z. Chen, A. S. Zeraati, H. S. Shiran, S. M. Sadaf, M. G. Kibria, E. H. Sargent, and C.-T. Dinh. “Catalyst regeneration via chemical oxidation enables long-term electrochemical carbon dioxide reduction”. In: *Journal of the American Chemical Society* 144.29 (2022), pp. 13254–13265.

[55] G. Kastlunger, H. H. Heenen, and N. Govindarajan. “Combining First-Principles Kinetics and Experimental Data to Establish Guidelines for Product Selectivity in Electrochemical CO2 Reduction”. In: *ACS Catalysis* 13.7 (2023), pp. 5062–5072.

[56] A. Mohsenzadeh, A. Zamani, and M. J. Taherzadeh. “Bioethylene production from ethanol: a review and techno-economical evaluation”. In: *ChemBioEng Reviews* 4.2 (2017), pp. 75–91.

[57] T. Moore, D. I. Oyarzun, W. Li, T. Y. Lin, M. Goldman, A. A. Wong, S. A. Jaffer, A. Sarkar, S. E. Baker, E. B. Duoss, *et al.* “Electrolyzer energy dominates separation costs in state-of-the-art CO2 electrolyzers: Implications for single-pass CO2 utilization”. In: *Joule* 7.4 (2023), pp. 782–796.

6

CATION CROSSOVER IN AEM BASED ZERO-GAP CO_2 ELECTROLYZERS: A DOUBLE EDGED SWORD

No great discovery was ever made without a bold guess.

- Issac Newton

CO_2 electrolysis using silver (Ag) and copper (Cu) based catalysts have been widely studied due to their ability to produce CO and multi-carbon products respectively. In industrially relevant membrane electrode assembly configurations, long term operational stability is hampered due to (bi) carbonate precipitation at the cathode triggered by alkali metal cation crossover from the anode. In this work, we investigate the role of cation crossover for Ag and Cu based catalysts by varying cation concentrations and the cation identity. We find that cation crossover from the anode is essential for CO_2 activation and cation identity (K+, Na+) affect CO_2RR selectivities significantly as shown in a number of previous studies. Further, we find that cation concentration do not alter product selectivity for a Ag catalyst producing CO, but alter product distribution significantly for a Cu catalyst, showing that C-C coupling rates are significantly affected by local cation concentration at the cathode. In contrast, cation crossover is detrimental for long term operation due to (bi) carbonate precipitation at the electrolyte free cathode, that induces flooding of the gas diffusion electrode over time. These results reveal that a proper management of local cation and water concentrations are essential in order to acheive long term operational stability in zero gap CO_2 electrolyzers.

This work was part of Proceedings of MATSUS Fall 2023 Conference (MATSUSFall23) by S.Subramanian and T. Burdyny.

6.1. INTRODUCTION

CO_2 electrolysis using anion exchange membrane electrode assembly (AEMEA) configuration have shown promise for finding a fine balance between various performance metrics such as cell voltage, faradaic efficiency and limiting current density of a desired product [1–3]. However, for these electrolyzers to be cost competitive with alternate technologies producing value added chemicals such as CO and ethylene, stability of operation for around 10,000 hrs are required[4, 5]. An inherent issue with this system that limits long term stability of operation is the (bi) carbonate precipitation at the cathode side of the reactor [6].

Extensive works have now shown strategies to mitigate or delay salt precipitation[7–11], however these are still limited to < 200 hrs of operation. Endrodi et.al reported a periodic electrolyte pulse strategy to run the AEMEA reactor for 200 hrs [12] at higher current densities (> 200 mA/cm^2). By injecting alkali cations periodically from the back of GDE, they were able to avoid salt precipitation effectively. An important finding from this study was that the cation crossover from the anolyte to the cathode side of the reactor is essential for CO_2 activation at the catalyst surface, without which no CO_2RR would occur. Monteiro et. al [13] also showed that alkali metal cations are essential for CO_2 activation at the catalyst surface and directly couples with CO_2 and an electron during this activation process at the negatively charged electrode. They postulated that a cation directly couples with CO_2^- radical anion before an interaction with a proton.

In AEMEA reactors where humidified CO_2 is fed at the cathode, a sufficient cation concentration at the catalyst microenvironment is then essential for CO_2RR. Alkali metal cations in the anolyte such as $KHCO_3$ or KOH is used for the OER reaction at the anode, but some crossover of these cations to the cathode side are commonly observed. This is primarily due to inability of AEMs to have 100% permselectivity for anions and electroosmotic drag during CO_2RR drives these hydrated cations from the anode side towards the negatively charged cathode.

The crossover of alkali cations towards the cathode during CO_2RR is also the primary reason for why (bi) carbonate salts start to form and precipitate gradually at the cathode GDE, leading to failure of operation over time. The rate of cation crossover is found to increase with increasing current densities and strategies to limit failure of operation was discussed in a recent perspective [8]. An ideal solution to this problem is then to use a conductive ionomer for the anode catalyst and use DI water as the anolyte during operation. This will get rid of any potassium ions entirely, thus preventing salt formation and precipitation completely.

In this work, we studied the influence of cation crossover on product selectivity for silver (Ag) and copper (Cu) based catalysts in AEMEA cells and found that no CO_2RR occurs when operated with pure water, even with the presence of cationic functional groups present in the Ag catalyst layer, suggesting that alkali metal cation crossover is essential for CO_2RR. In addition, cation crossover rate seems to directly affect C-C coupling rates for a Cu catalyst with higher ethylene and lower CO selectivity observed at anolyte concentrations > 0.1 M. Similar effects were also observed for a BPM operating under reverse bias, revealing that cation crossover is a 'double edged sword' in zero gap membrane electrode assembly reactors.

6.2. RESULTS AND DISCUSSION

6.2.1. CATION EFFECT FOR A SILVER CATALYST

We first investigated the influence of cation crossover rates on the performance of a Ag catalyst producing CO. Ag catalyst was sputtered onto a carbon based GDL similar to the work discussed in the previous chapters. We first used KOH and $KHCO_3$ electrolyte solutions as anolyte and varied their molar concentrations from 0.01 to 1M. An IrO_2 anode was used for OER at the anode. All tests were performed at a geometric current density of 200 mA/cm^2. Product quantification was performed similar to methods used in previous chapters. A pristine Ag GDE was used in each experiment.

As shown in Figure 6.1, we find no significant differences in Faradaic efficiencies for CO (72%) and H_2 (3-5%) selectivity are observed across the various anolyte concentrations used. The remaining faradaic current goes towards formation of formate ($HCOO^-$), however it was not measurable due to migration and subsequent oxidation to CO_2 at the anode. The observation of similar CO selectivity with various anolyte concentration shows that K^+ cation concentration above 10 mM do not influence CO and H_2 production during CO_2RR. This means a threshold concentration of cations around the Ag catalyst is sufficient for CO_2 activation and electroreduction to CO.

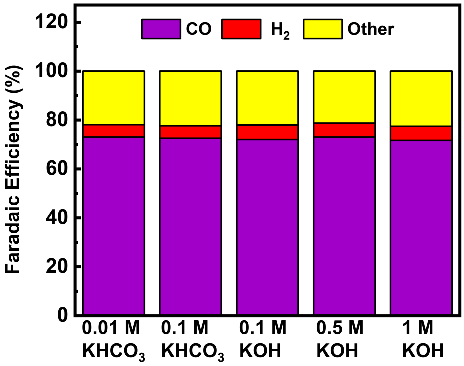

Figure 6.1 : CO and H_2 faradaic efficiencies for a Ag catalyst at 200 mA/cm^2 with varying K^+ concentration in the anolyte. Ni foam was used as the anode for KOH anolyte and IrO_2 for $KHCO_3$ anolyte.

We then switched to NaOH and DI water as the anolyte instead of potassium to get further insights on the performance. As illustrated in Figure 6.2, we see that both NaOH and DI water anolytes do not promote CO_2RR compared to KOH anolyte specifically above 50 mA/cm^2, revealing two important observations. First, weakly hydrated cations such as K^+ or Cs^+ are better for CO_2RR than strongly hydrated cations such as Na^+. This trend has already been shown in previous studies on why weakly hydrated cations are essential for CO_2 activation at the catalyst surface. Second, partial current densities of CO are limited to 10 mA/cm^2 at all current densities and HER dominates when DI water is used as the anolyte, showing no CO_2RR in the absence of cations in the anolyte. The sustainion membranes used in these experiments were all pre-activated in 1 M KOH solution and it's likely that some K^+ ions may be present on the membrane surface during electrochemical tests. The observation of no significant CO_2RR activity even with this membrane shows that a steady crossover of K^+ ions from the anolyte may be necessary for high rate CO_2RR.

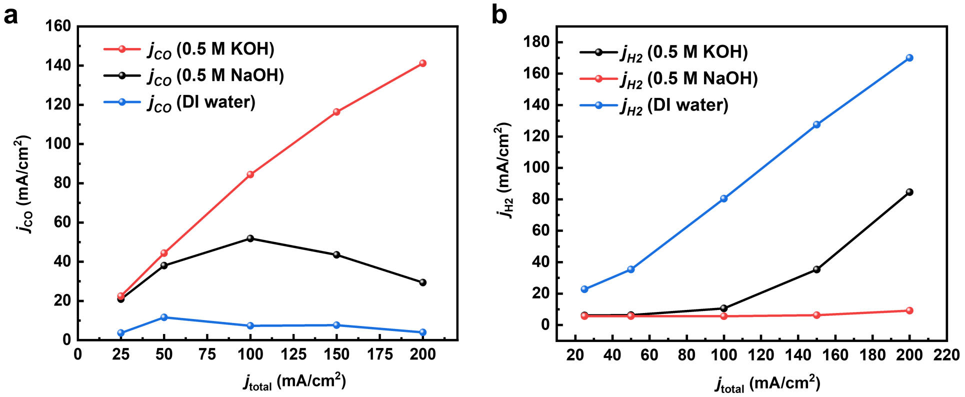

Figure 6.2 : Partial current densities of (a) CO and (b) H_2 obtained for a Ag catalyst with various anolytes in an MEA cell.

Next, we switched to spray coated Ag catalyst on carbon GDL as the electrode on the cathode side. The Ag catalyst was sprayed onto the carbon GDL using Ag nanoparticles and a Sustainion ionomer to get a final loading of 0.1 mg/cm^2. This loading was chosen to make a fair comparison with sputtered Ag catalyst layer which had the same mass loading. With the use of DI water as anolyte, we investigated if the cationic functional groups present in the ionomer could replace the co-catalytic effect of the alkali metal cation migrating from cathode to the anode. The sustainion ionomer has imidazolium cationic groups present in it and should enable the key step of CO_2 adsorption at the catalyst surface.

The results obtained are shown in Figure 6.3, where we see that the partial current densities of CO were below 10 mA/cm^2, with hydrogen being the dominant product, similar to the results obtained for a sputtered Ag catalyst layer. These findings show that the presence of the sustainion ionomer inside the Ag catalyst layer may not be sufficient to reach reasonable CO partial current densities and suppress HER. A constant supply of alkali cations might then be necessary for high rate CO_2RR in AEMEA reactors.

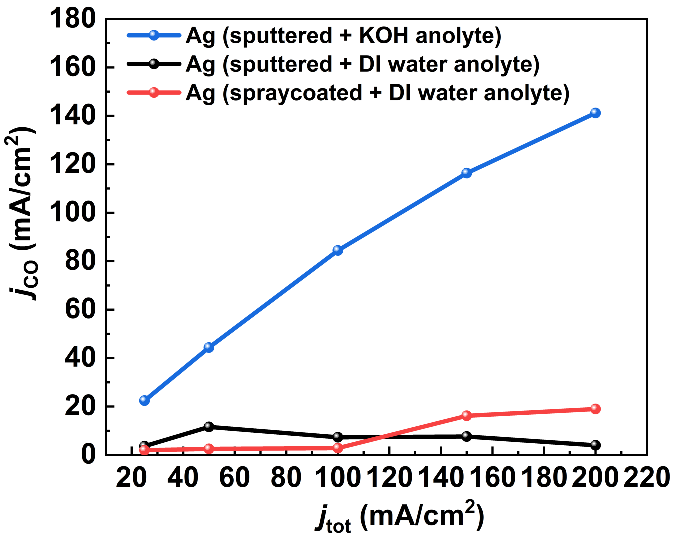

Figure 6.3 : Comparison of CO partial current densities for Ag catalyst layer prepared by sputter deposition without any ionomer and spray coated with sustainion ionomer at 200 mA/cm^2.

6.3. CATION CROSSOVER AFFECTS C-C COUPLING IN A COPPER BASED MEA CELL

We then investigated the influence of cation concentration for CO_2RR to CO and ethylene on a Cu based catalyst in AEMEA cell. We choose potassium bicarbonate as anolyte and varied the concentration keeping the applied current density fixed at 200 mA/cm^2. A thin Cu catalyst layer (200nm) was deposited on Sigracet 38 BC carbon GDL for the cathode. For the anode side, Pt catalyst was sputter deposited on Ti porous substrate to obtain a loading of 0.1 mg/cm^2. Due to challenges with measuring liquid products obtained from CO_2 RR as product migration and subseqent oxidation are known to occur, we measured only the gaseous products (CO, CH_4, C_2H_4, H_2) from the cathode.

As shown in Figure 6.3, we find that cation crossover rates from anode to cathode not only affect CO_2 activation, but also influence CO and ethylene selectivity. In particular, a linear decrease in CO selectivity from 30% to 6% with an increase in $KHCO_3$ concentrations from 0.01 M to 0.5 M. Ethylene selectivity follows the inverse trend from 28% at 0.01 M to 40% at 0.5 M anolye concentration. The observation of predominantly CO under conditions of cation deficiency might be supportive of a mechanism dependent on cation coverage or local concentration as shown in a recent study [14]. In this scenario, the C_{2+} pathway is likely enabled only when cation levels are sufficiently high, particularly at or near the interface. Considering that increased cation crossover stems from increased anolyte concentration (due to higher diffusion), it is then beneficial to use higher alkali cation concentrations in the anolyte for maximizing C-C coupling. In contrast lower concentrations might favour CO production from Cu. Using the knowlege of residence time of reactants from chapter 5, we then postulated that using 0.01 M $KHCO_3$ and higher inlet CO_2 flowrate (lower residence time) might show even higher CO selectivity. To test this, we then used a pristine Cu GDE with 0.01 M $KHCO_3$ anolyte and operated the MEA cell at 200 mA/cm^2 and varied CO_2 flowrates (10 to 50 sccm). As shown in Figure 6.4, we see the highest CO selectivity of 50% at 50 sccm and 0.01 M $KHCO_3$. This further proves that local cation concentration and reactant residence time are both dominant factors affecting C-C coupling on Cu based catalysts.

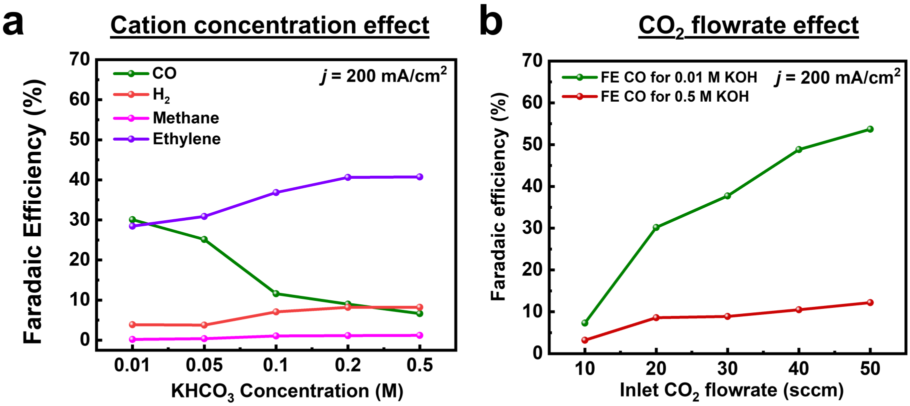

Figure 6.4 : Partial current densities of CO, C_2H_4, CH_4 and H_2 for a Cu catalyst with different K^+ concentration in the anolyte.

The dependence of CO and ethylene selectivity on anolyte concentration in MEA cell also shows that local electric field altered by concentration of cations at the double layer influence C-C coupling rates as shown in previous studies[15–19]. This has important implications for scaling up AEMEA reactors using Cu based catalysts. Since, higher cation concentrations are essential for increased C_{2+} production rates, trade-offs might exist between salt precipitation and C_{2+} selectivity, due to the requirement of higher alkali cation concentrations in the anolyte. Increased cation crossover will then lead to a faster carbonate precipitation at the cathode and subsequent failure of operation. In addition, the use of Cs based anolytes would be beneficial due to the higher solubility of $CsHCO_3$ (10.7 M) salt than $KHCO_3$ (3.6 M) that forms at the cathode side and an order of magnitude lower transference number (1×10^{-5}) than K^+ (1×10^{-4}) [20].

From a membrane perspective, it is important to understand the challenges associated with designing anion exchange membranes with 100% permselectivity for anions. The transport of cations through an AEM is influenced by multiple factors such as the concentration gradient, applied electric field and membrane hydration.

One factor that governs transport of counter-ions (cations) while excluding transport of co-ions (anions) is Donnan exclusion[21–23]. Donnan exclusion is affected by concentration of cations in the electrolyte and fixed charge groups in the AEM. As the ratio of fixed charged groups/concentration of anolyte decreases, a decrease in Donnan exclusion occurs leading to higher rates of cation crossover. This means that increasing the fixed charge concentration in the AEM will maximize Donnan exclusion, but this also can lead to increased water uptake and excessive membrane swelling[24–27]. Understanding the trade-offs associated with these parameters are then crucial for designing stable AEM based CO_2 electrolyzers.

6.4. REPLACING ALKALI CATIONS WITH ORGANIC CATIONS

Some of the recent studies have shown that alkali cations causing salt precipitation can be eliminated by replacing them with organic cations. Yin et.al showed that AEMEA reactors can be operated with pure water as anolyte, getting rid of alkali cations completely[28]. They used a quaternary ammonia poly(N-methyl-piperidine-co-p-terphenyl) (QAPPT poly-piperidinium) based polymer electrolyte and observed high faradaic efficiencies towards CO using a spray coated Au catalyst. An important observation from their work is the use of a different functional group, the poly piperidinium cation instead of imadiazolium cation present in sustainion ionomer (See Figure 6.5). These cationic groups might alter the electric field strength around the catalyst, thus changing the CO_2 adsorption at the catalyst surface. Additionally, electrochemical CO_2 RR tests were performed at 60 ^{o}C in this work. Operating at higher temperatures is beneficial not only for better kinetics of CO_2RR and increased ionic conductivity, but also might result in increased movement of these cationic groups in the ionomer around the catalyst, enabling increased CO_2 adsorption owing to altered electric field created by these cations. The role of these cationic groups at these temperatures of 50-60 ^{o}C require further understanding.

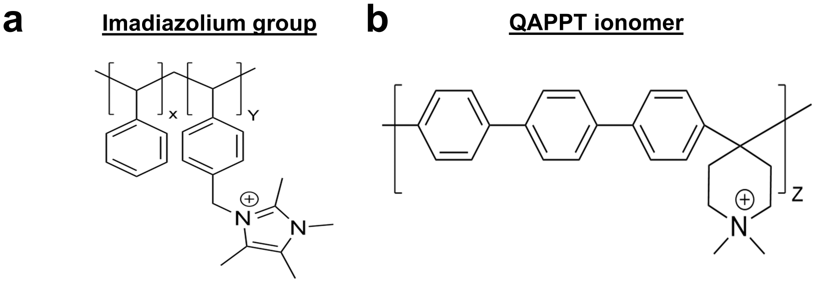

Figure 6.5 : (a) imadiazolium group present in sustainion ionomer, (b) QAPPT cation group used by Yin et. al [28].

Another work by Fan et.al also showed high rate CO_2RR to C_{2+} products by immobilization of cationic functional groups on a Cu surface. On a sputtered Cu catalyst, they spray coated Aemion ionomer containing benzimidazole cationic groups. A high selectivity of 80% was achieved for CO_2RR to C_{2+} products with a stability for 150 hrs at 100 mA/cm^2. However, it is important to note here that a PTFE based GDL was used as porous transport layer in this study. In industrially relevant reactors however, carbon based GDL will have to be used due to proper distribution of current density/potential throughout the electrode area, owing to carbon's better electrical conductivity. It will be interesting to see if similar performance can be achieved using carbon based GDL at higher current densities.

Another important parameter that needs to be emphasized here when designing these organic cationic groups on GDE is the zeta potential. A positive zeta potential of the prepared catalyst layer implies the presence of positively charged groups at the surface, beneficial for CO_2RR. A recent work using immobilized Poly (diallyldimethylammonium chloride)-graphene oxide (PDDA-GO) [29] on a Ag catalyst showed higher CO selectivity in acidic media (0.01 M H_2SO_4 anolyte). In this work, the authors claim that a net cationic effect was achieved on a Ag catalyst due to the net positive zeta potential of PDDA-GO which aids the conversion of CO2 to CO in an MEA electrolyzer devoid of any metal cations. A high FE for CO exceeding 80% across current densities ranging from 100 to 200 mA cm^{-2} was obtained. Such works show great promise for advancing pure water fed CO_2 electrolyzers and more efforts in this direction are essential for the field to move forward.

Finally, from a performance perspective, a recent study by Moore et.al [30] clearly showed that bringing down the electrolyzer energy requirements by reducing full cell voltage is the most important metric affecting overall costs as compared to other energy requirements like gas separation owing to lower single pass conversion efficiencies. Considering this aspect, operating at temperatures of 50-60 ^{o} C with some alkali cation concentrations (Cs^+ or K^+) in the anolyte will still be useful to bring down the overall cell voltage. Hence, it would be interesting to see if these organic cation groups could replace the role of alkali cations to see in future works, and provide very similar performance in terms of partial current density, cell voltage and long-term stability.

REFERENCES

[1] D. A. Salvatore, C. M. Gabardo, A. Reyes, C. P. O'Brien, S. Holdcroft, P. Pintauro, B. Bahar, M. Hickner, C. Bae, D. Sinton, *et al.* “Designing anion exchange membranes for CO2 electrolysers”. In: *Nature Energy* 6.4 (2021), pp. 339–348.

[2] E. W. Lees, B. A. Mowbray, F. G. Parlane, and C. P. Berlinguette. “Gas diffusion electrodes and membranes for CO2 reduction electrolysers”. In: *Nature Reviews Materials* 7.1 (2022), pp. 55–64.

[3] L.-C. Weng, A. T. Bell, and A. Z. Weber. “A systematic analysis of Cu-based membrane-electrode assemblies for CO 2 reduction through multiphysics simulation”. In: *Energy & Environmental Science* 13.10 (2020), pp. 3592–3606.

[4] M. G. Kibria, J. P. Edwards, C. M. Gabardo, C.-T. Dinh, A. Seifitokaldani, D. Sinton, and E. H. Sargent. “Electrochemical CO2 reduction into chemical feedstocks: from mechanistic electrocatalysis models to system design”. In: *Advanced Materials* 31.31 (2019), p. 1807166.

[5] I. E. Stephens, K. Chan, A. Bagger, S. W. Boettcher, J. Bonin, E. Boutin, A. K. Buckley, R. Buonsanti, E. R. Cave, X. Chang, *et al.* “2022 roadmap on low temperature electrochemical CO2 reduction”. In: *Journal of Physics: Energy* 4.4 (2022), p. 042003.

[6] J. A. Rabinowitz and M. W. Kanan. “The future of low-temperature carbon dioxide electrolysis depends on solving one basic problem”. In: *Nature Communications* 11.1 (2020), p. 5231.

[7] B. Endrődi, E. Kecsenovity, A. Samu, F. Darvas, R. Jones, V. Török, A. Danyi, and C. Janáky. “Multilayer electrolyzer stack converts carbon dioxide to gas products at high pressure with high efficiency”. In: *ACS energy letters* 4.7 (2019), pp. 1770–1777.

[8] M. Sassenburg, M. Kelly, S. **Subramanian**, W. A. Smith, and T. Burdyny. “Zero-gap electrochemical CO_2 reduction cells: challenges and operational strategies for prevention of salt precipitation”. In: *ACS Energy Letters* 8.1 (2022), pp. 321–331.

[9] J. Disch, L. Bohn, L. Metzler, and S. Vierrath. “Strategies for the mitigation of salt precipitation in zero-gap CO 2 electrolyzers producing CO”. In: *Journal of Materials Chemistry A* (2023).

[10] E. R. Cofell, U. O. Nwabara, S. S. Bhargava, D. E. Henckel, and P. J. Kenis. “Investigation of electrolyte-dependent carbonate formation on gas diffusion electrodes for CO2 electrolysis”. In: *ACS Applied Materials & Interfaces* 13.13 (2021), pp. 15132–15142.

[11] Y. Xu, J. P. Edwards, S. Liu, R. K. Miao, J. E. Huang, C. M. Gabardo, C. P. O'Brien, J. Li, E. H. Sargent, and D. Sinton. "Self-cleaning CO2 reduction systems: unsteady electrochemical forcing enables stability". In: *ACS Energy Letters* 6.2 (2021), pp. 809–815.

[12] B. Endrődi, A. Samu, E. Kecsenovity, T. Halmágyi, D. Sebők, and C. Janáky. "Operando cathode activation with alkali metal cations for high current density operation of water-fed zero-gap carbon dioxide electrolysers". In: *Nature energy* 6.4 (2021), pp. 439–448.

[13] M. C. Monteiro, F. Dattila, B. Hagedoorn, R. García-Muelas, N. López, and M. T. Koper. "Absence of CO2 electroreduction on copper, gold and silver electrodes without metal cations in solution". In: *Nature Catalysis* 4.8 (2021), pp. 654–662.

[14] G. A. El-Nagar, F. Haun, S. Gupta, S. Stojkovikj, and M. T. Mayer. "Unintended cation crossover influences CO2 reduction selectivity in Cu-based zero-gap electrolysers". In: *Nature Communications* 14.1 (2023), p. 2062.

[15] A. Murata and Y. Hori. "Product selectivity affected by cationic species in electrochemical reduction of CO2 and CO at a Cu electrode". In: *Bulletin of the Chemical Society of Japan* 64.1 (1991), pp. 123–127.

[16] S. Y. Lee, J. Kim, G. Bak, E. Lee, D. Kim, S. Yoo, J. Kim, H. Yun, and Y. J. Hwang. "Probing Cation Effects on* CO Intermediates from Electroreduction of CO2 through Operando Raman Spectroscopy". In: *Journal of the American Chemical Society* 145.42 (2023), pp. 23068–23075.

[17] J. E. Huang, F. Li, A. Ozden, A. Sedighian Rasouli, F. P. García de Arquer, S. Liu, S. Zhang, M. Luo, X. Wang, Y. Lum, *et al.* "CO2 electrolysis to multicarbon products in strong acid". In: *Science* 372.6546 (2021), pp. 1074–1078.

[18] R. B. Sandberg, J. H. Montoya, K. Chan, and J. K. Nørskov. "CO-CO coupling on Cu facets: Coverage, strain and field effects". In: *Surface Science* 654 (2016), pp. 56–62.

[19] X. Chang, J. Li, H. Xiong, H. Zhang, Y. Xu, H. Xiao, Q. Lu, and B. Xu. "C-C coupling is unlikely to be the rate-determining step in the formation of C2+ products in the copper-catalyzed electrochemical reduction of CO". In: *Angewandte Chemie International Edition* 61.2 (2022), e202111167.

[20] S. Garg, C. A. G. Rodriguez, T. E. Rufford, J. R. Varcoe, and B. Seger. "How membrane characteristics influence the performance of CO 2 and CO electrolysis". In: *Energy & Environmental Science* 15.11 (2022), pp. 4440–4469.

[21] K. Khoiruddin, D. Ariono, S. Subagjo, and I. G. Wenten. "The effect of heterogeneity in ion-exchange membrane structure on Donnan Exclusion". In: *Journal of Physics: Conference Series*. Vol. 1090. 1. IOP Publishing. 2018, p. 012045.

[22] N. Kimura, H. Matsumoto, Y. Konosu, R. Yamamoto, M. Minagawa, and A. Tanioka. “Membrane potential across anion-exchange membranes in acidic solution system”. In: *Journal of colloid and interface science* 286.1 (2005), pp. 288–293.

[23] T. Mohammadi and M. Skyllas-Kazacos. “Characterisation of novel composite membrane for redox flow battery applications”. In: *Journal of Membrane Science* 98.1-2 (1995), pp. 77–87.

[24] Y. Ji, H. Luo, and G. M. Geise. “Effects of fixed charge group physicochemistry on anion exchange membrane permselectivity and ion transport”. In: *Physical Chemistry Chemical Physics* 22.14 (2020), pp. 7283–7293.

[25] D. Kitto and J. Kamcev. “The need for ion-exchange membranes with high charge densities”. In: *Journal of Membrane Science* (2023), p. 121608.

[26] J. Kamcev, C. M. Doherty, K. P. Lopez, A. J. Hill, D. R. Paul, and B. D. Freeman. “Effect of fixed charge group concentration on salt permeability and diffusion coefficients in ion exchange membranes”. In: *Journal of Membrane Science* 566 (2018), pp. 307–316.

[27] B. Chen, P. Mardle, and S. Holdcroft. “Probing the effect of ionomer swelling on the stability of anion exchange membrane water electrolyzers”. In: *Journal of Power Sources* 550 (2022), p. 232134.

[28] Z. Yin, H. Peng, X. Wei, H. Zhou, J. Gong, M. Huai, L. Xiao, G. Wang, J. Lu, and L. Zhuang. “An alkaline polymer electrolyte CO 2 electrolyzer operated with pure water”. In: *Energy & Environmental Science* 12.8 (2019), pp. 2455–2462.

[29] J. Fan, B. Pan, J. Wu, C. Shao, Z. Wen, Y. Yan, Y. Wang, and Y. Li. “Immobilized Tetraalkylammonium Cations Enable Metal-free CO2 Electroreduction in Acid and Pure Water”. In: *Angewandte Chemie* (), e202317828.

[30] T. Moore, D. I. Oyarzun, W. Li, T. Y. Lin, M. Goldman, A. A. Wong, S. A. Jaffer, A. Sarkar, S. E. Baker, E. B. Duoss, *et al.* “Electrolyzer energy dominates separation costs in state-of-the-art CO2 electrolyzers: Implications for single-pass CO2 utilization”. In: *Joule* 7.4 (2023), pp. 782–796.

7

OUTLOOK ON FUTURE RESEARCH

In this chapter, I briefly discuss the challenges with AEM based CO_2 electrolyzers and offer future perspectives on scaling up CO_2 electrolysis with some recent developments in the field.

7.1. CHALLENGES WITH AEM BASED CO_2 ELECTROLYZERS

While this dissertation explored spatial effects in anion exchange membrane electrode assembly (AEMEA) CO_2 electrolyzers, significant challenges due to long term stability and costs of materials required for the electrolyzer makes one question the ideal reactor design choice for commercialization of this technology. To get more insights into this question, I briefly discuss the main technical challenges with AEMEA reactors in the following section.

7.1.1. STABILITY OF CARBON BASED GDL

The first challenge associated with AEMEA reactors is the stability of carbon based gas diffusion electrodes (GDE), that are affected by the precipitation of (bi) carbonate salts at the cathode side and electrolyte flooding at higher current densities. Flooding of GDE is primarily attributed to the gradual loss of hydrophobicity of the microporous layer of carbon GDL during operation[1]. Given that water serves as a reactant for CO_2 reduction reactions (CO_2RR), and an excess of water can potentially cause flooding, it becomes crucial to maintain proper water management on the cathode side of the reactor for ensuring a stable operation. In addition, (bi) carbonate precipitation at the cathode side is also shown to be a factor that accelerates electrolyte flooding in AEMEA reactors [2–4]. While recent studies have shown promising strategies for mitigating or avoiding precipitation[5, 6], very few reports have shown stability for >1000 hrs of operation[7, 8]. More research into long term stability of AEMEA systems are required with the use of pure water or Cesium salt anolytes as discussed in Chapter 6.

In addition, proper choice of carbon based GDE and flow field designs should be used as discussed in chapter 4. As reactors are scaled up, larger variations in reactant concentrations, pressure drop and temperatures will arise and GDE properties such as porosity and gas permeability will affect mass transport of reactants reaching the catalyst surface. This is where the knowledge from a vast number of works from PEM fuels cells and redox flow batteries can be useful for better design of GDE and flow field designs in CO_2 electrolyzers.

7.1.2. IRIDIUM SCARCITY CHALLENGE

The second challange that exists in AEM based CO_2 electrolyzers even if long term stability is achieved is the requirement of Iridium (Ir) as the anode material for the anodic oxygen evolution reaction. Iridium scarcity is a well known problem and the growing need for iridium, especially in emerging technologies such as PEM fuel cells and electrolyzers, gives rise to worries about its long-term sustainability and the possibility of future scarcities[9–12]. Christine et. al[13] recently performed an analysis on Ir scarcity for PEM water electrolysis technology and concluded that establishing an efficient closed-loop recycling system and simultaneously decreasing the catalyst loading in proton exchange membrane water electrolysis (PEMWE) cells will reduce the overall demand for materials. In addition, more initiatives are currently in progress to create alternative materials or enhance recycling techniques for products containing iridium.

ALTERNATE CATALYSTS FOR OER

Finding alternate catalysts for iridium for oxygen evolution reaction (OER) has been a decades long research area and many reports have shown alloying two different metals for obtaining OER rates similar to Ir [14–16]. Wu et. al recently reported a Nickel stabilized Ruthenium dioxide (Ni-RuO_2) as catalyst for OER in acidic media and reported > 1000 h stability at 200 mA/cm^2[17]. Another work by Chatti et.al [18] used mixed metal oxides made from dissolved cobalt, lead and iron precursors for similar acidic OER at 500 mA/cm^2. These works show great promise for using non-Ir based anodes for acidic OER which will then be an attractive choice for the anode side of an AEMEA CO_2 electrolyzer. Importantly, this knowledge on non-Ir based anode catalysts in the PEM electrolysis field should be translated to AEMEA CO_2 electrolysis and tested at industrially relevant conditions for overcoming this major challenge.

ALTERNATE ANODE REACTIONS

One of the other strategies that has seen interest in the past few years for overcoming the Ir scarcity challenge is replacing OER with an alternate anode reaction. In CO_2 electrolyzers, a major part of energy requirement comes from the anode side due to the higher redox potential for OER *(1.23 V vs. RHE)*. Alternate anode reactions such as glycerol oxidation on Pt catalysts have been reported to be an attractive choice due to the lower thermodynamic potentials for this reaction *(0.05 vs. RHE)* [19, 20]. Glycerol oxidation for products such as lactic acid or formic acid have been widely reported on Pt based[21] and Ni based catalysts [22]. Integrating such reactions with CO_2RR not only reduces the full cell voltage, but also provides an additional benefit of eliminating gas separation at the anode side due to the absence of oxygen evolution. [23]. However, challenges associated with stability and oxidation of products from these reactions such as formate pose a challenge for industrial applications [24]. Overall, advancements in the creation of promising anode catalysts and reactions present intriguing possibilities and it would be interesting to see if current challenges can be overcome to directly pair these reactions with CO_2RR at industrially relevant conditions.

7.1.3. DESIGNING CATALYST COATED MEMBRANES

As the full cell voltage of a CO_2 electrolyzer primarily affects the device energy efficiency, the ohmic losses encountered in zero gap AEM based CO_2 electrolyzers has to be minimized. The voltage losses encountered in the reactor stems from overpotentials on the cathode ($E_{cathode}$), anode (E_{anode}) and the membrane (E_{mem}). In particular, the ionic resistance between the AEM and the cathode catalyst layer plays a significant role in the overall cell voltage encountered in the system. This cathode-membrane interfacial resistance can be significantly reduced by directly depositing the catalyst on the membrane. Hensen et.al recently showed the use of catalyst coated membrane (CCM) for AEM based CO_2 electrolyzers and acheived a CO partial current density of 720 mA/cm^2 at 3.55 V, reducing the cathode ohmic resistance by 90%. Importantly, dilute anolyte concentrations were used (<10 mM $KHCO_3$) at these current densities, providing promising conditions for mitigating salt precipitation issues as well, as discussed in previous chapters. In addition, the CCM strategy seemed to work only for specific AEM used in their study (Orion AEM) and failed to provide stable performance for commercially available AEMs such as Sustainion and Piperion membranes. Since, a significant amount of work exists in CCM for AEM based water electrolyzers, it would be interesting to see where this research topic moves forward in the coming years. Overall, designing efficient CCM for AEM based CO_2 electrolyzers will be an important area of research for scale up of this technology.

7.1.4. BPMEA AS AN ALTERNATE REACTOR DESIGN CHOICE

Another topic of interest in CO_2RR that gas gained increased attention in the past few years in the use of bipolar membranes (BPM). BPMs have multiple benefits over AEM electrolyzers such as avoiding product migration and CO_2 crossover (in the form of carbonates) from cathode to anode. The main benefits when operated in reverse bias mode however, lies in the ability to maintain an alkaline pH at the anode side which enables the use of non-platinum group metal (PGM) free catalysts like nickel (Ni) at the anode. The downside is the additional voltage requirement for water dissociation reaction (WDR) within the membrane, however higher CO_2 single pass utilization efficiencies can be obtained owing to CO_2 regeneration from the reaction of protons and (bi) carbonate ions at the cathode.

Xie et.al used a BPMEA system for producing ethylene from Cu at 200 mA/cm^2 with a single pass CO_2 conversion of 78% [25]. The use of a porous PVDF thin buffer layer between the cathode catalyst and CEL of the BPM enabled significant regeneration of CO_2 from carbonate ions and reasonable suppression of HER. Better design of BPM and smart design strategies will be essential in the future to see if BPMEA could replace AEMEA reactors for operating at industrially relevant conditions.

7.1.5. STABILITY OF COPPER BASED CATALYSTS UNDER CO_2RR

One of the major challenges with electrosynthesis of ethylene and ethanol from CO_2RR is the instability of copper (Cu) based catalysts under applied cathodic potentials. Morphological/structural changes of Cu under CO_2RR conditions have been found to be the primary reason for this instability and the presence of Cu^+ species and defects are found to be essential for mitigating this instability during CO_2RR [26, 27]. Since, Cu^+ species is usually absent under higher cathodic potentials, potentiodynamic techniques has become a topic of great interest [28–31] for increasing the lifetime of catalyst.

Obsanjo et.al showed that this pulsing strategy can be used to achieve a stable CO_2RR at 150 mA/cm^2 for 200 hours in a GDE flow cell with 40% selectivity for ethylene [32]. In this work, a PTFE based GDL was used as gas diffusion media, which is effective for resisting electrolyte flooding. In practical application however, periodically changing the electrode polarity from cathodic to anodic conditions, may pose challenges for large-scale electrolyzers where carbon based GDL are necessary owing to its proper current distribution.

Further, the presence of copper oxides and role of Cu^+ species during electrochemical CO_2RR lack consensus [33–35]. However, in pulse CO_2RR, anodic potentials are commonly involved, and thermodynamically, the formation of oxide species is expected. The rate at which these oxides form in relation to the applied pulsed potential remains an unresolved question, with the expectation that future in situ and operando experiments will provide clarity on this issue. Substantial efforts must then be dedicated to advancing our understanding of pulse methods. This will facilitate the effective utilization of pulse methods for achieving stable CO_2 electrolyzer operation.

7.2. WHAT SHOULD WE MAKE OUT OF CO_2?

Finally, after lots of discussion into CO_2RR, an important question that arises is: which CO_2RR product is most suitable for commercialization? The answer to this question is significantly influenced by economic factors, the balance of supply and demand for specific products, and to the prevailing state-of-the-art technologies that affect overall costs and production rates. Table 7.1 presents the market prices (in US dollars per kilogram) of seven CO_2 reduction products based on the study by Jouny et.al [36].

It is interesting to see from Table 7.1 that formic acid, has highest normalized market price (16.1 x 10^3 USD/electron), which is primarily due to the number of electrons needed for its production. However, its annual production is the second lowest, indicating limited industrial use primarily as a preservative and antibacterial agent [37]. On the contrary, methane, widely utilized for power generation and domestic heating, and benefiting from abundant natural gas sources, boasts the highest annual production at 250 million metric tons per year, accompanied by the lowest normalized market price.

In addition, it is also evident that ethylene, methanol, and ethanol emerge as highly sought-after products due to their substantial market capacity and reasonable normalized market prices. These four items play pivotal roles in various industries as chemical precursors, fuel additives, and sources for energy generation. It is important to emphasize here that these conclusions are drawn purely from an economic standpoint and a comprehensive evaluation of the most suitable product for CO_2 electrolysis technology should take into account of emerging breakthroughs, including catalysts, electrochemical reactor design, separation, and storage.

Table 7.1: Market prices and annual global production figures for CO_2RR products.

Product	**Number of electrons (e^-)**	**Market price (USD/kg)**	**Normalized price (USD/e^-) x 10^3**	**Annual global production (Mtonne)**
CO (Syngas)	2	0.06	0.8	150.0
Formic acid	2	0.74	16.1	0.6
Methanol	6	0.58	3.1	110.0
Methane	8	0.18	0.4	250.0
Ethylene	12	1.30	3.0	140.0
Ethanol	12	1.00	3.8	77.0
n-propanol	18	1.43	4.8	0.2

7.3. FUTURE OUTLOOK

Due to current challenges existing in CO_2 electrolyzers, the construction of pilot plants for the widespread implementation of this technology will take several years. This is where the mature thermocatalytic pathway offers a faster route for sustainable hydrocarbon production. A wide variety of industries have already taken this route for direct CO_2 hydrogenation to products such as methanol [38]. For example, the Swedish company Liquid Winds and a Danish company Orsted are working together on the world's first large-scale sustainable e-methanol project using biogenic CO_2 and renewable H_2 produced from water electrolysis. The electrolyser is anticipated to have a capacity of approximately 70 MW and is projected to generate 50,000 tonnes of e-methanol annually. The hydrogen production through electrolysis will be sustained by onshore wind power, while the biogenic CO_2 will be captured from the combined heat and power plant Hörneborgsverket located in Sweden.

In another example, Air Company (based in the US) employs heterogeneous catalysis to perform the hydrogenation of CO_2 to ethanol. The resulting ethanol is of a high purity and suitable for applications in beverages, foods, cosmetics, pharmaceuticals, cleaning products, and fragrances. Green hydrogen for the reaction is also produced by water electrolysis and reacted with the captured CO_2.

When it comes to direct electrochemical CO_2 reduction route, several promising startups are focusing on the development of this technology for ethylene, formic acid, and CO (for syngas) production. Among the companies dedicated towards these products are Dioxycle (Paris), Twelve (US), eChemicles (Hungary) and Avantium (The Netherlands). While it will be interesting to see how their technologies shape up in the upcoming years, the contribution of CO_2 electrolyzers for the much required energy transition cannot yet be ruled out.

REFERENCES

[1] K. Yang, R. Kas, W. A. Smith, and T. Burdyny. “Role of the carbon-based gas diffusion layer on flooding in a gas diffusion electrode cell for electrochemical CO2 reduction”. In: *ACS Energy Letters* 6.1 (2020), pp. 33–40.

[2] A. B. Moss, S. Garg, M. Mirolo, C. A. G. Rodriguez, R. Ilvonen, I. Chorkendorff, J. Drnec, and B. Seger. “In operando investigations of oscillatory water and carbonate effects in MEA-based CO2 electrolysis devices”. In: *Joule* 7.2 (2023), pp. 350–365.

[3] S. Garg, Q. Xu, A. B. Moss, M. Mirolo, W. Deng, I. Chorkendorff, J. Drnec, and B. Seger. “How alkali cations affect salt precipitation and CO 2 electrolysis performance in membrane electrode assembly electrolyzers”. In: *Energy & Environmental Science* 16.4 (2023), pp. 1631–1643.

[4] Y. Kong, H. Hu, M. Liu, Y. Hou, V. Kolivoška, S. Vesztergom, and P. Broekmann. “Visualisation and quantification of flooding phenomena in gas diffusion electrodes used for electrochemical CO2 reduction: A combined EDX/ICP–MS approach”. In: *Journal of Catalysis* 408 (2022), pp. 1–8.

[5] B. Endrődi, A. Samu, E. Kecsenovity, T. Halmágyi, D. Sebők, and C. Janáky. “Operando cathode activation with alkali metal cations for high current density operation of water-fed zero-gap carbon dioxide electrolysers”. In: *Nature energy* 6.4 (2021), pp. 439–448.

[6] M. Sassenburg, M. Kelly, S. **Subramanian**, W. A. Smith, and T. Burdyny. “Zero-gap electrochemical CO_2 reduction cells: challenges and operational strategies for prevention of salt precipitation”. In: *ACS Energy Letters* 8.1 (2022), pp. 321–331.

[7] Z. Liu, H. Yang, R. Kutz, and R. I. Masel. “CO2 electrolysis to CO and O2 at high selectivity, stability and efficiency using sustainion membranes”. In: *Journal of The Electrochemical Society* 165.15 (2018), J3371.

[8] X. She, L. Zhai, Y. Wang, P. Xiong, M. M.-J. Li, T.-S. Wu, M. C. Wong, X. Guo, Z. Xu, H. Li, *et al.* “Pure-water-fed, electrocatalytic CO2 reduction to ethylene beyond 1,000 h stability at 10 A”. In: *Nature Energy* (2024), pp. 1–11.

[9] M. Clapp, C. M. Zalitis, and M. Ryan. “Perspectives on current and future iridium demand and iridium oxide catalysts for PEM water electrolysis”. In: *Catalysis Today* 420 (2023), p. 114140.

[10] R. Riedmayer, B. A. Paren, L. Schofield, Y. Shao-Horn, and D. Mallapragada. “Proton Exchange Membrane Electrolysis Performance Targets for Achieving 2050 Expansion Goals Constrained by Iridium Supply”. In: *Energy & Fuels* (2023).

[11] T. Terlouw, C. Bauer, R. McKenna, and M. Mazzotti. “Large-scale hydrogen production via water electrolysis: a techno-economic and environmental assessment”. In: *Energy & Environmental Science* 15.9 (2022), pp. 3583–3602.

[12] C. Mittelsteadt, E. Sorensen, and Q. Jia. “Ir Strangelove, or How to Learn to Stop Worrying and Love the PEM Water Electrolysis”. In: *Energy & Fuels* 37.17 (2023), pp. 12558–12569.

[13] C. Minke, M. Suermann, B. Bensmann, and R. Hanke-Rauschenbach. “Is iridium demand a potential bottleneck in the realization of large-scale PEM water electrolysis?” In: *international journal of hydrogen energy* 46.46 (2021), pp. 23581–23590.

[14] L. C. Seitz, C. F. Dickens, K. Nishio, Y. Hikita, J. Montoya, A. Doyle, C. Kirk, A. Vojvodic, H. Y. Hwang, J. K. Norskov, *et al.* “A highly active and stable IrO x/SrIrO3 catalyst for the oxygen evolution reaction”. In: *Science* 353.6303 (2016), pp. 1011–1014.

[15] L. An, C. Wei, M. Lu, H. Liu, Y. Chen, G. G. Scherer, A. C. Fisher, P. Xi, Z. J. Xu, and C.-H. Yan. “Recent development of oxygen evolution electrocatalysts in acidic environment”. In: *Advanced Materials* 33.20 (2021), p. 2006328.

[16] J. Song, C. Wei, Z.-F. Huang, C. Liu, L. Zeng, X. Wang, and Z. J. Xu. “A review on fundamentals for designing oxygen evolution electrocatalysts”. In: *Chemical Society Reviews* 49.7 (2020), pp. 2196–2214.

[17] Z.-Y. Wu, F.-Y. Chen, B. Li, S.-W. Yu, Y. Z. Finfrock, D. M. Meira, Q.-Q. Yan, P. Zhu, M.-X. Chen, T.-W. Song, *et al.* “Non-iridium-based electrocatalyst for durable acidic oxygen evolution reaction in proton exchange membrane water electrolysis”. In: *Nature Materials* 22.1 (2023), pp. 100–108.

[18] M. Chatti, J. L. Gardiner, M. Fournier, B. Johannessen, T. Williams, T. R. Gengenbach, N. Pai, C. Nguyen, D. R. MacFarlane, R. K. Hocking, *et al.* “Intrinsically stable in situ generated electrocatalyst for long-term oxidation of acidic water at up to 80 C”. In: *Nature Catalysis* 2.5 (2019), pp. 457–465.

[19] S. Verma, S. Lu, and P. J. Kenis. “Co-electrolysis of CO2 and glycerol as a pathway to carbon chemicals with improved technoeconomics due to low electricity consumption”. In: *Nature Energy* 4.6 (2019), pp. 466–474.

[20] H. Yadegari, A. Ozden, T. Alkayyali, V. Soni, A. Thevenon, A. Rosas-Hernández, T. Agapie, J. C. Peters, E. H. Sargent, and D. Sinton. “Glycerol oxidation pairs with carbon monoxide reduction for low-voltage generation of C2 and C3 product streams”. In: *ACS Energy Letters* 6.10 (2021), pp. 3538–3544.

[21] S. Carrettin, P. McMorn, P. Johnston, K. Griffin, C. J. Kiely, and G. J. Hutchings. “Oxidation of glycerol using supported Pt, Pd and Au catalysts”. In: *Physical Chemistry Chemical Physics* 5.6 (2003), pp. 1329–1336.

[22] V. Oliveira, C. Morais, K. Servat, T. Napporn, G. Tremiliosi-Filho, and K. B. Kokoh. “Glycerol oxidation on nickel based nanocatalysts in alkaline medium–Identification of the reaction products”. In: *Journal of Electroanalytical Chemistry* 703 (2013), pp. 56–62.

[23] K. Xie, A. Ozden, R. K. Miao, Y. Li, D. Sinton, and E. H. Sargent. “Eliminating the need for anodic gas separation in CO2 electroreduction systems via liquid-to-liquid anodic upgrading”. In: *Nature communications* 13.1 (2022), p. 3070.

[24] B. van den Bosch, B. Rawls, M. B. Brands, C. Koopman, M. F. Phillips, M. C. Figueiredo, and G.-J. M. Gruter. “Formate Over-Oxidation Limits Industrialization of Glycerol Oxidation Paired with Carbon Dioxide Reduction to Formate”. In: *ChemPlusChem* 88.4 (2023), e202300112.

[25] K. Xie, R. K. Miao, A. Ozden, S. Liu, Z. Chen, C.-T. Dinh, J. E. Huang, Q. Xu, C. M. Gabardo, G. Lee, *et al.* “Bipolar membrane electrolyzers enable high single-pass CO2 electroreduction to multicarbon products”. In: *Nature communications* 13.1 (2022), p. 3609.

[26] J. Vavra, G. P. Ramona, F. Dattila, A. Kormányos, T. Priamushko, P. P. Albertini, A. Loiudice, S. Cherevko, N. Lopéz, and R. Buonsanti. “Solution-based Cu+ transient species mediate the reconstruction of copper electrocatalysts for CO2 reduction”. In: *Nature Catalysis* (2024), pp. 1–9.

[27] R. M. Arán-Ais, F. Scholten, S. Kunze, R. Rizo, and B. Roldan Cuenya. “The role of in situ generated morphological motifs and Cu (i) species in C2+ product selectivity during CO2 pulsed electroreduction”. In: *Nature Energy* 5.4 (2020), pp. 317–325.

[28] C. A. Obasanjo, G. Gao, B. N. Khiarak, T. H. Pham, J. Crane, and C.-T. Dinh. “Progress and perspectives of pulse electrolysis for stable electrochemical carbon dioxide reduction”. In: *Energy & Fuels* 37.18 (2023), pp. 13601–13623.

[29] C. Kim, L.-C. Weng, and A. T. Bell. “Impact of pulsed electrochemical reduction of CO2 on the formation of C2+ products over Cu”. In: *ACS Catalysis* 10.21 (2020), pp. 12403–12413.

[30] R. Casebolt, K. Levine, J. Suntivich, and T. Hanrath. “Pulse check: Potential opportunities in pulsed electrochemical CO2 reduction”. In: *Joule* 5.8 (2021), pp. 1987–2026.

[31] C. A. Obasanjo, G. Gao, J. Crane, V. Golovanova, F. P. García de Arquer, and C.-T. Dinh. “High-rate and selective conversion of CO2 from aqueous solutions to hydrocarbons”. In: *Nature Communications* 14.1 (2023), p. 3176.

[32] T. N. Nguyen, Z. Chen, A. S. Zeraati, H. S. Shiran, S. M. Sadaf, M. G. Kibria, E. H. Sargent, and C.-T. Dinh. “Catalyst regeneration via chemical oxidation enables long-term electrochemical carbon dioxide reduction”. In: *Journal of the American Chemical Society* 144.29 (2022), pp. 13254–13265.

[33] H. Xiao, W. A. Goddard III, T. Cheng, and Y. Liu. “Cu metal embedded in oxidized matrix catalyst to promote CO2 activation and CO dimerization for electrochemical reduction of CO2”. In: *Proceedings of the National Academy of Sciences* 114.26 (2017), pp. 6685–6688.

[34] X. Yuan, S. Chen, D. Cheng, L. Li, W. Zhu, D. Zhong, Z.-J. Zhao, J. Li, T. Wang, and J. Gong. “Controllable Cu0-Cu+ sites for electrocatalytic reduction of carbon dioxide”. In: *Angewandte Chemie* 133.28 (2021), pp. 15472–15475.

[35] P.-P. Yang, X.-L. Zhang, F.-Y. Gao, Y.-R. Zheng, Z.-Z. Niu, X. Yu, R. Liu, Z.-Z. Wu, S. Qin, L.-P. Chi, *et al.* “Protecting copper oxidation state via intermediate confinement for selective CO2 electroreduction to C2+ fuels”. In: *Journal of the American Chemical Society* 142.13 (2020), pp. 6400–6408.

[36] M. Jouny, W. Luc, and F. Jiao. “General techno-economic analysis of CO2 electrolysis systems”. In: *Industrial & Engineering Chemistry Research* 57.6 (2018), pp. 2165–2177.

[37] M. Pérez-Fortes, J. C. Schöneberger, A. Boulamanti, G. Harrison, and E. Tzimas. “Formic acid synthesis using CO2 as raw material: Techno-economic and environmental evaluation and market potential”. In: *international journal of hydrogen energy* 41.37 (2016), pp. 16444–16462.

[38] H. Guzman, F. Salomone, E. Batuecas, T. Tommasi, N. Russo, S. Bensaid, and S. Hernandez. “How to make sustainable CO2 conversion to Methanol: Thermocatalytic versus electrocatalytic technology”. In: *Chemical Engineering Journal* 417 (2021), p. 127973.

SUMMARY

Carbon dioxide (CO_2) electrolysis is an attractive technology for the production of value-added products and hydrocarbons, establishing a route for leveraging renewable energy sources in the synthesis of fuels and chemicals. Considerable progress has been made in the past decade in advancing CO_2 electrolyzers towards commercial scales, however major challenges remain for achieving practical feasibility.

Among the various gas diffusion electrode (GDE) architectures reported for CO_2 electrolysis, the membrane electrode assembly (MEA) reactor configuration seems to be promising for scale up of the technology. While significant improvements in reaction rates and product selectivity have now been achieved, there is lack of knowledge on spatial effects occurring inside the reactor, due to conventional ‘black box’ measurement protocols and challenges with measuring local effects during reaction. In this thesis, we demonstrate that spatial variations in reactant concentrations can lead to corresponding variations in faradaic efficiency that conventional ’black box’ measurement procedures cannot capture. Using a combination of galvanostatic experiments and a 3D mass transport and fluid flow model, we show that these spatial variations can be predicted which aids in formulating design rules for scaling up these reactors.

Silver (Ag) catalyst shows promising performance for the electrochemical conversion of CO_2 to CO, however operating conditions specifically the inlet CO_2 flowrate is known to affect CO selectivity, by altering the local CO_2 concentration. Increasing the inlet CO_2 flowrate not only increases CO selectivity but also decreases single pass CO_2 utilization significantly, leading to a trade-off in CO_2 utilization and product selectivity. These trade-offs were measured and quantified for a 5 cm^2 MEA reactor and good agreements with the empirical transport model and experimental results were obtained.

Additionally, another operating parameter that hasn’t been studied is the gas flow field design at the cathode which distributes the reactants and transports products away from the gas diffusion electrode. We used knowledge from PEM fuel cells and water electrolyzers and showed for the first that gas flow field design can have significant effects on spatial reactant distribution, product selectivity and stability of GDE due to electrolyte flooding and salt precipitation at the cathode. Generating a higher pressure drop at the cathode side was found to be beneficial for resisting electrolyte flooding at higher current densities and future works should investigate how these gas flow field designs could further be manipulated for improving performance further. The important takeaway here is that ‘utilization’ of a catalyst on GDE is not solely affected by the catalyst preparation, but also by the design of system components such as the GDE, gas flow field design and operating conditions.

Further, copper (Cu) is one of the most attractive catalysts for CO_2 electrolysis due to its unique ability to produce multi-carbon products such as ethylene and ethanol. Modulating inlet CO_2 flowrates have previously been shown to affect multi-carbon product selectivities but a proper understanding of mass transport effects was lacking. In this thesis, we showed that under CO_2 depleted conditions, a subset of the reactor was performing CO electrolysis that significantly increased multi-carbon production rates, maximizing 'CO utilization'. The reactant residence time then plays a key role in affecting product selectivity which can also be altered by changing the gas flow field design at the cathode. With the help of mass spectroscopy, we showed that the reactant residence time changes significantly depending on the gas flow field design (serpentine, parallel and interdigitated). Importantly, the differences in residence time under varying flowrates and flow fields occur in the liquid phase of the reactor, further confirming that the reaction in liquid phase is rate limiting. Overall, these design strategies will play an important role when electrolyzers are scaled to larger areas and proper designs must be used for maximizing the production of hydrocarbons such as ethylene and ethanol from CO_2.

Finally, trade-offs associated with cell voltage, salt precipitation and cation crossover in anion exchange membrane electrode assemblies are another important factor to be considered when for scale up of this technology. Numerous studies on the role of cations for electrochemical CO_2 reduction were already reported. We showed that such effects are present even in zero gap MEA reactors where alkali metal cation crossover from the anode to cathode affects product distribution for Ag and Cu catalysts. With recent reports on replacing alkali cations by using pure water as anolyte and organic cations within the catalyst layer seems be a promising strategy to overcome stability issues associated with salt precipitation. It will be interesting to see how this research area moves forward, but overall, the role of CO_2 electrolyzers for the much required energy transition cannot yet be ruled out.

SAMENVATTING

Elektrolyse van kooldioxide (CO_2) is een aantrekkelijke technologie voor de-carbonisatie, het bieden van een duurzame route om producten met toegevoegde waarde en koolwaterstoffen te synthetiseren en het opzetten van een route voor het gebruik van hernieuwbare energiebronnen bij de synthese van brandstoffen en chemicaliën. Er is de afgelopen tien jaar aanzienlijke vooruitgang geboekt bij het bevorderen van CO_2-elektrolyzers naar commerciële schalen, maar er blijven grote uitdagingen bestaan om praktische haalbaarheid te bereiken.

Van de verschillende gasdiffusie-elektrode (GDE) -architecturen die zijn gerapporteerd voor CO_2-elektrolyse, lijkt de membraan-elektrodeassemblage (MEA) -reactorconfiguratie veelbelovend voor opschaling van de technologie. Hoewel er nu aanzienlijke verbeteringen in reactiesnelheden en productselectiviteit zijn bereikt, ontbreekt het aan kennis over ruimtelijke effecten in de reactor, ten gevolge van conventionele ‘ black box ’ meetprotocollen en uitdagingen bij het meten van lokale effecten tijdens reactie. In dit proefschrift laten we zien dat ruimtelijke variaties in reactant concentraties kunnen leiden tot overeenkomstige variaties in faradaïsche efficiëntie die conventionele ’black box’-meetprocedures niet kunnen vastleggen. Gebruikmakend van een combinatie van galvanostatische experimenten en een 3D-massatransport- en vloeistofstroommodel, laten we zien dat deze ruimtelijke variaties kunnen worden voorspeld, wat zal helpen bij het formuleren van ontwerpregels voor het opschalen van deze reactoren.

Een zilver (Ag) katalysator vertoont veelbelovende activiteit voor de elektrochemische omzetting van CO_2 in CO, maar het is bekend dat operatieve omstandigheden, met name het inlaat-CO2-stroomsnelheid, de CO-selectiviteit beïnvloeden, door de lokale CO2-concentratie te wijzigen. Het verhogen van het inlaat-CO_2-stroomsnelheid verhoogt niet alleen de CO-selectiviteit, maar vermindert ook aanzienlijk het CO_2-gebruik met enkelvoudige doorgang, wat leidt tot een afweging van het CO_2-gebruik en de productselectiviteit. Deze afwegingen werden gemeten en gekwantificeerd voor een MEA-reactor van 5 cm^2 en er werden goede overeenkomsten met het empirische transportmodel en experimentele resultaten verkregen.

Bovendien is een andere operationele parameter die niet is onderzocht het gasstromingsveldontwerp aan de kathode, dat de reactanten verdeelt en producten wegvoert van de gasdiffusie-elektrode. We gebruikten kennis van PEM-brandstofcellen en waterelektrolysatoren en toonden voor het eerst dat gasstromingsveldontwerp aanzienlijke effecten kan hebben op de ruimtelijke reactantverdeling, productselectiviteit en stabiliteit van GDE als gevolg van elektrolytoverstromingen en zoutneerslag aan de kathode. Het genereren van een hogere drukval aan de kathodezijde bleek gunstig voor het weerstaan van elektrolytoverstromingen bij hogere stroomdichtheden en toekomstig werk zou moeten onderzoeken hoe deze gasstromingsveldontwerpen verder zouden kunnen gaan worden gemanipuleerd om de prestaties verder te verbeteren. De belangrijkste boodschap hier is dat ‘ gebruik ’ van een katalysator op GDE niet alleen wordt beïnvloed door de katalysatorvoorbereiding, maar ook door het ontwerp van systeemcomponenten zoals de GDE, ontwerp van het gasstroomveld en operationele condities.

Verder is koper (Cu) een van de meest aantrekkelijke katalysatoren voor CO_2-elektrolyse vanwege het unieke vermogen om C_{2+} producten zoals ethyleen en ethanol te produceren. Het is eerder aangetoond dat het moduleren van inlaat-CO_2-stroomsnelheden de product selectiviteiten met meerdere koolstofproducten beïnvloedt, maar een goed begrip van de effecten van massatransport ontbrak. In dit proefschrift toonden we aan dat onder CO_2 arme omstandigheden een subset van de reactor CO-elektrolyse uitvoerde die de productiesnelheden van C_{2+} producten aanzienlijk verhoogde, waardoor het ‘ CO-gebruik ’ werd gemaximaliseerd. De reactanten verblijftijd speelt dan een sleutelrol bij het beïnvloeden van de productselectiviteit, die ook kan worden verandert door het gasstromingsveldontwerp aan de kathode te wijzigen. Met behulp van ex-situ massaspectroscopie hebben we aangetoond dat de reactanten verblijftijd aanzienlijk verandert, afhankelijk van het gasstromingsveldontwerp (serpentine, parallel en interdigitated). Belangrijk is dat de verschillen in verblijftijd onder verschillende stroomsnelheden en stroomvelden optreden in de vloeibare fase van de reactor, wat verder bevestigt dat de reactie in de vloeibare fase snelheid begrenzend is. Over het algemeen, zullen deze ontwerpstrategieën een belangrijke rol spelen wanneer elektrolyzers naar grotere gebieden worden geschaald en de juiste ontwerpen moeten worden gebruikt om de productie van koolwaterstoffen zoals ethyleen en ethanol uit CO_2 te maximaliseren.

Ten slotte zijn afwegingen in verband met cel voltage, zoutneerslag en kationen crossover in anionen-uitwisselingsmembraan-elektrodeassemblage, andere belangrijke factoren waarmee rekening moet worden gehouden bij het opschalen van deze technologie. Talrijke studies over de rol van kationen voor elektrochemische CO_2-reductie zijn al gerapporteerd. We hebben aangetoond dat dergelijke effecten zelfs aanwezig zijn in MEA-reactoren met geen tussenruimte, waar de crossover van alkalimetaalkation van de anode naar de kathode de productverdeling voor Ag- en Cu-katalysatoren beïnvloedt. Met recente rapporten over het vervangen van alkalikationen door zuiver water te gebruiken als anoliet en organische kationen in de katalysatorlaag, lijkt het een veelbelovende strategie om stabiliteitsproblemen in verband met zoutneerslag te overwinnen. Het zal interessant zijn om te zien hoe dit onderzoeksgebied vooruitgaat, maar over het algemeen kan de rol van CO_2-elektrolysatoren voor de noodzakelijke energietransitie nog niet worden uitgesloten.

ACKNOWLEDGEMENTS

Hey reader! Are you coming straight to this page after reading my propositions? Come on! Do read my chapters. Honestly, it feels like I came to the Netherlands just yesterday. And here I am, submitting a 150-page document with some science stuff. It's over. The PhD journey. This is definitely one of the important phases of my life. Not because of the scientific work itself, but because of the wonderful, smart and kind scientific souls with whom I have worked and interacted with in the last 4 years. Without all these people, the journey would not have been memorable. In no particular order (flat hierarchy right?), I would like to thank the following people who have made my PhD a memorable experience:

Prof. Burdyny: I am uncertain about the number of words I can use to express my gratitude, Tom. I will always be grateful to you for hiring me as your first official PhD student. Moving to Delft and the Netherlands was possible due to the trust you had when you hired me. Coming to the PhD journey. As a new group at TU Delft working on scaling up CO_2 electrolyzers, it was both fun and challenging to setup and work with new equipment in the lab and every day was a new learning experience. When COVID stuck in 2020, I remember my first project work where I was playing around with building mass transport models in COMSOL Multiphysics. I still remember the curiosity and the inputs you gave during my learning process, that helped me learn a bit of mass transport modelling.

Thereafter, I could clearly see that you were not only a PI who cared about group's research output unlike many PIs in the academic world, but you are someone who makes sure that every researcher was going in the right direction. You showed us that you are both a great scientist and a lab manager, something that very few PIs have in today's world. Everyone joining our lab could feel within a few months that they were at the right place. When you received the best lecturer of the year award, starting grant award and other accolades, it was both a proud feeling as well as inspiring to see the growth of a leader. I have learnt so many things from you both scientifically and personally and I will make sure to contribute what I have learnt to other people with whom I will work in the near future. I have no doubt that the Burdyny Energy lab will continue to make great scientific contributions in the future. I would also like to thank Sarah for hosting us dinner at your place along with you during Christmas time.

Bernard: Thank you for being not just my promotor but also for some great discussions during my PhD. Your constant feedback and critical comments during presentations and monthly meetings made me improve my critical thinking skills and I believe I have grown into a better researcher. Your constant stress on 'Helicopter view' and 'But why?' questions helped me view science from a completely different perspective. I always enjoyed your critical questions and discussions during the MECS group. **Fokko**: Thank you for some great scientific discussions during the MECS group meetings.

The PhDs and Postdocs with whom I have had the privilege of working with. **Hugo**: We started as a PhD student just 1.5 months apart. It was great to see you grow over the years and I learnt so many things from you. Assertiveness and self-confidence are two traits that I have seen in you and was impressed with. Travelling together to summer schools and various conferences was a lot of fun and thanks for making it memorable with lots of scientific and non-scientific discussions. **Erdem**: See the spray coating setup in our lab folks? It was this guy who first bought it to our labs. It was great learning and working with you in the first two years of my PhD. Apart from scientific discussions, you made sure we had lots of fun in Barcelona during the MATSUS Conference and other meetups in Delft. It is great to see your constant growth, currently in industry. I am sure you will continue to shine in industry.

Aaron: The best scientific discussions I have had were with you Aaron. Your sharp scientific criticism during discussions helped me become more critical in science and you played an important role in me becoming a better researcher. I am happy to see you become a PI and start your own research group in Melbourne. Thanks to Nikki and you for hosting us for dinner in Delft and for the fun conversations we had during those times. **Kailun**: When I first joined the lab, you were the first person to show me how to use the PTFE cells. After that, working with you and discussing science helped me a lot to grow myself as a researcher. Thank you for being a great colleague.

Maryam: Professor! It was great sitting next to you in the office for over a year and having some great conversations. I have never seen someone so passionate and hardworking in the labs and your hard work and dedication towards science inspired everyone in our labs. I wa not surprised when you were offered a got a postdoc position at MIT in the US. I am sure that you will succeed in finding a PI position in academia soon. **Mark**: Hey sassy boy! You are a unique personality. Every research group should have someone like you. They say laughter is the best medicine. To every PI out there, make sure to hire a 'Mark' in your group for a bit of laughter within the group. Apart from this, it was great working with you on the salt precipitation perspective article. I am proud to say that we both made lots of salt in the gas flow channels of the MEA cells. **Sanjana**: Although you were working at Shell during your PhD, I remember you were the first one showing me how to use the MEA cells and the membranes when I started in the lab. Thank you for being kind and helpful for everyone in the lab and I am glad to see you shine in industry after your PhD.

Marijn: Thanks for introducing me to bipolar membranes and involving me in one of your projects. It was great working with you and to see how well you organized your projects, was a great learning. **Anirudh**: Thanks for being a great colleague during your PhD days and its great to work with you again in the HYeT project. **Davide**: Thank you for being a great colleague and for being a great drummer during our music sessions at

X. Should probably do more of those sessions.

Georgia and Diana: Thanks for all those great conversations during the course of your PhD and in the sputter labs. It was inspiring to see the dedication to work you both had during work. Thanks also for inviting me to Eindhoven for a random weekend chat. It was great having you as colleagues and I hope to see you guys along sometime. **Dylan and Peter**: Thanks for all the wonderful conversations during coffee breaks and during the borrel and for the Dutch translation of my summary Peter. Wish you both a great success in all your future endeavours. **Mark and Pranav**: Thanks to you both for some fun chats during coffee breaks and teaching me a bit about batteries.

Joost and Herman: A very important part of MECS group are these two technicians who makes life easier for all researchers in the group. Thank you Joost for being a great support during the course of my PhD, right from installing the GCs and mass flow meters in the labs to making ordering chemicals easier for us. Herman: thanks for the sputtering instrument which made our catalyst preparation easier and importantly very reproducible. Thank you both for being so kind to all researchers in training and handling of the instruments in the lab. Additionally, thank you for so many great conversations on various topics during coffee breaks and borrel time. To other technicians: Thank you **Duco** for being of great help with SEM and **Xiaohui** for XRD. **Bart** for not just helping with XPS, but also for some fun chats at the ChemE coffee corner. **Roos**: Thank you very much for being of great help during many occasions and always open to help with all the financial and office related stuff.

Coming to the newbies (or next-gen.) in our group. **Jesse Kok**: Thank you, Mr. Kok, for being a nice colleague and for great conversations in the office. It was great to have had supervised you during your Master thesis and see you grow as a PhD in our group. **Jasper**: Thanks for all the great time discussing some great science, for the random scientific talks during breaks and some bouldering in Delft. Oh! And thanks for the fun conversations during our Conference in Malaga. I wish you the best in your postdoctoral research work. **Nick, Henry, Gerard**: It is great to see you guys being motivated all the time and thank you all for both scientific and non-scientific discussions. I am sure you will push the progress of scientific work from our group even better in the coming years. **Tiange**: Thanks Tiange for being a great colleague during your short stay here in Delft. **Vineesh**: Thanks for being such a kind person and for some great scientific discussions. Your help in lab during the last year of my PhD immensely helped me to learn more about electrochemistry.

Now coming to the non-MECSicans. **Kosta and Christel**: Thanks for being such nice souls discussing science and for the random chats during the course of my PhD. It was great working with you both during the BPM perspective article and I learnt a lot from those discussions. I wish you both a great success in your PhDs. **Lorenz**: Thanks for always being open to share and discuss science across our labs and for the pressure relief valve that you helped install in our GC setup. **Jorrit**: Thanks for some fun conversations and for always being motivated by science.

To the **Collaborators**: Thank you Pratik, Asvin, Min, Prof. Atsushi and Ruud for helping me carry out experiments in your labs. The last work of my PhD showed me how much one can learn by not just being kind human beings, but by being open about scientific collaboration and discussions. And fellow researchers from other labs: Katie, Iris, Nandalal, Nat, Ezgi. I wish you all a great success in your academic journey. To **Prof. David Vermaas**: thank you for the multiple collaborations during my PhD and for some great discussions during our BPM work.

Friends: Thank you Uttam, Ayush, Parag, Bjarki and Hemanth for some wonderful time in the past 4 years. I feel fortunate to have met and shared some great moments. From weekend music jam sessions to random conversations about spirituality, philosophy and Richard Dawkins, it was great to have had lots of fun during the weekends. Thank you, Ayush, for making the time at Chamonix with Nino an unforgettable experience. The glacier hike is something that I am so fortunate to have tried and should continue in the future. **Srikkanth**: Thank you Srikkanth for some great weekend walks and talks in Delft and for the fun time during our Christmas trip to Cyprus. To **Prithiv and Lakshmi**: Thank you both for having me in Trier a few times and visiting me in Delft. It was fun roaming around with you guys and I learnt a lot from both of you.

To **Dhamma Friends**: Thank you Joost and Lotte for the Wednesday group meditation sittings in Rotterdam. It was great to have had weekly meditation sittings with other meditators. Maintaining the practice of Vipassana has been an important part of my life, that has given me so much mental strength and in dealing with situations better in life. I wish you and your family achieve great progress in Dhamma.

To my **Mom, Dad and Sister**: Thanking you here won't be enough. I am who I am today because of your constant care, support and values that I learnt from you all.

COVID-19: Thank you, COVID-19, for re-confirming that career is not the most important thing in life and Karma is real!

And finally! To all other friends and colleagues whom I may have missed here, thank you for being part of this great journey and I wish everyone a great success in their lives. I finish off with one of my favourite lines from 'The Office' series which goes like: "I wish there was a way to know you're in the good old days, before you've actually left them". Peace.

Siddhartha Subramanian
Delft, January 2024

CURRICULUM VITAE

Siddhartha SUBRAMANIAN

18-12-1992	Born in Tarapur, India.

EDUCATION

2010–2014	B.Tech in Chemical Engineering Pondicherry Engineering College Puducherry, India
2014–2015	Master of Science in Advanced Chemical Engineering Loughborough University, United Kingdom
2020-2024	PhD Chemical Engineering Delft University of Technology, Delft *Thesis:* Spatial Considerations in Membrane Electrode Assembly CO_2 Electrolyzers *Promotor:* Prof. dr. T.E. Burdyny

List of Publications

12. K. Petrov, C. Koopman, S. **Subramanian**, M. Koper, T. Burdyny, and D. Vermaas. “Bipolar membranes are a necessity for intrinsically stable and scalable CO_2 electrolysis”. In: (). In peer review.

11. S. **Subramanian**, J. Kok, P. Gholkar, A. S. Kumar, H.-P. I. van Montfort, R. Kortlever, A. Urakawa, B. Dam, and T. Burdyny. “CO residence time modulates multi-carbon formation rates in a zero gap Cu based CO_2 electrolyzer”. In: ()

10. H.-P. Iglesias van Montfort, S. **Subramanian**, E. Irtem, M. Sassenburg, M. Li, J. Kok, J. Middelkoop, and T. Burdyny. “An Advanced Guide to Assembly and Operation of CO_2 Electrolyzers”. In: *ACS Energy Letters* 8.10 (2023), pp. 4156–4161

9. H.-P. Iglesias van Montfort, M. Li, E. Irtem, M. Abdinejad, Y. Wu, S. K. Pal, M. Sassenburg, D. Ripepi, S. **Subramanian**, J. Biemolt, *et al.* “Non-invasive current collectors for improved current-density distribution during CO2 electrolysis on super-hydrophobic electrodes”. In: *Nature Communications* 14.1 (2023), p. 6579

8. M. Abdinejad, S. **Subramanian**, M. K. Motlagh, M. Noroozifar, S. Duangdangchote, I. Neporozhnii, D. Ripepi, D. Pinto, M. Li, K. Tang, *et al.* “Insertion of MXene-Based Materials into Cu–Pd 3D Aerogels for Electroreduction of CO_2 to Formate”. In: *Advanced Energy Materials* (2023), p. 2300402

7. M. Sassenburg, M. Kelly, S. **Subramanian**, W. A. Smith, and T. Burdyny. “Zero-gap electrochemical CO_2 reduction cells: challenges and operational strategies for prevention of salt precipitation”. In: *ACS Energy Letters* 8.1 (2022), pp. 321–331

6. S. **Subramanian**, K. Yang, M. Li, M. Sassenburg, M. Abdinejad, E. Irtem, J. Middelkoop, and T. Burdyny. “Geometric Catalyst Utilization in Zero-Gap CO_2 Electrolyzers”. In: *ACS Energy Letters* 8.1 (2022), pp. 222–229

5. M. Abdinejad, E. Irtem, A. Farzi, M. Sassenburg, S. **Subramanian**, H.-P. Iglesias van Montfort, D. Ripepi, M. Li, J. Middelkoop, A. Seifitokaldani, *et al.* “CO_2 Electrolysis via Surface-Engineering Electrografted Pyridines on Silver Catalysts”. In: *ACS catalysis* 12.13 (2022), pp. 7862–7876

4. L. Ge, H. Rabiee, M. Li, S. **Subramanian**, Y. Zheng, J. H. Lee, T. Burdyny, and H. Wang. “Electrochemical CO_2 reduction in membrane-electrode assemblies”. In: *Chem* 8.3 (2022), pp. 663–692

3. K. Yang, M. Li, S. **Subramanian**, M. A. Blommaert, W. A. Smith, and T. Burdyny. “Cation-driven increases of CO_2 utilization in a bipolar membrane electrode assembly for CO_2 electrolysis”. In: *ACS Energy Letters* 6.12 (2021), pp. 4291–4298

2. M. A. Blommaert, S. **Subramanian**, K. Yang, W. A. Smith, and D. A. Vermaas. “High indirect energy consumption in AEM-based CO_2 electrolyzers demonstrates the potential of bipolar membranes”. In: *ACS Applied Materials & Interfaces* 14.1 (2021), pp. 557–563

1. S. **Subramanian**, J. Middelkoop, and T. Burdyny. “Spatial reactant distribution in CO_2 electrolysis: balancing CO 2 utilization and faradaic efficiency”. In: *Sustainable Energy & Fuels* 5.23 (2021), pp. 6040–6048